SIMULATION OF III-V NANOWIRES FOR INFRARED PHOTODETECTION

SIMULATION OF III-V NANOWIRES FOR INFRARED PHOTODETECTION

By KHALIFA MOHAMMAD AZIZUR-RAHMAN, M.A.Sc.

A Thesis Submitted to the School of Graduate Studies

in Partial Fulfilment of the Requirements

for the Degree of

Doctor of Philosophy

McMaster University

DOCTOR OF PHILOSOPHY (2016)   McMaster University

(Engineering Physics)   Hamilton, Ontario

TITLE: Simulation of III-V Nanowires for Infrared Photodetection

AUTHOR: Khalifa Mohammad Azizur-Rahman

       B.A.Sc. Materials Science & Engineering

       (University of Toronto)

       M.A.Sc. Electrical & Computer Engineering

       (University of Waterloo)

SUPERVISOR: Professor Raymond R. LaPierre

NUMBER OF PAGES: xvii, 161

Abstract

The absorptance in vertical nanowire (nw) arrays is typically dominated by three optical phenomena: radial mode resonances, near-field evanescent wave coupling, and Fabry–Perot (F-P) mode resonances. The contribution of these optical phenomena to GaAs, InP and InAs nw absorptance was simulated using the finite element method. The study compared the absorptance between finite and semi-infinite nws with varying geometrical parameters, including the nw diameter (D), array period (P), and nw length (L). Simulation results showed that the resonance peak wavelength of the HE_{1n} radial modes linearly red-shifted with increasing D. The absorptance and spectral width of the resonance peaks increased as L increased, with an absorptance plateau for very long nws that depended on D and P. Near-field coupling between neighbouring nanowires (nws) was observed to increase with increasing diameter to period ratio (D/P). The effect of F-P modes was more pronounced for shorter nws and weakly coupled light.

Based on the collective observation of the correlation between nw geometry and optical phenomena in GaAs, InP, and InAs nw arrays, a periodic array of vertical InSb nws was designed for photodetectors in the low-atmospheric absorption window (λ = 3-5 µm) within the mid-wavelength infrared (MWIR) spectrum (λ = 3-8 µm). Simulations, using the finite element method, were implemented to optimize the nw array geometrical parameters (D, P, and L) for high optical absorptance (~0.8), which exceeded that of a thin film of equal

thickness. The results further showed that the HE_{1n} resonance wavelengths in InSb nw arrays can be tuned by adjusting D and P, thus enabling multispectral absorption throughout the near infrared (NIR) to MWIR region. Optical absorptance was investigated for a practical photodetector consisting of a vertical InSb nw array embedded in bisbenzocyclobutene (BCB) as a support layer for an ultrathin Ni contact layer. Polarization sensitivity of the photodetector was examined. Lastly, how light flux enters the nw top and sidewalls on HE_{11} resonance was investigated.

Acknowledgements

conversations. My family, especially my parents, provided ample motivation in my research work and constantly checked up on my research progress. I cannot thank them enough. Lastly, this acknowledgement section is incomplete without thanking my wife who helped me negotiate the ups and downs of research, proof reading my writings from time to time, and providing me great research feedback. It goes to say I could not have reached this far without the help and kindness of everyone around me.

This work is dedicated to everyone

who has motivated and helped me

to progress in my studies

Table of Contents

List of Figures

xii

List of Tables

1 Introduction

Everything in our surrounding environment emits and absorbs infrared (IR) light, which lies between the visible and microwave portions of the electromagnetic spectrum (~750 nm to 1 mm) [1]. As a result, sensing IR light for information regarding any particular object has proven valuable in the fields of astronomy, chemical sensing and spectroscopy, optical fiber communication, building diagnostics and electrical/mechanical inspection, law enforcement and firefighting, plant science and agriculture, defense, etc.

Various IR sensing material systems and detector device configurations have been investigated since IR light was first serendipitously discovered by Herschel in 1800 [2]. These detector types can be broadly classified into two major groups, namely thermal detectors and photon detectors [2].

In thermal detectors the absorbed incident IR photon heats up the detector element. The change in the element temperature results in a change in its physical property, e.g. electrical conductivity in the case of bolometers, which in turn results in output electrical signal. Thermal detectors do not require cooling; however, they have low spectral responsivity [2], where spectral responsivity is defined as the generated photocurrent per incident optical power [3].

In photon detectors, the incident IR photon is absorbed by electrons in the material leading to photocurrent. Photon detectors have wavelength-dependent spectral responsivity [2,3]. Photon detectors also require cryogenic cooling to

achieve high device performance, e.g. signal to noise ratio [2]. This thesis is focused on photon detectors for IR image sensing application in the mid-wavelength infrared (MWIR) region (3-8 μm).

1.1 Current infrared (IR) photon detectors

Among photon detectors, the most widely used material system for MWIR image sensing is $Hg_{1-x}Cd_xTe$ (MCT) [3]. In recent times, detector technologies based on other material systems have also been investigated as prospective alternatives, such as quantum well infrared photoconductors (QWIP) based on the III-V material system [3]. In this section, MCT and GaAs/AlGaAs based QWIP technology for IR detector applications will be briefly reviewed. This will be followed by a brief discussion of multispectral IR detectors. Detailed reviews of IR detectors based on MCT, QWIP, and other technologies including their application in multispectral detectors are provided in references [4–7].

1.1.1 IR detector material system and technology

1. *$Hg_{1-x}Cd_xTe$ (MCT):*

MCT is a ternary alloy that is considered a near ideal material for IR detection [4]. Its band gap (E_g) can be tuned by changing its alloy composition (x) from semimetallic HgTe (E_g = -0.3 eV at x = 0 and T = 4.2 K) to semiconducting CdTe (E_g = 1.648 eV at x = 1 and T = 4.2 K) [4]. Also, while the E_g is tuned with

x, the change in lattice constant is minute, which allows for the possibility of fabricating high quality layered and graded structures [4,5]. MCT also has large absorption coefficient up to the tunable E_g, long carrier lifetime, and high electron mobility that allows for high device quantum efficiency [4,5]. Due to these unique advantages, MCT is widely used for high performance IR photodetection applications in MWIR and other IR spectrum categories such as short wavelength infrared (SWIR: 1.4-3 μm), long wavelength infrared (LWIR: 8-15 μm), etc. [4,5].

The primary disadvantage for MCT is its substrate. MCT is epitaxially grown on lattice matched CdZnTe wafers [4–6,8,9]. However, CdZnTe is extremely costly, the wafer sizes are small, and it has a different thermal expansion coefficient than Si resulting in integration issues with Si readout integrated circuits (ROIC) [4–6,8,9]. To put the cost of CdZnTe into perspective, the cost of a 6 inch (15.24 cm) diameter Si wafer is ~$100 while 7 x 7 cm^2 CdZnTe costs $10000 [5]. Thus to date, the major application of MCT has been confined to IR detectors [5]. The readily producible wafer sizes however increased in recent times from the reported ~50 cm^2 in 2009 [5] to ~64 cm^2 in 2016 [6]. In order to avert the high cost of CdZnTe, research was conducted toward directly growing MCT on Si substrate for better integration with Si ROIC. Even though the lattice mismatch between MCT and Si is ~19%, MCT was epitaxially grown on Si using a CdTe/ZnTe buffer layer [5]. However, MCT on Si demonstrates higher dislocation density than MCT on CdZnTe [5]. As a result, CdZnTe is still the preferred substrate for fabricating

high performance MCT-based IR detectors and in most device configurations Si ROIC is epoxied onto the CdZnTe substrate [6].

2. *QWIP:*

Amongst the various QWIPs that have been investigated, the GaAs/AlGaAs material system based QWIP is the most thoroughly investigated technology [5]. GaAs/AlGaAs-based QWIPs have certain inherent advantages over MCT-based detectors such as established manufacturing and processing techniques for GaAs growth, high yield of uniform film growth on 6 inch GaAs wafers, and relatively low manufacturing cost [9]. Unlike MCT, QWIPs absorb IR light in a narrow absorption band of full-width-at-half-maximum (FWHM) of ~1-2 μm [9]. Hence they are particularly suited for multispectral detection as they have zero spectral crosstalk between different absorption bands if the bands are separated by a few microns in wavelength [9]. However, QWIPs have low quantum efficiency ($< 10\%$) since optical transitions are forbidden for normally incident light [9]. They also require operating at T $<$ 70K due to the inherent limitation of intersubband transitions [9].

The success of QWIPs led to research into quantum dot infrared photodetectors (QDIP), e.g. InAs quantum dots (QDs) embedded in InGaAs quantum wells with GaAs barrier [5]. Theoretically, QDIPs have certain advantages over QWIPs such as normal incidence response and higher operating temperature

[9]. However, significant challenges exist in achieving the theoretical predictions due to lack of control over ensemble size and density [9].

1.1.2 Multispectral IR detectors

A multispectral detector has several absorption wavelength bands with negligible overlap or crosstalk [7,10]. This results in a multicolored image that contains the spectral information from each of the absorption wavelength bands [7,10]. An IR multispectral detector has multiple absorption bands in the IR spectrum [5,7,10]. Simultaneous multispectral IR detection is important as it offers the capability of detecting temperature differences in various objects allowing for better contrast in the IR [7].

Two approaches are used for multispectral detection in standard detectors [5]. In the first approach additional optical equipment are used above the photodetector arrays, such as lenses, prisms, diffraction gratings, etc. These optical equipment disperse the incident IR light onto different photodetector arrays [5]. This results in a multicolored image based on the IR wavelength band incident on each photodetector array. In the second approach, filter wheels, with bandpass filters that allow IR light to flow within a specified wavelength band, are used to spectrally discriminate the incident light and focus it onto a single array of photodetectors [5]. Several images are then captured at different wavelength bands and added together to produce a multicolored image. The added optical architecture from both of these approaches require complicated optical alignment leading to

high cost and additional device constraints, including increase in size of the detector array and cooling requirements [5].

One of the strategies employed in order to avoid these additional optical instrumentation complexities is to fabricate a vertical stack of detectors that have different spectral sensitivities. For example, stacking chronologically largest E_g detector in the path of the incident light first, followed by successively shorter bandgap detectors. As a result, the shortest incident wavelength is absorbed first and the longest wavelength is absorbed last [5]. Using this approach, two and three color detectors have been developed for MCT based detectors with spectral response at two and three separate spectral bands [5]. Four color detectors with sensitivities in four unique spectral bands spanning from 3 μm to ~16 μm wavelength range was also demonstrated using QWIPs. This was possible due to the narrow spectral band width of the QWIPs [5].

A more recent approach toward multispectral detection is to directly fabricate a tunable Fabry-Perot (F-P) cavity filter array on top of the detector array [5,9]. The filter etalon spacing in these F-P cavity filters are changed via applied bias to transmit a specified narrow spectral band (200-300 nm) onto the detector [5,9]. This allows for the spectral sensitivity to be modulated real-time based on sensor requirements [5,9]. Drawbacks to this approach are that F-P cavity filter transmittance is low (60% to 70% in SWIR and 30% to 40% in LWIR [5]) and additional ROIC is required to tune the etalon spacing. The latter drawback

increases the complexity of ROIC integration with the photodetector device in addition to the fabrication complexity of producing the F-P cavity filters [5,9].

Both of the above alternative approaches toward multispectral detection introduces additional design complexity. A simpler cost effective and efficient design approach is desirable for multispectral imaging with preferably an alternative material system to MCT that can be directly grown on Si substrates.

1.2 Prospective application of III-V based vertical nanowire (nw) arrays for multispectral IR photodetectors

Continued advancement of material fabrication and characterization techniques over the past decade have vastly increased the ability to repeatedly create complex nanostructures. Vertical nw arrays of various semiconductors have recently been produced via bottom up and top down fabrication techniques [11]. Of note are the III-V based nws that have desirable structural and optical properties that can be used to develop cheap and efficient multispectral detectors in SWIR, MWIR, and LWIR wavelength bands of the IR spectrum. Provided below is a brief review of the structural and optical properties of III-V based vertical nw arrays and the prospective advantages of nw-based multispectral IR detectors. Similar properties can be equally observed for other semiconductor-based nws.

1.2.1 Structural properties

III-V nws possess unique structural features over the respective constituent bulk materials and thin film counterparts. One of the desirable structural properties of nws is that nw sidewalls are capable of reducing lattice misfit strain during epitaxial growth [12,13]. This allows lattice mismatched heterostructures to be fabricated, e.g. GaAs on Si, that would otherwise be impossible with planar thin films. This opens the possibility of fabricating III-V based nws on Si substrates that take advantage of cheaper and larger wafer sizes and well established fabrication processes of the Si industry [14]. Novel geometrical structures can also be incorporated into III-V nws such as core-shell heterostructures and axial heterostructures including the incorporation of quantum dots [15,16]. This allows for novel homojunction and heterojunction configurations in optoelectronic devices [17].

1.2.2 Optical properties

Unique optical phenomena are also observed in vertical nw arrays due to their geometrical structure. These optical phenomena are radial mode resonance, near-field evanescent wave coupling, and F-P mode resonance [18,19]. Due to the large refractive index mismatch between nws and the surrounding medium, nws act as nanoscopic waveguides that strongly couple to incident light at resonance wavelengths and guide them along the nw axis. These radial mode resonances enhance nw absorption at these resonance wavelengths over its bulk counterpart

[18,19]. The evanescent components of the guided light in nws overlap with neighbouring nws giving rise to near-field coupling. Significant near-field coupling also influences the nw absorptance properties and converts radial modes of single nws to photonic modes of the 2D nw photonic crystal array [20]. Furthermore, due to the finite dimension of the nw length (L), longitudinal or F-P modes also arise along the nw axis that also influence nw absorptance. The influence of all these optical phenomena on nw absorptance can be tuned by changing the nw array geometrical parameters: nw diameter (D), array period (P), and L [18,19].

1.2.3 Prospective advantages of nw based multispectral IR photodetectors

Based on the aforementioned brief nw properties, it can be stated that III-V nws possess unique qualities for multispectral IR photodetector applications that are difficult and costly to achieve with existing industry applied material systems and approaches for multispectral photodetectors:

1. *Better integration with Si ROIC:* III-V nw based multispectral photodetectors can be better integrated with Si ROIC by directly fabricating them on Si substrate.

2. *Inherent multispectral IR detection ability:* III-V nw array geometrical parameters can be tuned to achieve narrow spectral absorption bandwidth. This eliminates the need for additional spectral filter array above the photodetector array for multispectral detector design. This reduces

fabrication complexity, e.g. for bottom-up approach this can be achieved by defining P in a single lithography step and the D and L can be modulated by varying the growth condition. Alternatively, for top-down approach both D and P can be defined in a single lithography step and the L can be defined by etch time.

3. *NWs double as photodetector:* III-V nws can also incorporate radial and axial homojunctions and heterojunctions. Thus, not only do nws strongly absorb at specific spectral bands, but they can also convert the absorbed photons to current.

These unique advantages are expected to significantly improve multispectral photodetector device performance and reduce device fabrication complexity and overall cost. Studies have been conducted on the above mentioned properties of nws and a brief literature review will highlight relevant optical studies on nws in the following section.

1.3 Literature review

Radial modes, near-field evanescent wave coupling, and F-P modes are established concepts in the field of waveguide theory and photonic crystal theory and are covered in detail in books related to these fields [21–26]. However, the observation of these phenomena in nws has only come about recently due to the advancement of nw fabrication and characterization technology. A brief outline of

the literature on nw optical phenomena and their optoelectronic application is provided in this section.

Radial mode resonances have been observed on horizontal nws and vertical nw arrays by various groups. Resonance in horizontal nws were reported for Si [27–29] and Ge [30]. Nw absorptance on resonance was shown to drastically increase compared to planar thin films of the same material. These reports further demonstrated that the radial mode resonances are D dependent and red-shift with increasing D. Cao et al. also demonstrated from simulation study that the resonances in horizontal nws are caused by incident light coupling to the TE and TM family of radial modes [30].

Experimental and simulation studies of resonance in vertical nw arrays was demonstrated for various semiconductors such as Si (crystalline [31,32] and amorphous [33]), Ge (crystalline) [34], InP [35–39], GaAs [40,41], InAs [42], etc. Among these early reports, Seo et al. was one of the first to demonstrate through simultaneous experimental and simulation study on top-down etched circular cross-section Si nws that the incident light, parallel to the nw axis, coupled to the HE_{11} radial mode on resonance. They further showed that the HE_{11} resonance wavelength red-shifts linearly with D. A further simulation study on Si by Wang et al. [43] showed that the incident light also couples to higher order HE_{1n} modes at larger D [43]. They further demonstrated that higher order HE_{1n} modes not only linearly red-shifted with increasing D but the slope of the red-shift with respect to D decreased with successively higher order of HE_{1n} modes [43]. Similar to horizontal nws, the

absorptance of vertical nw arrays on HE_{1n} resonances was comparatively larger than planar thin film absorptance of the same material.

The absorptance spectra in vertical nws, for incident light parallel to nw axis, were observed to be invariant at longer wavelengths for circular and square nw cross-sections with equal cross-sectional area [44]. Similar results are also expected for equal area hexagonal and circular cross-section nws. This is based on the results by Henneghien et al. who showed that equal area hexagonal and circular cross-section nws have the same radial mode effective refractive index [45]. As a result, Henneghien et al. stipulated that the effective refractive index of the radial modes does not depend on transverse cross-section shape but on its area [45]. However, from the comparison of circular and square nw cross-section of equal area by Dossou et al. it can be more generally stated that as the degree of rotational symmetry of the cross-section decreases, the cross-section shape does begin to influence the effective refractive index of the radial modes [44].

Linearly polarized light incident upon the nw array at angles of incidence (θ) between 0° (parallel to the nw axis) and 90° (perpendicular to the nw axis) were also investigated through simulation study [20,43]. For $\theta \leq 5^o$ the incident light is observed to predominantly couple to the HE_{1n} family of modes [43]. But for $\theta > 5^o$, the incident light begins to couple to the TM_{1n} family of modes with increasing θ [20,43]. Concurrently, the resonance peak slightly blue-shifts (on the order of tens of nm) from the HE_{1n} resonance wavelength at $\theta = 0^o$ to TM_{1n} resonance wavelength at $\theta = 90^o$ [20,43].

For sparse nw arrays (D/P << 1), nw resonance absorptance can be explained by treating the nw as an individual waveguide [20,46]. In this regime the array absorptance was also shown to be equal to that of disordered arrays due to negligible influence of near field coupling [46]. However, for dense nw array the near field coupling between modes of neighbouring nws does affect the overall nw array absorptance [20]. With increasing nw density, the near-field coupling between modes of neighbouring nws increases and the resonance wavelength blue-shifts for incident light parallel to the nw axis [18–20,47]. Concurrently, the FWHM of the resonance absorptance peaks broaden [43]. Sturmberg et al. provided a theoretical treatment for explaining the influence of near-field coupling with increasing nw array density on nw radial modes by assuming nearest neighbour interaction for m = 1 mode [48]. Fountaine et al. further generalized the theoretical treatment by Sturmberg et al. for m-th mode orders and provided a theoretical explanation for radial mode blue- or red-shift with increasing lattice density or sparsity [20].

The lattice symmetry was shown to have negligible influence on vertical Si nw array absoprtance for D/P = 0.5. This was demonstrated by Li et al. for hexagonal and square lattice with the hexagonal lattice arrangement having slightly broader resonance peak [49]. However, for different material systems and for denser nw arrays (D/P > 0.5) the influence of lattice symmetry on nw array absorptance is expected to become significant with increasing near-field coupling.

Vertical nw array absorptance is polarization independent. This is due to the nw cross-sectional and array symmetry [19]. Park et al. recently demonstrated that

by using elliptical nw cross-section the absorptance spectra of the nws can be made polarization dependent [50]. For elliptical cross-section nws, the absorptance spectra is blue-shifted for polarization along the minor axis of the nw cross-section, compared to the absorptance spectra for polarization along the major axis [50].

The aforementioned optical properties of nw arrays were utilized to fabricate various nw based optoelectronic devices, such as solar cells, photodetectors, etc. For the case of solar cells, the array geometry (D, P, and L) are modulated to achieve broadband absorptance. This is achieved in two ways for vertical nws with non-tapered sidewalls:

1. The first approach is to make the nw array dense. This broadens the resonance peaks which in turn broadens the absorptance spectra. This approach was shown, via simulation study, most notably on Si [51], InP [36], and GaAs [52] based nws. Sturmberg et al. also reported a rigorous optimization study for achieving maximum solar absorptance (leading to maximum short circuit current) in Si, Ge, InP, and GaAs nw systems [53].

2. Fabricate an array with 2 x 2 square unit cell basis [54]. Each square sub-cell of the 2 x 2 basis cell has a nw of different D. This leads to different resonance wavelengths associated with each D, which in turn yields a broad absorptance spectrum for the 2 x 2 square unit cell. This approach was simulated using GaAs nws by Fountaine et al. [54].

In both cases the nw absorptance spectra were much larger than the planar thin film spectra of the same material.

Nw arrays can also be used for novel multispectral imaging and photodetector applications. Park et al. utilized the resonance absorptance property of vertical nw arrays to demonstrate compact multispectral filters based on Si nw arrays [55]. In a later paper they also demonstrated nw array based photodetectors in the visible spectrum for filter free image sensing [56]. Their device scheme took advantage of the resonance spectra of a nw array to directly convert absorbed light to photocurrent without the need for dye-based color filters that are commonly used for visible multispectral detectors [56]. Svensson et al. also demonstrated InAsSb nw array based MWIR photoconductors. They reported on the D dependence of the photocurrent and the good agreement with the resonance absorptance peak from simulation of InSb with the experimental photocurrent peak from InAsSb nws [57]. Thompson et al. later demonstrated InAsSb based p-i-n photodetectors on Si substrate with resonance spectra in the SWIR region [58]. However, to the best of our knowledge, a systematic study for achieving high resonance absorptance by optimizing the nw geometrical parameters for IR multispectral detector applications does not exist.

1.4 Thesis objective and outline

The objectives of this thesis are twofold. First, we aim to understand the individual contributions of nw optical phenomena, namely radial modes, near-field evanescent wave coupling, and F-P modes to GaAs, InP, and InAs nw array absorptance. This is achieved by comparing the absorptance between finite and semi-infinite nws with varying geometrical parameters, namely D, P, and L. The findings of this study were published under the title: "Wavelength-selective absorptance in GaAs, InP and InAs nanowire arrays" [18]. The results showed how much each optical phenomena influence nw absorptance, their correlation with nw array geometrical parameters, and how this can be applied to tune nw resonance absorptance for multispectral photodetector application.

Following the results from the aforementioned study, the second objective is to optimize InSb nw array parameters to produce sharp HE_{11} resonance peaks spanning near infrared (NIR) to MWIR spectral bands. This was done both in air and bisbenzocyclobutene (BCB) to demonstrate the multispectral HE_{11} absorption bands on InSb nw array. The results were used to present an optical design for a MWIR photodetector comprised of an InSb nw array on a Si substrate with ultrathin Ni top contact. The findings of this study were published under the title: "Optical design of a mid-wavelength infrared InSb nanowire photodetector" [19]. The simulation study, to the best of our knowledge, provides the first systematic study of InSb nw optical phenomena. The study also provides the first optimization

scheme for achieving high HE_{11} resonance absorptance up to the bandgap of InSb for the lowest nw aspect ratio (L/D). The results pave the way for optimizing multispectral photodetector optical design for other nw-based material systems for different wavelength bands.

In order to outline the results from the abovementioned objectives, which are presented in chapters 4 through 6, a theoretical overview of radial modes and near-field coupling are presented in chapter 2. This is followed by a brief overview of the simulation methodology in chapter 3. The thesis concludes with a summary of the highlighted results and prospective future research direction in chapter 7.

2 Nanowire (nw) optical phenomena

Three optical phenomena influence absorptance of incident light in vertical nanowire (nw) arrays: (1) radial mode resonance, (2) near-field evanescent wave coupling, and (3) longitudinal or Fabry-Perot (F-P) mode resonance.

Radial mode resonance occurs when the incident light couples strongly with the nw radial modes and are funnelled into the nw at specific wavelengths. These radial modes are electromagnetic wave solutions to nw radial boundary conditions. For non-absorbing nws (extinction coefficient $k(\lambda)$ is 0), radial modes that propagate without power loss along the nw (or waveguide) axis are called guided modes [21,22,24]. The guided mode field profile inside the nw arises due to the nw radial boundary conditions, and outside the nw the field profile monotonically decreases in the radial direction [21,24]. In contrast, radial modes that propagate along the nw axis while their confined power is attenuated via radiation propagating away from the nw are referred to as leaky modes [21,22,24]. The field profiles of leaky modes appear the same as guided modes up to the radiation caustic (R_{rad}). R_{rad} is a boundary in the cladding layer (medium outside the nw) that demarcates a distinct change in the field profile of the leaky mode [21,24]. The leaky mode field profile beyond R_{rad} is oscillatory with the amplitude damping with increasing radial distance from R_{rad} [21,24]. For absorbing nws, guided mode power is attenuated

through absorption along the nw axis [20]. On the other hand, leaky mode power is attenuated along the nw axis through simultaneous absorption along the nw axis and radiation of power away from the nw [20].

Near-field evanescent wave coupling occurs between neighbouring nws. Evanescent waves are a component of the radial mode that arises outside the nw. The amplitude of these waves decay with radial distance from the nw boundary. When the evanescent wave of one nw radial mode significantly overlaps with a neighbouring nw of same or different diameter (D) that can also support radial modes, then the radial modes between these neighbouring nws couple. This is also referred to as amplitude coupling [22]. As a result of this process, power transfers from one coupled radial mode to the other leading to a decrease in amplitude of the former mode and increase in amplitude of the latter.

F-P mode resonance arises due to the longitudinal boundary conditions at the nw array top and bottom. These boundary conditions give rise to axial standing waves along the nw length (L) through constructive interference of the guided incident light at specific wavelengths.

This chapter provides a brief mathematical review of radial modes in nws and near-field coupling between nws in an array. This is presented by approximating the nws as cylindrical step index dielectric waveguides that extend to infinity. Maxwell's equations are solved for this simplified cylindrical waveguide to arrive at guided mode solutions, i.e. the field profile outside the

waveguide monotonically decreases with increasing radial distance from the waveguide. This derivation is adapted from reference [59]. Mathematical solutions demonstrating oscillatory leaky mode field profiles beyond the R_{rad} are provided in the following reference [21]. In this thesis unless otherwise specified both guided and leaky modes will be collectively referred to by their general category, radial modes. The different radial modes that arise as solutions will then be briefly introduced along with their properties. This will be followed by an analysis of the family of modes responsible for nw absorption. The D dependence of the resonance absorptance will be reviewed. Thereafter, the influence of near-field coupling between neighbouring nws in a periodic nw array on the radial modes are investigated. The radial modes in a 2D nw array convert to photonic crystal modes and the resonance absorptance is likewise perturbed by the array period (P). The chapter concludes with a brief overview of references for further review of the subject matter.

2.1 Maxwell's equations in dielectric media

(a)   **(b)**
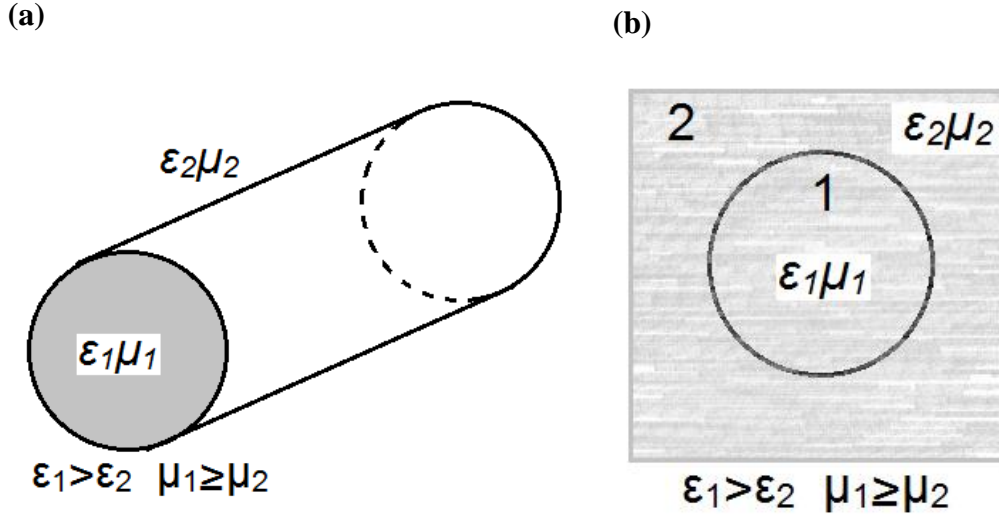
Figure 2.1. Schematic diagram of a cylindrical dielectric waveguide (a) side and (b) cross-section view. Image adapted from reference [59].

We begin our analysis of the electromagnetic wave behavior inside a nw by assuming that the nw is a cylindrical step index dielectric waveguide with infinite L to avoid axial standing waves that would give rise to F-P modes (see figure 2.1). Accordingly, Maxwell's equations inside matter are:

Gauss' Law: $$\vec{\nabla}.\vec{D}(\vec{r},t) = \rho_f \qquad (2.1)$$

$$\vec{\nabla}.\vec{B}(\vec{r},t) = 0 \qquad (2.2)$$

Faraday's Law: $$\vec{\nabla}\times\vec{E}(\vec{r},t) = -\frac{\partial\vec{B}(\vec{r},t)}{\partial t} \qquad (2.3)$$

Ampere's Law: $$\vec{\nabla}\times\vec{H}(\vec{r},t) = \vec{J_f} + \frac{\partial\vec{D}(\vec{r},t)}{\partial t} \qquad (2.4)$$

Here, $\vec{E}(\vec{r},t)$, $\vec{D}(\vec{r},t)$, and $\vec{B}(\vec{r},t)$ are the electric, electric displacement, and magnetic fields respectively. $\vec{H}(\vec{r},t)$ is simply referred as H, for according to Sommerfeld as quoted by Griffiths "The unhappy term 'magnetic field' for H should be avoided as far as possible. It seems to us that this term has led into error none less than Maxwell himself…" [60]. Both $\vec{E}(\vec{r},t)$ and $\vec{D}(\vec{r},t)$, and $\vec{B}(\vec{r},t)$ and $\vec{H}(\vec{r},t)$, are related to each other via constitutive relationships governed by the nature of the medium the fields are in [59,60]. ρ_f and $\vec{J_f}$ are free charge and free current density. Equations (2.1) to (2.4) represent a convenient way of dividing charge into free and bound parts [60]. However, they are disadvantaged by the hybrid notation of simultaneously containing $\vec{E}(\vec{r},t)$, $\vec{D}(\vec{r},t)$ $\vec{B}(\vec{r},t)$, and $\vec{H}(\vec{r},t)$ [60].

Now, we will make some further simplifying assumptions for ease of analytical calculations:

1. $\rho_f = 0$ and $\vec{J_f} = 0$

2. The dielectric medium is isotropic, linear, and non-magnetic. Thus, $\varepsilon = \varepsilon_0\varepsilon_r$ (ε_r is a scalar) and $\mu = \mu_0$ ($\mu_r = 1$) [59]. However, ε can depend on frequency.

Hence, $\vec{D}(\vec{r}, t) = \varepsilon \vec{E}(\vec{r}, t)$ and $\vec{H}(\vec{r}, t) = \left(\frac{1}{\mu}\right)\vec{B}(\vec{r}, t)$. We can now rewrite Maxwell's equation in terms of $\vec{E}(\vec{r}, t)$ and $\vec{H}(\vec{r}, t)$ as follows:

$$\vec{\nabla} \cdot \vec{E}(\vec{r}, t) = 0 \tag{2.5}$$

$$\vec{\nabla} \cdot \vec{H}(\vec{r}, t) = 0 \tag{2.6}$$

$$\vec{\nabla} \times \vec{E}(\vec{r}, t) = -\mu \frac{\partial \vec{H}(\vec{r}, t)}{\partial t} \tag{2.7}$$

$$\vec{\nabla} \times \vec{H}(\vec{r}, t) = \varepsilon \frac{\partial \vec{E}(\vec{r}, t)}{\partial t} \tag{2.8}$$

2.2 The wave equation for E- and H-fields

Equations (2.7) and (2.8) can be decoupled into E- and H-field terms by applying the curl to each one of them. For example, equation (2.7) would then read:

$$\vec{\nabla} \times \left(\vec{\nabla} \times \vec{E}(\vec{r}, t)\right) = \vec{\nabla} \times \left(-\mu \frac{\partial \vec{H}(\vec{r}, t)}{\partial t}\right) \tag{2.9}$$

$$\vec{\nabla}\left(\vec{\nabla} \cdot \vec{E}(\vec{r}, t)\right) - \nabla^2 \vec{E}(\vec{r}, t) = -\mu \frac{\partial \left(\vec{\nabla} \times \vec{H}(\vec{r}, t)\right)}{\partial t} = -\mu\varepsilon \frac{\partial^2 \vec{E}(\vec{r}, t)}{\partial t^2} \tag{2.10}$$

$$\nabla^2 \vec{E}(\vec{r}, t) = \mu\varepsilon \frac{\partial^2 \vec{E}(\vec{r}, t)}{\partial t^2} \tag{2.11}$$

Given that the refractive index of a material is $n = \sqrt{\dfrac{\mu\varepsilon}{\mu_o \varepsilon_o}} = \sqrt{\varepsilon_r}$, and the speed of light $c = \dfrac{1}{\sqrt{\mu_o \varepsilon_o}}$, they can be used to substitute $\mu\varepsilon = \left(\dfrac{n}{c}\right)^2$. The wave equation for $\vec{E}(\vec{r}, t)$ now takes the following form:

$$\nabla^2 \vec{E}(\vec{r},t) = \left(\frac{n}{c}\right)^2 \frac{\partial^2 \vec{E}(\vec{r},t)}{\partial t^2} \tag{2.12}$$

Similarly, by applying the above approach to equation (2.8) we arrive at the following wave equation for $\vec{H}(\vec{r},t)$:

$$\nabla^2 \vec{H}(\vec{r},t) = \left(\frac{n}{c}\right)^2 \frac{\partial^2 \vec{H}(\vec{r},t)}{\partial t^2} \tag{2.13}$$

The E- and H-field vectors can be represented in different basis vector representations; however, for ease of calculation with cylindrical waveguides the field vectors will be represented in a cylindrical coordinate basis system. The E-field vector in cylindrical coordinates is represented as follows:

$$\vec{E}(\vec{r},t) = E_\rho(\vec{r},t)\hat{\boldsymbol{\rho}} + E_\phi(\vec{r},t)\hat{\boldsymbol{\phi}} + E_z(\vec{r},t)\hat{\boldsymbol{z}} \tag{2.14}$$

Hence, the E-field wave equation can be represented in cylindrical basis as follows:

$$\nabla^2 E_\rho(\vec{r},t)\hat{\boldsymbol{\rho}} + \nabla^2 E_\phi(\vec{r},t)\hat{\boldsymbol{\phi}} + \nabla^2 E_z(\vec{r},t)\hat{\boldsymbol{z}}$$
$$= \left(\frac{n}{c}\right)^2 \left(\frac{\partial^2 E_\rho(\vec{r},t)}{\partial t^2}\hat{\boldsymbol{\rho}} + \frac{\partial^2 E_\phi(\vec{r},t)}{\partial t^2}\hat{\boldsymbol{\phi}} + \frac{\partial^2 E_z(\vec{r},t)}{\partial t^2}\hat{\boldsymbol{z}}\right) \tag{2.15}$$

All the cylindrical basis vector components in the E-field wave equation have the same structure, namely:

$$\nabla^2 E_q(\vec{r},t) = \left(\frac{n}{c}\right)^2 \frac{\partial^2 E_q(\vec{r},t)}{\partial t^2} \tag{2.16}$$

Where, $q = \rho$, ϕ, and z. The H-field wave equation can be similarly decomposed into cylindrical basis vector components and represented as above by

replacing the E-field components by their analog H-field components. Henceforward, equations for the E-field will be solved and the analogous equations for the H-field will simply be presented for conciseness unless the equations related to the H-field are different.

2.3 The Helmholtz equation

The wave equation for the E-field will now be solved. The analogous wave equation for the H-field has the same solution. Given that equation (2.16) is a second order partial differential equation (PDE), our first approach is to apply the method of separation of variables.

We decouple the E-field wave equation into spatial $\left(E_s(\vec{r})\right)$ field and temporal $\left(E_t(t)\right)$ field components by seeking a solution that is a simple product:

$$E_q(\vec{r}, t) = E_s(\vec{r})E_t(t) \tag{2.17}$$

where, $q = \rho$, ϕ, and z. Inserting equation (2.17) into equation (2.16) we then obtain the following relation:

$$\frac{\nabla^2 E_S(\vec{r})}{E_S(\vec{r})} = \left(\frac{n}{c}\right)^2 \frac{1}{E_t(t)} \frac{\partial^2 E(t)}{\partial t^2} \tag{2.18}$$

The two sides of the equation are dependent on different variables and hence both sides are constant. Without loss of generality we then equate both sides to $-k^2$.

The spatial portion can now be written as:

$$\frac{\nabla^2 E_S(\vec{r})}{E_S(\vec{r})} = -k^2 \tag{2.19}$$

$$\nabla^2 E_S(\vec{r}) + k^2 E_S(\vec{r}) = 0 \tag{2.20}$$

Equation (2.20) is the Helmholtz equation. The temporal portion can now be written as:

$$\left(\frac{n}{c}\right)^2 \frac{1}{E_t(t)} \frac{d^2 E(t)}{dt^2} = -k^2 \tag{2.21}$$

$$\frac{d^2 E_t(t)}{dt^2} = -\left(\frac{ck}{n}\right)^2 E_t(t) \tag{2.22}$$

We can now substitute in angular frequency (ω) by noting that $\frac{c}{n} k = ck_0 = \omega$, where the wavenumber ($k$) in a medium is $k = k_0 n = \frac{2\pi n}{\lambda}$ (k_0 is the wavenumber in vacuum). Therefore,

$$\frac{d^2 E_t(t)}{dt^2} + \omega^2 E_t(t) = 0 \tag{2.23}$$

The general solution to the time dependent second order differential equation is:

$$E_t(t) = ae^{j\omega t} + be^{-j\omega t} \tag{2.24}$$

Equation (2.24) provides the evolution of the wave at a certain frequency (ω) with time and indicates that the time variation of the fields is sinusoidal. Fields with sinusoidal time variation are called time-harmonic fields.

2.4 The Helmholtz equation in cylindrical coordinates

The Laplacian in the Helmholtz equation (equation (2.20)) can be expanded in cylindrical coordinates as follows:

$$\nabla^2 f = \frac{1}{\rho}\frac{\partial}{\partial \rho}\left(\rho\frac{\partial f}{\partial \rho}\right) + \frac{1}{\rho^2}\frac{\partial^2 f}{\partial \phi^2} + \frac{\partial^2 f}{\partial z^2} \tag{2.25}$$

As a result, the Helmholtz equation takes the following form:

$$\frac{1}{\rho}\frac{\partial}{\partial \rho}\left(\rho\frac{\partial E_S(\vec{r})}{\partial \rho}\right) + \frac{1}{\rho^2}\frac{\partial^2 E_S(\vec{r})}{\partial \phi^2} + \frac{\partial^2 E_S(\vec{r})}{\partial z^2} + k^2 E_S(\vec{r}) = 0 \tag{2.26}$$

This is also a second order differential equation. We again resort to the method of separation of variables to divide the spatial component into a product of functions, each of which depend on only one of the three orthogonal bases of the cylindrical coordinate system:

$$E_S(\vec{r}) = E(\rho)E(\phi)E(z) \tag{2.27}$$

We now insert equation (2.27) into the Helmholtz equation in cylindrical coordinates (equation (2.26)) and then proceed to reorganize it in such a manner that each function is separated into individual parts as follows:

$$\frac{1}{\rho}\frac{\frac{\partial}{\partial \rho}\left(\rho\frac{\partial E(\rho)}{\partial \rho}\right)}{E(\rho)} + \frac{1}{\rho^2}\frac{\frac{\partial^2 E(\phi)}{\partial \phi^2}}{E(\phi)} + \frac{\frac{\partial^2 E(z)}{\partial z^2}}{E(z)} + k^2 = 0 \tag{2.28}$$

We first note that the transverse and longitudinal parts are dependent on different variables. Hence each of these two segments can be equated to a constant. We conveniently choose the longitudinal component to be equal to constant $-\beta^2$:

$$\frac{\frac{\partial^2 E(z)}{\partial z^2}}{E(z)} = -\beta^2 \tag{2.29}$$

Thus the general solution to equation (2.29) is:

$$E(z) = Ae^{j\beta z} + Be^{-j\beta z} \tag{2.30}$$

Additionally, the transverse component is equated to a constant $-T^2$:

$$\frac{1}{\rho}\frac{\frac{\partial}{\partial \rho}\left(\rho\frac{\partial E(\rho)}{\partial \rho}\right)}{E(\rho)} + \frac{1}{\rho^2}\frac{\frac{\partial^2 E(\phi)}{\partial \phi^2}}{E(\phi)} = -T^2 \tag{2.31}$$

The constants T and β are transverse and longitudinal wavenumbers of the E- and H-fields. They are related to the overall wavenumber (k) by the following equation:

$$T^2 + \beta^2 = k^2 \tag{2.32}$$

We can further reorganize the equation (2.31) into the following relation:

$$\rho\frac{\frac{\partial}{\partial \rho}\left(\rho\frac{\partial E(\rho)}{\partial \rho}\right)}{E(\rho)} + (\rho T)^2 = -\frac{\frac{\partial^2 E(\phi)}{\partial \phi^2}}{E(\phi)} \tag{2.33}$$

Both sides are now dependent on different variables and hence, as shown previously, both sides are equal to a constant. Thus, the transverse segment can also be separated into angular (φ) and radial (ρ) portions.

The angular component can be written as follows:

$$\frac{\frac{\partial^2 E(\phi)}{\partial \phi^2}}{E(\phi)} = -v^2 \tag{2.34}$$

Here, v is the angular wavenumber. The general solution to the φ component of the E-field is:

$$E(\phi) = A e^{jv\phi} + B e^{-jv\phi} \tag{2.35}$$

The transverse component equation (2.33) can now be rewritten as follows:

$$\rho \frac{\partial}{\partial \rho} \left(\rho \frac{\partial E(\rho)}{\partial \rho} \right) + (\rho^2 T^2 - v^2) E(\rho) = 0 \tag{2.36}$$

This is the Bessel equation. For $T^2 > 0$ and when v is an integer ($v = m$), the general solution is:

$$E(\rho) = A_m J_m(\rho T) + B_m N_m(\rho T) \tag{2.37}$$

Here, $J_m(\rho T)$ is a Bessel function of the first kind and $N_m(\rho T)$ is a Bessel function of the second kind, alternatively referred to as a Neumann function. The following linear combinations are also solutions of the Bessel equation:

$$H_m^{(1)}(\rho T) = J_m(\rho T) + j \cdot N_m(\rho T) \tag{2.38}$$

$$H_m^{(2)}(\rho T) = J_m(\rho T) - j \cdot N_m(\rho T) \tag{2.39}$$

$H_m^{(1)}(\rho T)$ and $H_m^{(2)}(\rho T)$ are Hankel functions of the first and second kind. The functions, $J_m(\rho T)$, $N_m(\rho T)$, $H_m^{(1)}(\rho T)$, and $H_m^{(2)}(\rho T)$ are linearly independent and linear combination of any two of these functions form a complete solution of

the Bessel equation [59]. The functions $J_m(\rho T)$ and $N_m(\rho T)$ are quasi-periodic with multiple zeros [59]. As the argument values in these functions increase they can be approximated by cosine and sine functions [59].

Conversely for $T^2 < 0$, the Bessel equation can be rewritten as follows:

$$\rho \frac{\partial}{\partial \rho} \left(\rho \frac{\partial E(\rho)}{\partial \rho} \right) - (\rho^2 \tau^2 + \upsilon^2) E(\rho) = 0 \tag{2.40}$$

Here, T was replaced by $j\tau$. The solutions are then $J_\upsilon(j\rho\tau)$ and $N_\upsilon(j\rho\tau)$ [59]. Here again we assume υ is an integer ($\upsilon = m$). Real linearly independent solutions can be constructed out of $J_m(j\rho\tau)$ and $N_m(j\rho\tau)$ as follows:

$$I_m(\rho\tau) = j^{-m} J_m(j\rho\tau) \tag{2.41}$$

$$K_m(\rho\tau) = j^{-m+1} \frac{\pi}{2} [J_m(j\rho\tau) + jN_m(j\rho\tau)] \tag{2.42}$$

where $I_m(\rho\tau)$ and $K_m(\rho\tau)$ are modified Bessel functions of the first and second kind, respectively. As a result, the general solution to equation (2.40) can be written as follows:

$$E(\rho) = A_m I_m(\rho\tau) + B_m K_m(\rho\tau) \tag{2.43}$$

The $I_m(\rho\tau)$ and $K_m(\rho\tau)$ functions are monotonically increasing and decreasing functions, respectively. In the limit of large arguments, they can be better approximated by an exponential function.

2.5 E- and H-field in cylindrical coordinates

Depending on the specific boundary condition, the radial portion of $E_q(\rho, \phi, z, t)$ (where, $q = \rho, \phi, z$) can take on either of the aforementioned set of solutions, i.e., Bessel functions, Neumann functions, and Hankel functions or modified Bessel functions. The $E_q(\rho, \phi, z, t)$ component of the E-field, based on equation (2.17), can now be written in the following form if we assume that the wave is propagating in the positive z-direction:

$$E_q(\rho, \phi, z, t) = E_q(\rho, \phi)e^{-j\beta z}e^{j\omega t} \tag{2.44}$$

Similarly, the $H_q(\rho, \phi, z, t)$ component of the H-field takes the same form as well:

$$H_q(\rho, \phi, z, t) = H_q(\rho, \phi)e^{-j\beta z}e^{j\omega t} \tag{2.45}$$

As a result, we can state that the E- and H-fields of a monochromatic wave with frequency ω propagating in the positive z-direction in cylindrical coordinates as:

$$\vec{E}(\rho, \phi, z, t) = \vec{E}(\rho, \phi)e^{-j\beta z}e^{j\omega t} \tag{2.46}$$

$$\vec{H}(\rho, \phi, z, t) = \vec{H}(\rho, \phi)e^{-j\beta z}e^{j\omega t} \tag{2.47}$$

Inserting the $\vec{E}(\rho, \phi, z, t)$ and $\vec{H}(\rho, \phi, z, t)$ relations from equation (2.46) and (2.47) into Faraday's and Ampere's Law, and performing algebraic manipulation, the transverse components of the E-field, $E_\rho(\rho, \phi, z)$ and $E_\phi(\rho, \phi, z)$, and the H-field, $H_\rho(\rho, \phi, z)$ and $H_\phi(\rho, \phi, z)$, can be determined from the algebraic

combination of $E_z(\rho, \phi, z)$ and $H_z(\rho, \phi, z)$ components. This simplifies the problem to determining the $E_z(\rho, \phi, z)$ and $H_z(\rho, \phi, z)$ components and then other components can be found in relation to them.

We now insert equations (2.46) and (2.47) into Faraday's Law, equation (2.7), arriving at the following relationship:

$$\vec{\nabla} \times \vec{E}(\rho, \phi, z) = -j\omega\mu\vec{H}(\rho, \phi, z) \tag{2.48}$$

Thereafter, we expand the differential equation in cylindrical coordinates:

$$\left[\frac{1}{\rho}\frac{\partial E_z(\rho, \phi, z)}{\partial \phi} - \frac{\partial E_\phi(\rho, \phi, z)}{\partial z}\right]\hat{\rho} + \left[\frac{\partial E_\rho(\rho, \phi, z)}{\partial z} - \frac{\partial E_z(\rho, \phi, z)}{\partial \rho}\right]\hat{\phi}$$

$$+ \frac{1}{\rho}\left[\frac{\partial \left(\rho E_\phi(\rho, \phi, z)\right)}{\partial \rho} - \frac{\partial E_\rho(\rho, \phi, z)}{\partial \phi}\right]\hat{z} \tag{2.49}$$

$$= -j\omega\mu\left[H_\rho(\rho, \phi, z)\hat{\rho} + H_\phi(\rho, \phi, z)\hat{\phi} + H_z(\rho, \phi, z)\hat{z}\right]$$

Equation (2.49) can be subdivided into its spatial components as follows:

1. *Radial basis vector component ($\hat{\boldsymbol{\rho}}$):*

$$\frac{1}{\rho}\frac{\partial E_z(\rho, \phi, z)}{\partial \phi} + j\beta E_\phi(\rho, \phi, z) = -j\omega\mu H_\rho(\rho, \phi, z) \tag{2.50}$$

2. *Angular basis vector component ($\hat{\boldsymbol{\phi}}$):*

$$-j\beta E_\rho(\rho, \phi, z) - \frac{\partial E_z(\rho, \phi, z)}{\partial \rho} = -j\omega\mu H_\phi(\rho, \phi, z) \tag{2.51}$$

3. *Longitudinal basis vector component ($\hat{\mathbf{z}}$):*

$$\frac{1}{\rho}\left[\frac{\partial\left(\rho E_\phi(\rho,\phi,z)\right)}{\partial\rho} - \frac{\partial E_\rho(\rho,\phi,z)}{\partial\phi}\right] = -j\omega\mu H_z(\rho,\phi,z) \tag{2.52}$$

We can apply the same strategy used in Faraday's law equation with Ampere's law equation (equation (2.8)) by first inserting equations (2.46) and (2.47) and then subdividing them into the three spatial cylindrical basis vector components as follows:

1. *Radial basis vector component ($\hat{\boldsymbol{\rho}}$):*

$$\frac{1}{\rho}\frac{\partial H_z(\rho,\phi,z)}{\partial\phi} + j\beta H_\phi(\rho,\phi,z) = j\omega\varepsilon E_\rho(\rho,\phi,z) \tag{2.53}$$

2. *Angular basis vector component ($\hat{\boldsymbol{\phi}}$):*

$$-j\beta H_\rho(\rho,\phi,z) - \frac{\partial H_z(\rho,\phi,z)}{\partial\rho} = j\omega\varepsilon E_\phi(\rho,\phi,z) \tag{2.54}$$

3. *Longitudinal basis vector component ($\hat{\mathbf{z}}$):*

$$\frac{1}{\rho}\left[\frac{\partial\left(\rho H_\phi(\rho,\phi,z)\right)}{\partial\rho} - \frac{\partial H_\rho(\rho,\phi,z)}{\partial\phi}\right] = j\omega\varepsilon E_z(\rho,\phi,z) \tag{2.55}$$

We now solve for $E_\phi(\rho, \phi, z)$ and $H_\rho(\rho, \phi, z)$ from equations (2.50) and (2.54) and $E_\rho(\rho, \phi, z)$ and $H_\phi(\rho, \phi, z)$ from equations (2.51) and (2.53) and express them in terms of $E_z(\rho, \phi, z)$ and $H_z(\rho, \phi, z)$ as follows:

$$E_\rho(\rho, \phi, z) = \frac{j}{\beta^2 - k^2}\left[\beta \frac{\partial E_z(\rho, \phi, z)}{\partial \rho} + \frac{\omega\mu}{\rho}\frac{\partial H_z(\rho, \phi, z)}{\partial \phi}\right] \qquad (2.56)$$

$$E_\phi(\rho, \phi, z) = \frac{j}{\beta^2 - k^2}\left[\frac{\beta}{\rho}\frac{\partial E_z(\rho, \phi, z)}{\partial \phi} - \omega\mu\frac{\partial H_z(\rho, \phi, z)}{\partial \rho}\right] \qquad (2.57)$$

$$H_\rho(\rho, \phi, z) = \frac{j}{\beta^2 - k^2}\left[\beta \frac{\partial H_z(\rho, \phi, z)}{\partial \rho} - \frac{\omega\varepsilon}{\rho}\frac{\partial E_z(\rho, \phi, z)}{\partial \phi}\right] \qquad (2.58)$$

$$H_\phi(\rho, \phi, z) = \frac{j}{\beta^2 - k^2}\left[\frac{\beta}{\rho}\frac{\partial H_z(\rho, \phi, z)}{\partial \phi} + \omega\varepsilon\frac{\partial E_z(\rho, \phi, z)}{\partial \rho}\right] \qquad (2.59)$$

We now have relationships for E_ρ, E_ϕ, H_ρ, and H_ϕ (equations (2.56) to (2.59)) field components in terms of E_z and H_z field components that satisfy Maxwell's equations. The E_z and H_z field components are defined in terms of propagating waves in the positive z-direction of the cylindrical coordinate system (equation (2.44) and (2.45) for $q = z$). Equations (2.56) to (2.59) can now be used to find the E- and H-field components in a cylindrical waveguide.

2.6 E- and H-fields in a cylindrical waveguide

After deriving all the necessary equations to solve the E- and H-field components inside a cylindrical waveguide, we will now focus our attention on step index fibers that stretch to infinity, each of which consists of a uniform core, with refractive index ($n_1 = \sqrt{\frac{\mu_1 \varepsilon_1}{\mu_o \varepsilon_o}}$), and cladding layer, with refractive index ($n_2 = \sqrt{\frac{\mu_2 \varepsilon_2}{\mu_o \varepsilon_o}}$). The refractive index of the core is greater than that of the cladding layer ($n_1 > n_2$). This ensures that the total reflection condition is met and that the core can accommodate radial modes. As the waveguide is radially symmetric, we have the following angular component condition:

$$\phi = \phi + 2\pi \tag{2.60}$$

As a result, the $E(\phi)$ (equation (2.35)) field component after 2π rotation will equal itself:

$$e^{j\upsilon\phi} = e^{j\upsilon(\phi+2\pi)} \tag{2.61}$$

$$1 = e^{j\upsilon 2\pi} \tag{2.62}$$

$$2\pi m = 2\pi \upsilon \tag{2.63}$$

$$m = \upsilon \tag{2.64}$$

Hence, υ is an integer and the radial components of first and second kinds of Bessel functions and modified Bessel functions will have integer order. We can now state the E- and H-field components in the waveguide core and cladding layer.

2.6.1 E- and H-field components in waveguide core

In the core, where $0 \leq \rho \leq R$, the radial solution of the $E_z(\rho, \phi, z)$ and $H_z(\rho, \phi, z)$ field components is a Bessel function of the first kind. The Neumann function solution diverges to negative infinity at $\rho = 0$. Thus, its coefficient is zero in the general solution (equation 2.37). The angular solution takes on integer value for υ. As a result, the Bessel function solutions are of integer order. Additionally, it is assumed that the wave propagates in the positive z-direction, hence the longitudinal solution is $e^{-j\beta z}$. Thus, based on equations (2.44) and (2.45) and (2.56) to (2.59), the time harmonic E- and H-field components have the following solution in the waveguide core (the subscript 1 denotes core layer):

$$E_{z1}(\rho, \phi, z) = A J_m(\rho T) e^{jm\phi} e^{-j\beta z} \tag{2.65}$$

$$E_{\rho1}(\rho, \phi, z) = \frac{1}{T^2}\left[-j\beta A J'_m(\rho T) + \frac{m\omega\mu_1}{\rho} B J_m(\rho T)\right] e^{jm\phi} e^{-j\beta z} \tag{2.66}$$

$$E_{\phi1}(\rho, \phi, z) = \frac{1}{T^2}\left[\frac{m\beta}{\rho} A J_m(\rho T) + j\omega\mu_1 B T J'_m(\rho T)\right] e^{jm\phi} e^{-j\beta z} \tag{2.67}$$

$$H_{z1}(\rho, \phi, z) = B J_m(\rho T) e^{jm\phi} e^{-j\beta z} \tag{2.68}$$

$$H_{\rho1}(\rho, \phi, z) = \frac{1}{T^2}\left[-j\beta B T J'_m(\rho T) - \frac{m\omega\varepsilon_1}{\rho} A J_m(\rho T)\right] e^{jm\phi} e^{-j\beta z} \tag{2.69}$$

$$H_{\phi1}(\rho, \phi, z) = \frac{1}{T^2}\left[\frac{\beta m}{\rho} B J_m(\rho T) - j\omega\varepsilon_1 A T J'_m(\rho T)\right] e^{jm\phi} e^{-j\beta z} \tag{2.70}$$

Here, the sum of the squares of T and β equal the overall wavenumber in the waveguide core (k_1):

$$T^2 + \beta^2 = k_1^2 = \left(\frac{\omega}{v_1}\right)^2 = \left(\frac{\omega n_1}{c}\right)^2 = \omega^2 \varepsilon_1 \mu_1 \qquad (2.71)$$

2.6.2 E- and H-field components in waveguide cladding layer

The cladding layer is assumed to extend to infinity, where $R \leq \rho \leq \infty$. The wave solutions we seek should have a finite value at $\rho = R$ and decay to zero as ρ approaches infinity, giving us the field profiles for guided modes. So $T^2 < 0$, and we replace T with $j\tau$. Thus, the solution is a modified Bessel function of the second kind. The modified Bessel function of the first kind diverges to infinity as ρ approaches infinity. Hence, its coefficient is zero in the general solution (equation 2.43). Therefore, based on equations (2.44) and (2.45), and (2.56) to (2.59), the time harmonic E- and H-field components have the following solution in the waveguide cladding layer (the subscript 2 denotes cladding layer):

$$E_{z2}(\rho, \phi, z) = C K_m(\rho\tau) e^{jm\phi} e^{-j\beta z} \qquad (2.72)$$

$$E_{\rho2}(\rho, \phi, z) = \frac{1}{\tau^2}\left[j\beta\tau C K_m'(\rho\tau) - \frac{\omega\mu_2 m}{\rho} D K_m(\rho\tau) \right] e^{jm\phi} e^{-j\beta z} \qquad (2.73)$$

$$E_{\phi2}(\rho, \phi, z) = \frac{1}{\tau^2}\left[-\frac{m\beta}{\rho} C K_m(\rho\tau) - j\omega\mu_2\tau D K_m'(\rho\tau) \right] e^{jm\phi} e^{-j\beta z} \qquad (2.74)$$

$$H_{z2}(\rho, \phi, z) = D K_m(\rho\tau) e^{jm\phi} e^{-j\beta z} \qquad (2.75)$$

$$H_{\rho 2}(\rho, \phi, z) = \frac{1}{\tau^2}\left[j\beta\tau D K_m'(\rho\tau) + \frac{m\omega\varepsilon_2}{\rho} C K_m(\rho\tau) \right] e^{jm\phi} e^{-j\beta z} \qquad (2.76)$$

$$H_{\phi 2}(\rho, \phi, z) = \frac{1}{\tau^2}\left[-\frac{m\beta}{\rho} D K_m(\rho\tau) + j\omega\varepsilon_2\tau C K_m'(\rho\tau) \right] e^{jm\phi} e^{-j\beta z} \qquad (2.77)$$

Here, the sum of the squares of the transverse wavenumber (τ) and β equal the overall wavenumber in the waveguide cladding layer (k_2):

$$-\tau^2 + \beta^2 = k_2^2 = \left(\frac{\omega}{v_2}\right)^2 = \left(\frac{\omega n_2}{c}\right)^2 = \omega^2 \varepsilon_2 \mu_2 \qquad (2.78)$$

2.7 Eigenvalue equation of a cylindrical waveguide

Boundary conditions are used to find the eigenvalue equation of a cylindrical waveguide. The tangential E- and H-field components, namely $E_z(\rho, \phi, z)$, $H_z(\rho, \phi, z)$, $E_\phi(\rho, \phi, z)$, and $H_\phi(\rho, \phi, z)$, at the boundary ($\rho = R$), between core and cladding layer, are continuous [3,24,59]. Utilizing this boundary condition leads to the following set of linear equations for z and ϕ-components of the E- and H-fields:

1. *z-component of E- and H-fields:*

$$E_{z1}(R, \phi, z) = E_{z2}(R, \phi, z) \qquad (2.79)$$

$$A J_m(RT) - C K_m(R\tau) = 0 \qquad (2.80)$$

and

$$H_{z1}(R, \phi, z) = H_{z2}(R, \phi, z) \tag{2.81}$$

$$BJ_m(RT) - DK_m(R\tau) = 0 \tag{2.82}$$

2. φ-component of E- and H-fields:

$$E_{\phi 1}(R, \phi, z) = E_{\phi 2}(R, \phi, z) \tag{2.83}$$

$$\frac{m\beta}{RT^2} AJ_m(RT) + \frac{j\omega\mu_1}{T} BJ'_m(RT) + \frac{m\beta}{R\tau^2} CK_m(R\tau) + \frac{j\omega\mu_2}{\tau} DK'_m(R\tau)$$

$$= 0 \tag{2.84}$$

and

$$H_{\phi 1}(R, \phi, z) = H_{\phi 2}(R, \phi, z) \tag{2.85}$$

$$-\frac{j\omega\varepsilon_1}{T} AJ'_m(RT) + \frac{\beta m}{RT^2} BJ_m(RT) - \frac{j\omega\varepsilon_2}{\tau} CK'_m(R\tau) + \frac{\beta m}{R\tau^2} DK_m(R\tau)$$

$$= 0 \tag{2.86}$$

The four simultaneous homogeneous linear equations, (2.80), (2.82), (2.84), and (2.86), can be written in matrix form as follows:

$$\begin{bmatrix} J_m(RT) & 0 & -K_m(R\tau) & 0 \\ 0 & J_m(RT) & 0 & -K_m(R\tau) \\ \frac{m\beta}{RT^2}J_m(RT) & \frac{j\omega\mu_1}{T}J'_m(RT) & \frac{m\beta}{R\tau^2}K_m(R\tau) & \frac{j\omega\mu_2}{\tau}K'_m(R\tau) \\ -\frac{j\omega\varepsilon_1}{T}J'_m(RT) & \frac{\beta m}{RT^2}J_m(RT) & -\frac{j\omega\varepsilon_2}{\tau}K'_m(R\tau) & \frac{\beta m}{R\tau^2}K_m(R\tau) \end{bmatrix} \begin{bmatrix} A \\ B \\ C \\ D \end{bmatrix} = 0 \tag{2.87}$$

Non-trivial solutions to this matrix equation can be found by equating the determinant of the coefficient matrix to zero. We then arrive at the following

general eigenvalue equation for the cylindrical waveguide after some algebraic manipulation:

$$\left[\frac{\varepsilon_1}{RT}\frac{J'_m(RT)}{J_m(RT)} + \frac{\varepsilon_2}{R\tau}\frac{K'_m(R\tau)}{K_m(R\tau)}\right] \cdot \left[\frac{\mu_1}{RT}\frac{J'_m(RT)}{J_m(RT)} + \frac{\mu_2}{R\tau}\frac{K'_m(R\tau)}{K_m(R\tau)}\right]$$
$$-\left(\frac{m\beta}{\omega}\right)^2\left[\frac{1}{(RT)^2} + \frac{1}{(R\tau)^2}\right]^2 = 0 \tag{2.88}$$

We can omit β by manipulating equations (2.71) and (2.78) as follows:

$$1 + \left(\frac{\beta}{T}\right)^2 = \omega^2\frac{\varepsilon_1\mu_1}{T^2} \tag{2.89}$$

$$-1 + \left(\frac{\beta}{\tau}\right)^2 = \omega^2\frac{\varepsilon_2\mu_2}{\tau^2} \tag{2.90}$$

After adding equations (2.89) and (2.90), we arrive at the following expression:

$$\beta^2\left[\frac{1}{(RT)^2} + \frac{1}{(R\tau)^2}\right] = \omega^2\left[\frac{\varepsilon_1\mu_1}{(RT)^2} + \frac{\varepsilon_2\mu_2}{(R\tau)^2}\right] \tag{2.91}$$

Additionally, by subtracting equation (2.78) from (2.71) we arrive at the following relation for RT and $R\tau$:

$$(RT)^2 + (R\tau)^2 = (Rk_1)^2 - (Rk_2)^2 = \sqrt{\omega^2R^2(\varepsilon_1\mu_1 - \varepsilon_2\mu_2)} = V^2 \tag{2.92}$$

Here, V is a unitless number often called the fiber number or normalized frequency and it is a characteristic parameter of a waveguide [3,21].

Substituting equation (2.91) into the eigenvalue equation, equation (2.88), we arrive at the following relation:

$$
\left[\frac{\varepsilon_1}{RT} \frac{J'_m(RT)}{J_m(RT)} + \frac{\varepsilon_2}{R\tau} \frac{K'_m(R\tau)}{K_m(R\tau)} \right] \cdot \left[\frac{\mu_1}{RT} \frac{J'_m(RT)}{J_m(RT)} + \frac{\mu_2}{R\tau} \frac{K'_m(R\tau)}{K_m(R\tau)} \right]
$$
$$
- m^2 \left[\frac{\varepsilon_1 \mu_1}{(RT)^2} + \frac{\varepsilon_2 \mu_2}{(R\tau)^2} \right] \left[\frac{1}{(RT)^2} + \frac{1}{(R\tau)^2} \right] = 0
$$

(2.93)

Equations (2.92) and (2.93) can now be used to find the eigenvalue (RT) of the radial modes in the cylindrical dielectric for a specific V. It is also convenient for mode analysis to introduce a factor χ by rearranging equation (2.93) into the following form:

$$
\chi = \frac{\left[\frac{\varepsilon_1}{RT} \frac{J'_m(RT)}{J_m(RT)} + \frac{\varepsilon_2}{R\tau} \frac{K'_m(R\tau)}{K_m(R\tau)} \right]}{m \left[\frac{\varepsilon_1 \mu_1}{(RT)^2} + \frac{\varepsilon_2 \mu_2}{(R\tau)^2} \right]} = \frac{m \left[\frac{1}{(R\tau)^2} + \frac{1}{(RT)^2} \right]}{\left[\frac{\mu_1}{RT} \frac{J'_m(RT)}{J_m(RT)} + \frac{\mu_2}{R\tau} \frac{K'_m(R\tau)}{K_m(R\tau)} \right]}
$$

(2.94)

We now make substitutions to either the first or second portion of equation (2.94) so that they both have the same expression. This is achieved by substituting the denominator of the first segment of equation (2.94), first via equation (2.91) and then equation (2.88), or the numerator of the second segment of equation (2.94), via equation (2.88), to arrive at the following expression:

$$
\chi = \frac{\omega}{\beta} \frac{\sqrt{\frac{\varepsilon_1}{RT} \frac{J'_m(RT)}{J_m(RT)} + \frac{\varepsilon_2}{R\tau} \frac{K'_m(R\tau)}{K_m(R\tau)}}}{\sqrt{\frac{\mu_1}{RT} \frac{J'_m(RT)}{J_m(RT)} + \frac{\mu_2}{R\tau} \frac{K'_m(R\tau)}{K_m(R\tau)}}}
$$

(2.95)

Equation (2.95) along with the ratios of coefficients C and A, or D and B, from equation (2.80) or (2.82), namely:

$$\frac{C}{A} = \frac{D}{B} = \frac{J_m(RT)}{K_m(R\tau)} \tag{2.96}$$

are inserted into equation (2.84) and (2.86) to arrive at the following ratio of H_z to E_z component:

$$\frac{H_z}{E_z} = \frac{B}{A} = \frac{D}{C} = j \frac{\sqrt{\dfrac{\varepsilon_1}{RT}\dfrac{J_m'(RT)}{J_m(RT)} + \dfrac{\varepsilon_2}{R\tau}\dfrac{K_m'(R\tau)}{K_m(R\tau)}}}{\sqrt{\dfrac{\mu_1}{RT}\dfrac{J_m'(RT)}{J_m(RT)} + \dfrac{\mu_2}{R\tau}\dfrac{K_m'(R\tau)}{K_m(R\tau)}}} = \frac{j\beta\chi}{\omega} \tag{2.97}$$

In order to better determine the radial modes, the eigenvalue equation (2.93) can be reorganized into the following quadratic equation:

$$\left[\frac{J_m'(RT)}{J_m(RT)}\right]^2 + \left[\frac{(\varepsilon_1\mu_2 + \varepsilon_2\mu_1)}{\varepsilon_1\mu_1}\frac{RTK_m'(R\tau)}{R\tau K_m(R\tau)}\right]\frac{J_m'(RT)}{J_m(RT)}$$

$$+ \frac{\varepsilon_2\mu_2}{\varepsilon_1\mu_1}\left[\frac{RTK_m'(R\tau)}{R\tau K_m(R\tau)}\right]^2 \tag{2.98}$$

$$- (mRT)^2\left[\frac{1}{(RT)^2} + \frac{\varepsilon_2\mu_2}{\varepsilon_1\mu_1(R\tau)^2}\right]\left[\frac{1}{(R\tau)^2} + \frac{1}{(RT)^2}\right] = 0$$

The quadratic formula then yields the following two roots:

$$\frac{J_m'(RT)}{J_m(RT)} = -P + \sqrt{Q} \tag{2.99}$$

$$\frac{J_m'(RT)}{J_m(RT)} = -P - \sqrt{Q} \tag{2.100}$$

where P and Q are:

$$P = \frac{\varepsilon_1 \mu_2 + \varepsilon_2 \mu_1}{2\varepsilon_1 \mu_1} \cdot \frac{RTK'_m(R\tau)}{R\tau K_m(R\tau)} \tag{2.101}$$

$$Q = \left(\frac{\varepsilon_1 \mu_2 - \varepsilon_2 \mu_1}{2\varepsilon_1 \mu_1}\right)^2 \left[\frac{RTK'_m(R\tau)}{R\tau K_m(R\tau)}\right]^2$$

$$+ \left(\frac{m}{RT}\right)^2 \left[1 + \frac{\varepsilon_2 \mu_2}{\varepsilon_1 \mu_1}\left(\frac{RT}{R\tau}\right)^2\right]\left[1 + \left(\frac{RT}{R\tau}\right)^2\right] \tag{2.102}$$

$R\tau$ can be found in relation to RT from equation (2.92). The two roots (equations (2.99) and (2.100)) specify the eigenvalues of two different radial modes in the cylindrical dielectric. At this juncture we define these radial modes:

1. *Transverse Electric Mode (TE):* the longitudinal E_z component is zero. The radial mode has a non-zero H_z component [61]. All the E-field components are on the transverse plane to the direction of propagation [61]. From equation (2.97) this occurs when χ approaches ∞.

2. *Transverse Magnetic Mode (TM):* the longitudinal H_z component is zero. The radial mode has a non-zero E_z component [61]. All the H-field components are on the transverse plane to the direction of propagation [61]. From equation (2.97) this occurs when χ approaches 0.

3. *Hybrid HE or EH Mode:* both the longitudinal E_z and H_z components have non-zero values. The field strength of $E_z > H_z$ for HE modes and $H_z > E_z$ for EH modes [24]. Equation (2.100) represents the eigenvalue equation for

HE modes and equation (2.99) represents the eigenvalue equation for EH modes [59].

4. *Transverse Electromagnetic Mode (TEM):* both the longitudinal E_z and H_z components have a value of zero [61]. In order to arrive at these eigenmodes, instead of using the above approach, the Helmholtz equation needs to be solved for the transverse components [61]. TEM modes are not typically observed in nws and hence will not be further discussed in this thesis.

Additionally, the modes are further classified by indices m and n in the subscript, e.g. HE$_{mn}$. These indices are defined as follows:

1. *m (Angular or azimuthal mode index):* indicates the number of field maxima along the angular direction for 2π rotation [62]. m = 0 indicates circularly symmetric modes. In the field profile equations, m also indicates the order of the Bessel function of the first kind (in equations (2.65) to (2.70)) and modified Bessel function of the second kind (in equations (2.72) to (2.77)) [61].

2. *n (Radial mode index):* indicates the number of field maxima and minima along the radial direction [62]. Alternatively, it counts the number of field nulls or roots in the radial direction [43]. In the field profile equations (2.65) to (2.70), n indicates the nodes of the Bessel function of the first kind.

We will now work out some simple examples for finding the eigenvalue of TE, TM, and hybrid HE and EH modes.

2.7.1 TE and TM modes (m = 0)

We can obtain TE and TM modes by setting m = 0. Then, by using the recurrence formula for the derivative of the Bessel function of the first kind and modified Bessel function of the second kind we obtain:

$$J'_m(x) = \frac{1}{2}[J_{m-1}(x) - J_{m+1}(x)] \tag{2.103}$$

$$J'_0(x) = \frac{1}{2}[J_{-1}(x) - J_1(x)] = \frac{1}{2}[-J_1(x) - J_1(x)] = -J_1(x) \tag{2.104}$$

and

$$K'_m(x) = -\frac{1}{2}[K_{m-1}(x) + K_{m+1}(x)] \tag{2.105}$$

$$K'_0(x) = -\frac{1}{2}[K_{-1}(x) + K_1(x)] = -\frac{1}{2}[K_1(x) + K_1(x)] = -K_1(x) \tag{2.106}$$

Inserting the results from equations (2.104) and (2.106) into equation (2.99) we get the following relation:

$$\frac{J'_0(RT)}{J_0(RT)} = -\frac{J_1(RT)}{J_0(RT)} = -P + \sqrt{Q} = \frac{\mu_2}{\mu_1}\frac{RTK_1(R\tau)}{R\tau K_0(R\tau)} \tag{2.107}$$

$$\frac{J_1(RT)}{J_0(RT)} = -\frac{\mu_2}{\mu_1}\frac{RTK_1(R\tau)}{R\tau K_0(R\tau)} \tag{2.108}$$

Similarly, by inserting the results from equations (2.104) and (2.106) into equation (2.100) we get the following relation:

$$\frac{J_0'(RT)}{J_0(RT)} = -\frac{J_1(RT)}{J_0(RT)} = -P - \sqrt{Q} = \frac{\varepsilon_2}{\varepsilon_1}\frac{RTK_1(R\tau)}{R\tau K_0(R\tau)} \tag{2.109}$$

$$\frac{J_1(RT)}{J_0(RT)} = -\frac{\varepsilon_2}{\varepsilon_1}\frac{RTK_1(R\tau)}{R\tau K_0(R\tau)} \tag{2.110}$$

Equation (2.108) is the eigenvalue equation of the TE_{0n} modes and equation (2.110) is the eigenvalue equation of the TM_{0n} modes. We can analytically deduce which equation represents the eigenvalues of either TE_{0n} or TM_{0n} by inserting either equation (2.108) or (2.110) into the equation (2.97) for m = 0. For equation (2.108), the ratio of H_z over E_z goes to infinity (similarly $\chi \to \infty$) in equation (2.97), which indicates that $E_z = 0$ and the expression represents TE_{0n} modes. For equation (2.110), the ratio of H_z over E_z goes to zero (similarly $\chi = 0$) in equation (2.97), which indicates that $H_z = 0$ and the expression represents TM_{0n} modes.

By utilizing equations (2.108) and (2.110) we can now determine the eigenvalues of TE_{0n} and TM_{0n} modes. Figure 2.2 was plotted using MATLAB to demonstrate the eigenvalues (RT) for TE_{01}, TE_{02}, TM_{01} and TM_{02} for core refractive index (n_1) = 3.5, cladding refractive index (n_2) = 1, and V = 12. As frequency increases (i.e. V increases), more modes in the waveguide are guided [59].
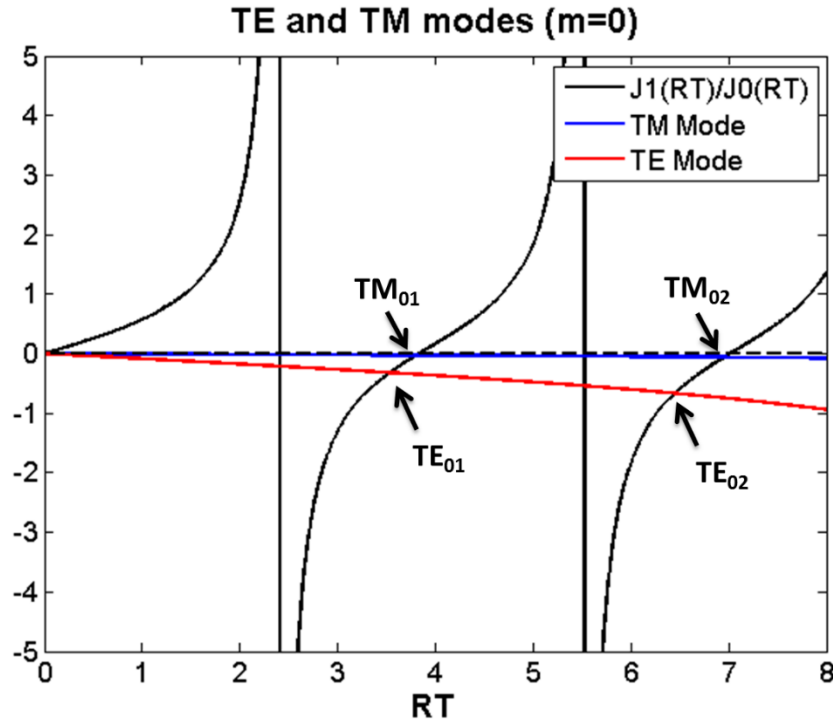
Figure 2.2. Graphical method for determining the eigenvalues (*RT*) for TE_{01}, TE_{02}, TM_{01}, and TM_{02} modes of a cylindrical dielectric waveguide. The dielectric was assumed to be non-magnetic. The refractive index inside the core (n_1) is 3.5, refractive index of the cladding layer (n_2) is 1, and V is 12 (MATLAB code presented in Appendix 9.1).

1. *TE_{0n} Mode:*

We can also utilize the properties of TE_{0n} modes (m = 0, E_z = 0 which implies coefficient $A = C = 0$ in equations (2.65) to (2.70) and (2.72) to (2.77), and using equation (2.96)) to arrive at the following TE_{0n} mode E- and H-field profiles in cylindrical coordinates:

$$E_{\phi 1}(\rho, \phi, z) = -\frac{1}{T} j\omega\mu_1 B J_1(\rho T) e^{-j\beta z} \tag{2.111}$$

$$H_{z1}(\rho, \phi, z) = B J_0(\rho T) e^{-j\beta z} \tag{2.112}$$

$$H_{\rho 1}(\rho, \phi, z) = \frac{1}{T} j\beta B J_1(\rho T) e^{-j\beta z} \tag{2.113}$$

$$E_{\phi 2}(\rho, \phi, z) = \frac{1}{\tau} j\omega\mu_2 D K_1(\rho\tau) e^{-j\beta z}$$

$$= -\frac{1}{\tau} j\omega\mu_2 \frac{J_0(RT)}{K_0(R\tau)} B K_1(\rho\tau) e^{-j\beta z} \tag{2.114}$$

$$H_{z2}(\rho, \phi, z) = D K_0(\rho\tau) e^{-j\beta z} = -\frac{J_0(RT)}{K_0(R\tau)} B K_0(\rho\tau) e^{-j\beta z} \tag{2.115}$$

$$H_{\rho 2}(\rho, \phi, z) = -\frac{1}{\tau} j\beta D K_1(\rho\tau) e^{-j\beta z} = \frac{1}{\tau} j\beta \frac{J_0(RT)}{K_0(R\tau)} B K_1(\rho\tau) e^{-j\beta z} \tag{2.116}$$
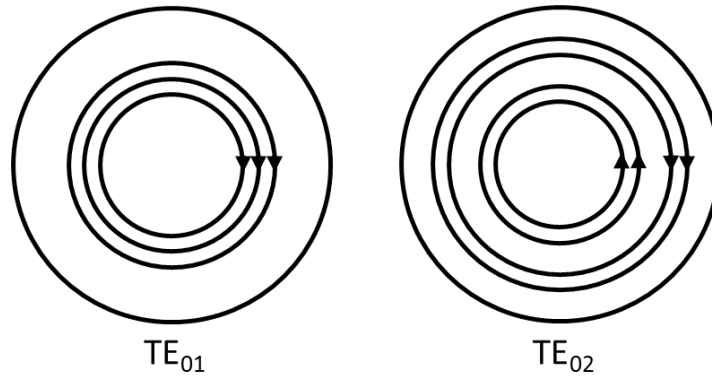
Figure 2.3. Electric field patterns of TE$_{01}$ and TE$_{02}$ radial modes [59].

From the mode profile solutions (equations (2.111) to (2.116)), it is observed that the E-field only has an angular component in the transverse plane of the waveguide (equation (2.111)) as shown in figure 2.3. The n values (2nd mode

index) indicate the nodes. On either side of the nodes the field lines switch directions, because the Bessel function amplitude changes sign.

2. *TM$_{0n}$ Mode:*

Applying a similar strategy to obtain the TE$_{0n}$ modes, we use the TM$_{0n}$ mode properties (m $= 0$, $H_z = 0$, which implies coefficient $B = D = 0$ in equations (2.65) to (2.70) and (2.72) to (2.77), and using equation (2.96)) to arrive at the TM$_{0n}$ mode profiles in cylindrical coordinates:

$$E_{z1}(\rho, \phi, z) = AJ_0(\rho T)e^{-j\beta z} \tag{2.117}$$

$$E_{\rho 1}(\rho, \phi, z) = \frac{1}{T}j\beta AJ_1(\rho T)e^{-j\beta z} \tag{2.118}$$

$$H_{\phi 1}(\rho, \phi, z) = \frac{1}{T}j\omega\varepsilon_1 AJ_1(\rho T)e^{-j\beta z} \tag{2.119}$$

$$E_{z2}(\rho, \phi, z) = CK_0(\rho\tau)e^{-j\beta z} = -\frac{J_0(RT)}{K_0(R\tau)}AK_0(\rho\tau)e^{-j\beta z} \tag{2.120}$$

$$E_{\rho 2}(\rho, \phi, z) = -\frac{1}{\tau}j\beta CK_1(\rho\tau)e^{-j\beta z} = \frac{1}{\tau}j\beta\frac{J_0(RT)}{K_0(R\tau)}AK_1(\rho\tau)e^{-j\beta z} \tag{2.121}$$

$$H_{\phi 2}(\rho, \phi, z) = -\frac{1}{\tau}j\omega\varepsilon_2 CK_1(\rho\tau)e^{-j\beta z}$$

$$= \frac{1}{\tau}j\omega\varepsilon_2\frac{J_0(RT)}{K_0(R\tau)}AK_1(\rho\tau)e^{-j\beta z} \tag{2.122}$$
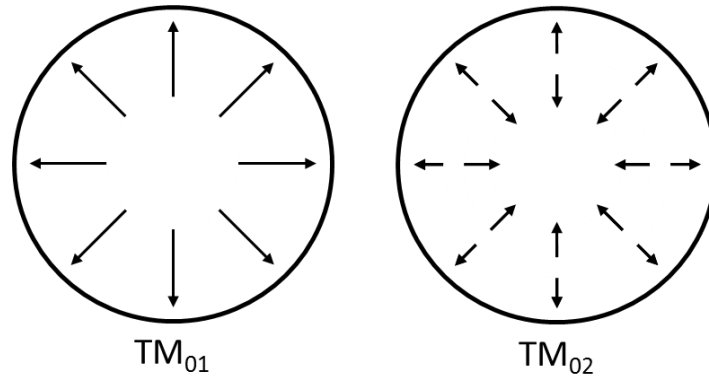
Figure 2.4. Electric field patterns of TM_{01} and TM_{02} radial modes [59].

The E-field patterns for TM_{0n} modes radially point outward as only the radial component of the E-field exists in the transverse plane of the waveguide as shown in figure 2.4. As the n value increases, field lines switch directions on either side of the node since the Bessel function amplitude changes sign.

2.7.2 Hybrid HE and EH modes (m ≠ 0)

The hybrid HE and EH modes have more complex field patterns in the transverse plane of the waveguide, involving both radial and angular terms. In particular, one group of HE modes are essential to the study of resonance absorptance in vertical nws. They are the HE_{1n} group (m = 1). The eigenvalue solutions of the HE_{1n} and EH_{1n} radial modes are plotted via MATLAB in figure 2.5.
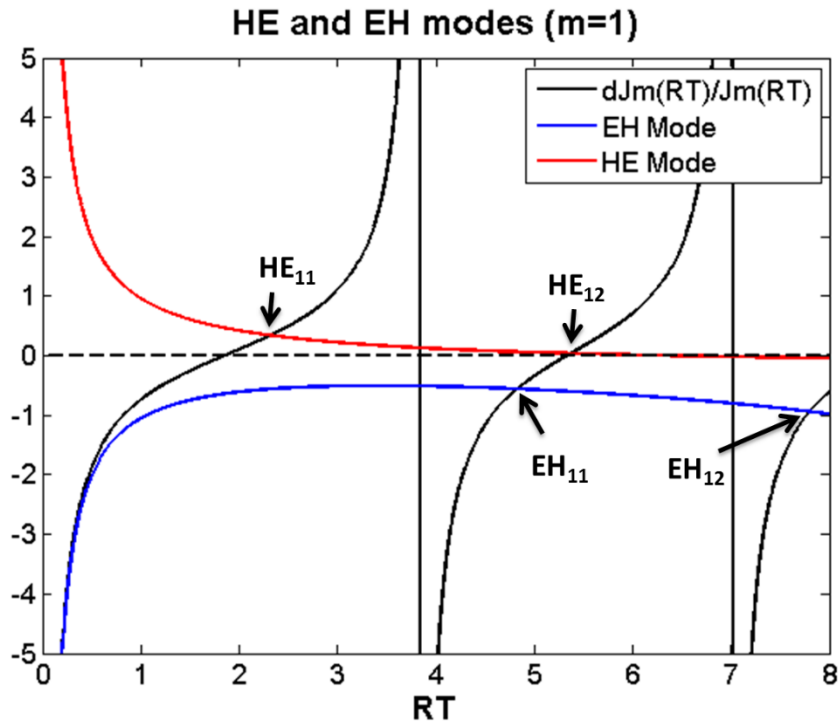
Figure 2.5. Graphical method for determining the eigenvalues (*RT*) for hybrid HE_{11}, HE_{12}, EH_{11}, and EH_{12} modes of a cylindrical dielectric waveguide. The dielectric was assumed to be non-magnetic. The refractive index inside the core (n_1) is 3.5, refractive index of the cladding layer (n_2) is 1, and *V* is 12 (MATLAB code presented in Appendix 9.2).

The intersections between the red and black lines indicate the HE_{1n} mode solutions and the intersections between the blue and black lines indicate the EH_{1n} mode solutions. Regardless of how small the *V* parameter is, the red line always intersects the black line to indicate the eigenvalue solution of the HE_{11} mode. This is because HE_{11} mode is a fundamental cylindrical waveguide mode with no cut-off frequency. It is the HE_{1n} modes that couple and guide incident light into vertical

nw [20,36,43,53]. The electric field lines of the HE_{11} and HE_{12} radial modes are shown in figure 2.6.
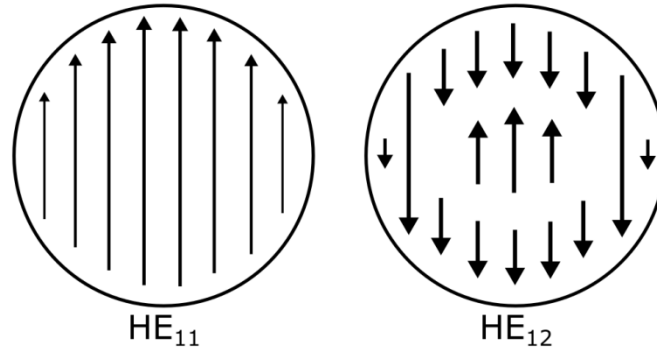
Figure 2.6. Electric field patterns of hybrid HE_{11} and HE_{12} radial modes [59].

2.7.3 Coupling of incident light to HE_{1n} family of modes

Incident light couples to HE_{1n} modes more favorably compared to other nw modes, namely TE_{0n}, TM_{0n}, HE_{mn} (m > 1), EH_{mn} (m > 1), which, barring specific cut-off conditions for modes, all exist within the nw waveguide. This can be understood by analyzing the symmetry properties of these modes and how closely their E-field pattern resembles that of the incident plane wave [36,43]. The closer the resemblance, the more coupling overlap the mode will have with the incident light. A plane wave, with E-field polarized in the X or Y direction, is anti-symmetric under reflection along y-z or x-z plane that axially bisects the nw (cylindrical waveguide) [43]. As a result, the plane wave is circularly asymmetric and has

angular mode index m = 1 (π rotation returns to the same value) [36]. This rules out

excitation of all modes except for m = 1 group of modes, namely: HE_{1n} and EH_{1n}

[36]. Between these two groups, the transverse E-field pattern of the HE_{1n} modes

closely resembles that of the plane wave, inside and outside the nw core, with the

E-field pattern of the HE_{11} mode resembling it the most [36]. This is unlike EH_{1n}

modes which have different E-field patterns in the transverse waveguide cross-

section to that of the incident plane wave. This is why the HE_{1n} family of modes

are the dominant excited modes in vertical nws [20,36,43]. Since the HE_{1n} family

of modes can couple to plane waves with E-fields polarized in either X or Y

direction they are doubly degenerate and are often referred to as HE_{1n}^x and HE_{1n}^y

[24,43,45].

2.7.4 Diameter dependence of HE_{1n} resonance absorptance

The HE_{1n} resonances in nw arrays exhibit red-shift with increasing D. This

is due to nw radial boundary conditions. A simple expression of resonance peak

wavelength with respect to D can be derived by assuming that the evanescent field

is negligible outside the nw. We begin by recalling equation (2.80), which is the

boundary condition of the *z*-component of the E-field:

$$AJ_m(RT) - CK_m(R\tau) = 0 \qquad (2.123)$$

By assuming that the evanescent field is negligible, the above equation

simplifies to the following form for m = 1:

$$J_1(RT) = 0 \tag{2.124}$$

For ease of calculation, equation (2.124) can be approximated as a sine profile (as $J_1(\rho) = 0$ at $\rho = 0$) and a relationship between the resonance peak wavelength (λ_{HE1n}) and D can be derived using simple algebraic manipulation as follows:

$$sin(RT) = 0 \tag{2.125}$$

$$RT = n\pi; n = 1,2,3,\dots \tag{2.126}$$

$$R\frac{2\pi Re(\bar{n}_{eff})}{\lambda_{HE1n}} = n\pi \tag{2.127}$$

$$\lambda_{HE1n} = \frac{Re(\bar{n}_{eff})D}{n} \tag{2.128}$$

where D = 2*R and $Re(\bar{n}_{eff})$ is the real portion of the complex effective refractive index ($\bar{n}_{eff}$) of the mode. Equation (2.128) demonstrates that λ_{HE1n} is linearly dependent on D. As a result, with increasing D, λ_{HE1n} will red-shift. However, the slope of this red-shift will decrease with increasing radial mode index n.

2.8 Near-field coupling in cylindrical waveguide array

We have thus far solved the eigenvalue equation and investigated the radial mode field profiles of a single semi-infinitely long cylindrical step index waveguide. This is sufficient for sparse nw arrays [20]. However, to better

approximate a closely packed vertical nw array, we can likewise solve the eigenvalue equation of an array of semi-infinitely long cylindrical step index waveguides. As mentioned in the beginning of this chapter, the proximity of the waveguides will increase or decrease the influence of near-field coupling between neighbouring nw radial modes. This in turn will affect the eigenvalue equation of the step index dielectric waveguide [20].

For our analysis we will use the multipole method for deriving the eigenvalue equation for a cylindrical waveguide in a square array. Only nearest neighbour interactions are taken into account [20,26,48]. The derivation is similar to that presented by Sturmberg et al. for a cylindrical waveguide in a square array in the supplementary information of reference [53] for m = 1 mode order. The general multipole method for solving the Helmholtz equation for a periodic array is presented in references [26,63].

A square unit cell is assumed with side length equal to the array period P and a cylindrical waveguide at the center. This unit cell is translated by integer multiples of P in the 2D plane to reproduce the 2D array [26]. We now focus on the E_z field inside the unit cell and expand it inside the dielectric cylinder (indicated by subscript 1) in terms of Bessel functions of the first kind, since there are no singularities in the waveguide:

$$E_{z1}(\rho, \phi, z) = \sum_{m=-\infty}^{\infty} A_m^E J_m(\rho T) e^{jm\phi} e^{-j\beta z} \qquad (2.129)$$

Here, T is defined according to equation (2.71), i.e. $T^2 = k_1^2 - \beta^2$. The superscript E on the coefficient A refers to the E-field. Additionally, outside the cylinder (indicated by subscript 2), but within the unit cell, we can expand the E_z field in terms of the modified Bessel functions of the first ($I_m(\rho\tau)$) and second kind ($K_m(\rho\tau)$):

$$E_{z2}(\rho, \phi, z) = \sum_{m=-\infty}^{\infty} \left(B_m^E I_m(\rho\tau) + C_m^E K_m(\rho\tau) \right) e^{jm\phi} e^{-j\beta z} \qquad (2.130)$$

Here τ is defined according to equation (2.78), i.e. $\tau^2 = \beta^2 - k_2^2$. The H_z field inside and outside the cylindrical waveguide can also be expanded as follows within the unit cell:

$$H_{z1}(\rho, \phi, z) = \sum_{m=-\infty}^{\infty} A_m^H J_m(\rho T) e^{jm\phi} e^{-j\beta z} \qquad (2.131)$$

$$H_{z2}(\rho, \phi, z) = \sum_{m=-\infty}^{\infty} \left(B_m^H I_m(\rho\tau) + C_m^H K_m(\rho\tau) \right) e^{jm\phi} e^{-j\beta z} \qquad (2.132)$$

The superscript H on the coefficients A, B, and C refer to the H-field. The influence of the periodic lattice is summed up based on the following relation:

$$B_m^i = \sum_{n=-\infty}^{\infty} (-1)^{m+n} S_{m-n} C_n^i \qquad (2.133)$$

This is called the Dynamic Rayleigh Identity and a detailed derivation of this relationship is provided in references [26,63]. The relationship to first order (n = m) is:

$$B_n^i = S_0 C_n^i \qquad (2.134)$$

Here, S_0 is the zeroth order lattice sum that takes into account nearest neighbour interactions in a periodic array [20,26,48]. Also, S_0 depends only on the geometry of the array [26]. Now, we can use this relationship to reduce the number of independent coefficients of the E_z and H_z field expansions and utilize the electromagnetic boundary conditions, i.e. tangential components of E- and H-fields are continuous across a dielectric boundary (equations (2.79), (2.81), (2.83), and (2.85)), to arrive at the eigenvalue equation of a periodic array. We can write the mth mode order for the E_z and H_z field expansions inside and outside the waveguide, equations (2.129) to (2.132), as follows:

$$E_{z1}(\rho, \phi, z) = A_m^E J_m(\rho T) e^{jm\phi} e^{-j\beta z} \tag{2.135}$$

$$E_{z2}(\rho, \phi, z) = \left(K_m(\rho\tau) + S_0 I_m(\rho\tau)\right) C_m^E e^{jm\phi} e^{-j\beta z} \tag{2.136}$$

$$H_{z1}(\rho, \phi, z) = A_m^H J_m(\rho T) e^{jm\phi} e^{-j\beta z} \tag{2.137}$$

$$H_{z2}(\rho, \phi, z) = \left(K_m(\rho\tau) + S_0 I_m(\rho\tau)\right) C_m^H e^{jm\phi} e^{-j\beta z} \tag{2.138}$$

We can similarly write the mth mode order for the E_ϕ field inside and outside the cylindrical waveguide in the unit cell based on equation (2.57), which relates E_ϕ to E_z and H_z fields, as follows:

$$E_{\phi 1}(\rho, \phi, z) = \frac{j}{\beta^2 - k_1^2} \left[\frac{\beta}{\rho} \frac{\partial E_{z1}(\rho, \phi, z)}{\partial \phi} - \omega\mu \frac{\partial H_{z1}(\rho, \phi, z)}{\partial \rho} \right] \tag{2.139}$$

$$E_{\phi 1}(\rho, \phi, z) = -\frac{j}{T^2} \left[\frac{\beta}{\rho} jm J_m(\rho T) A_m^E \right.$$
$$\left. - \omega\mu_1 T J_m'(\rho T) A_m^H \right] e^{jm\phi} e^{-j\beta z} \tag{2.140}$$

$$E_{\phi2}(\rho,\phi,z) = \frac{j}{\beta^2 - k_2^2}\left[\frac{\beta}{\rho}\frac{\partial E_{z2}(\rho,\phi,z)}{\partial \phi} - \omega\mu\frac{\partial H_{z2}(\rho,\phi,z)}{\partial \rho}\right] \qquad (2.141)$$

$$E_{\phi2}(\rho,\phi,z) = \frac{j}{\tau^2}\left[\frac{\beta}{\rho}jm\big(K_m(\rho\tau) + S_0 I_m(\rho\tau)\big)C_m^E\right.$$

$$\left. - \omega\mu_2\tau\big(K_m'(\rho\tau) + S_0 I_m'(\rho\tau)\big)C_m^H\right]e^{jm\phi}e^{-j\beta z} \qquad (2.142)$$

Similarly, the mth mode order for H_ϕ field inside and outside the cylindrical waveguide in the unit cell based on equation (2.59), which relates H_ϕ to E_z and H_z fields, can be written as follows:

$$H_{\phi1}(\rho,\phi,z) = \frac{j}{\beta^2 - k_1^2}\left[\frac{\beta}{\rho}\frac{\partial H_{z1}(\rho,\phi,z)}{\partial \phi} + \omega\varepsilon\frac{\partial E_{z1}(\rho,\phi,z)}{\partial \rho}\right] \qquad (2.143)$$

$$H_{\phi1}(\rho,\phi,z) = -\frac{j}{T^2}\left[\frac{\beta}{\rho}jm J_m(\rho T)A_m^H\right.$$

$$\left. + \omega\varepsilon_1 T J_m'(\rho T)A_m^E\right]e^{jm\phi}e^{-j\beta z} \qquad (2.144)$$

$$H_{\phi2}(\rho,\phi,z) = \frac{j}{\beta^2 - k_2^2}\left[\frac{\beta}{\rho}\frac{\partial H_{z2}(\rho,\phi,z)}{\partial \phi} + \omega\varepsilon\frac{\partial E_{z2}(\rho,\phi,z)}{\partial \rho}\right] \qquad (2.145)$$

$$H_{\phi2}(\rho,\phi,z) = \frac{j}{\tau^2}\left[\frac{\beta}{\rho}jm\big(K_m(\rho\tau) + S_0 I_m(\rho\tau)\big)C_m^H\right.$$

$$\left. + \omega\varepsilon_2\tau\big(K_m'(\rho\tau) + S_0 I_m'(\rho\tau)\big)C_m^E\right]e^{jm\phi}e^{-j\beta z} \qquad (2.146)$$

We note here that the E- and H-field profiles inside the dielectric cylinder (e.g. E_{z1}, $E_{\phi1}$, H_{z1}, and $H_{\phi1}$ above) are similar to analogous field profiles for a single dielectric cylinder (e.g. equations (2.65), (2.67), (2.68), and (2.70)). Now we utilize the electromagnetic boundary conditions, that is the tangential components

of the E- and H-fields ($E_z(\rho,\phi,z)$, $H_z(\rho,\phi,z)$, $E_\phi(\rho,\phi,z)$, and $H_\phi(\rho,\phi,z)$) are

continuous across the dielectric cylinder boundary ($\rho = R$) [3,59]:

1. *z-component of E- and H-fields:*

The E_z field boundary condition at $\rho = R$ is:

$$E_{z1}(R,\phi,z) = E_{z2}(R,\phi,z) \tag{2.147}$$

$$C_m^E = \frac{J_m(RT)}{\left(K_m(R\tau) + S_0 I_m(R\tau)\right)} A_m^E \tag{2.148}$$

and the H_z field boundary condition at $\rho = R$ is:

$$H_{z1}(R,\phi,z) = H_{z2}(R,\phi,z) \tag{2.149}$$

$$C_m^H = \frac{J_m(RT)}{\left(K_m(R\tau) + S_0 I_m(R\tau)\right)} A_m^H \tag{2.150}$$

2. *φ-component of E- and H-fields:*

The E_ϕ field boundary condition at $\rho = R$ is:

$$E_{\phi 1}(R,\phi,z) = E_{\phi 2}(R,\phi,z) \tag{2.151}$$

$$-\frac{j}{T^2}\left[\frac{\beta}{R} jm J_m(RT) A_m^E - \omega\mu_1 T J_m'(RT) A_m^H\right] e^{jm\phi} e^{-j\beta z}$$

$$= \frac{j}{\tau^2}\left[\frac{\beta}{R} jm \left(K_m(R\tau) + S_0 I_m(R\tau)\right) C_m^E \right. \tag{2.152}$$

$$\left. - \omega\mu_2 \tau \left(K_m'(R\tau) + S_0 I_m'(R\tau)\right) C_m^H\right] e^{jm\phi} e^{-j\beta z}$$

Equation (2.152) can be reorganized by inserting the expression for the

coefficients C_m^E (equation (2.148)) and C_m^H (equation (2.150)) as follows:

$$-\frac{jm\beta}{\omega}\left[\frac{1}{(RT)^2}+\frac{1}{(R\tau)^2}\right]A_m^E$$

$$+\left[\frac{\mu_1}{RT}\frac{J_m'(RT)}{J_m(RT)}+\frac{\mu_2}{R\tau}\frac{\left(K_m'(R\tau)+S_0I_m'(R\tau)\right)}{\left(K_m(R\tau)+S_0I_m(R\tau)\right)}\right]A_m^H=0 \tag{2.153}$$

Similarly, the H_ϕ field boundary condition at $\rho=R$ is:

$$H_{\phi1}(R,\phi,z)=H_{\phi2}(R,\phi,z) \tag{2.154}$$

$$-\frac{j}{T^2}\left[\frac{\beta}{R}jmA_m^H+\omega\varepsilon_1T\frac{J_m'(RT)}{J_m(RT)}A_m^E\right]J_m(RT)e^{jm\phi}e^{-j\beta z}$$

$$=\frac{j}{\tau^2}\left[\frac{\beta}{\rho}jmA_m^H\right. \tag{2.155}$$

$$\left.+\omega\varepsilon_2\tau\frac{\left(K_m'(R\tau)+S_0I_m'(R\tau)\right)}{\left(K_m(R\tau)+S_0I_m(R\tau)\right)}A_m^E\right]J_m(RT)e^{jm\phi}e^{-j\beta z}$$

Here we have inserted the expression for the coefficients C_m^E (equation (2.148)) and C_m^H (equation (2.150)). Equation (2.155) can now be reorganized as follows:

$$-\left[\frac{\varepsilon_1}{RT}\frac{J_m'(RT)}{J_m(RT)}+\frac{\varepsilon_2}{R\tau}\frac{\left(K_m'(R\tau)+S_0I_m'(R\tau)\right)}{\left(K_m(R\tau)+S_0I_m(R\tau)\right)}\right]A_m^E$$

$$-\frac{jm\beta}{\omega}\left[\frac{1}{(RT)^2}+\frac{1}{(R\tau)^2}\right]A_m^H=0 \tag{2.156}$$

The two simultaneous homogeneous equations (2.153) and (2.156) can now be written in matrix form similar to equation (2.87):

$$\left[\begin{array}{cc}-\frac{jm\beta}{\omega}\left[\frac{1}{(RT)^2}+\frac{1}{(R\tau)^2}\right] & \left[\frac{\mu_1}{RT}\frac{J_m'(RT)}{J_m(RT)}+\frac{\mu_2}{R\tau}\frac{\left(K_m'(R\tau)+S_0I_m'(R\tau)\right)}{\left(K_m(R\tau)+S_0I_m(R\tau)\right)}\right] \\ -\left[\frac{\varepsilon_1}{RT}\frac{J_m'(RT)}{J_m(RT)}+\frac{\varepsilon_2}{R\tau}\frac{\left(K_m'(R\tau)+S_0I_m'(R\tau)\right)}{\left(K_m(R\tau)+S_0I_m(R\tau)\right)}\right] & -\frac{jm\beta}{\omega}\left[\frac{1}{(RT)^2}+\frac{1}{(R\tau)^2}\right]\end{array}\right]\left[\begin{array}{c}A_m^E \\ A_m^H\end{array}\right] \tag{2.157}$$

$$=0$$

Equating the determinant of the coefficient matrix to zero yields a non-trivial solution to the matrix equation (2.157). We now arrive at the following transcendental eigenvalue equation of the cylindrical waveguide array:

$$\left[\frac{\varepsilon_1}{RT}\frac{J'_m(RT)}{J_m(RT)} + \frac{\varepsilon_2}{R\tau}\frac{\left(K'_m(R\tau) + S_0 I'_m(R\tau)\right)}{\left(K_m(R\tau) + S_0 I_m(R\tau)\right)}\right]\left[\frac{\mu_1}{RT}\frac{J'_m(RT)}{J_m(RT)}\right.$$

$$\left.+ \frac{\mu_2}{R\tau}\frac{\left(K'_m(R\tau) + S_0 I'_m(R\tau)\right)}{\left(K_m(R\tau) + S_0 I_m(R\tau)\right)}\right] \tag{2.158}$$

$$-\left(\frac{m\beta}{\omega}\right)^2\left[\frac{1}{(RT)^2} + \frac{1}{(R\tau)^2}\right]^2 = 0$$

The perturbation term, S_0, in equation (2.158) takes into account the increased near-field coupling interaction between modes of neighbouring cylindrical waveguides [20]. In this scenario the modes can be best described as 2D photonic crystal modes that have similar field profiles to the radial modes of a single cylindrical dielectric waveguide [20]. As the lattice becomes sparse, the S_0 value becomes small and the near-field coupling between modes of neighbouring dielectric cylinders decreases [20]. In this limit, the modes of the eigenvalue equation of an infinitely long cylindrical waveguide (equation (88)) is sufficient to describe the radial modes in sparse cylindrical waveguide arrays [20]. In the extremely sparse limit, S_0 value approaches 0 and equation (2.158) converts to equation (2.88) for a single cylindrical step index dielectric waveguide [20,53]. Conversely, as the array becomes dense the magnitude of S_0 value increases [20].

Fountaine et. al. demonstrated that a positive S_0 value demonstrates constructive interference of the fields from neighbouring cylindrical waveguides at

the cylinder-cladding interface leading to a localized increase in the refractive index [20]. This causes a decrease in mode confinement and a red-shift of the resonance wavelength of the radial mode with respect to that of the radial mode of a single cylindrical waveguide [20]. Conversely, a negative S_0 value demonstrates destructive interference of the fields at the cylinder-cladding interface leading to a localized decrease in the refractive index [20]. This causes an increase in mode confinement and a blue-shift of the resonance wavelength of the radial mode with respect to that of the radial mode of a single cylindrical waveguide [20]. A further increase in magnitude of positive or negative S_0 value leads to further red- or blue-shift of the resonance wavelength of the radial mode with respect to that of the radial mode of a single cylindrical waveguide [20].

When correlating this observation with nw arrays for incident light parallel to the nw axis, it is observed that as the P decreases (array density increases) the resonance wavelengths of the HE_{1n} modes blue-shift. As stated above, this is because the increased near-field coupling between nws leads to destructive interference of the fields at the nw surface. This causes a localized decrease in the refractive index surrounding the nw interface which increases mode confinement. This overall effect results in the HE_{1n} resonance wavelength blue-shift. This correlates with the S_0 value becoming increasingly negative. Alternatively, an increase in P (increasing sparsity of nw arrays) shows a red-shift in resonance wavelength. This leads to a decrease in near-field coupling which in turn leads to a localized increase in refractive index due to constructive interference of the fields

at the nw interface. This causes a decrease in mode confinement which in turn results in the HE_{1n} resonance wavelength red-shift. This correlates with S_0 value becoming less negative. As the nws become sparse (D/P << 1) the rate of resonance red-shift with increasing P decreases until it no longer red-shifts. At this limit the nw behaves as a single dielectric waveguide and the S_0 value can be assumed to be zero.

In this chapter we have briefly reviewed radial modes in an infinite cylindrical dielectric waveguide. This topic is covered in more detail in references [21,22,24,59]. We then investigated the influence of near-field coupling between neighbouring cylindrical waveguides on the photonic crystal modes in a cylindrical waveguide array. Additional details on photonic crystal modes in 2D array are further explored in references [20,25,26,48,53]. A detailed derivation of the Rayleigh Identity in periodic structures is provided in references [26,63]. A short review on longitudinal cavity modes or F-P modes can be found in references [3,64]. Lastly, a rigorous theoretical discussion of light absorption along vertical nw axes after coupling to HE_{1n} radial modes is provided in appendix C of reference [36].

3 Simulation methodology

This chapter is divided into three subsections in order to review the optical simulation model setup of III-V nanowire (nw) arrays (GaAs, InP, InAs, and InSb) and InSb nanowire (nw) photodetector. First, a brief review of finite element method (FEM) is provided since FEM was used by COMSOL 3.5a software to simulate the nw array optical model. Second, the optical model subdomain conditions, boundary conditions, and measured parameters used in COMSOL software are presented. Lastly, the chapter ends by comparing simulated data with published experimental data for GaAs nw arrays [41].

3.1. Finite element method (FEM)

Interaction of light with vertical nw arrays can be modeled by specifying adequate boundary conditions to the Helmholtz equation of electric (E) field, $\vec{E}(\vec{r})$, and H-field, $\vec{H}(\vec{r})$. The Helmholtz equations for E- and H-fields are second order partial differential equations (PDE). In combination with specified nw array boundary conditions, the mathematical problem is referred to as a boundary value problem (BVP) [65]. The specific BVP described above cannot be solved analytically. However, numerical approaches can be utilized to arrive at approximate solutions to this BVP [66,67].

FEM is one such numerical approach, and it is utilized by COMSOL, to solve a BVP [65–70]. FEM technique solves a BVP by converting it to linear algebraic equations that yield approximate solutions. The procedure involves partitioning a continuous domain Ω governed by a BVP into smaller subdomains or elements. The shape of these elements in 3D can be specified as tetrahedral, hexahedral, pyramidal, or prismatic [71]. Thereafter, the solutions to the BVP are found by explicitly calculating the unknown function (that needs to be solved) at the vertices (nodes) of these elements. The calculated unknown functions in conjunction with basis functions, that interpolate non-nodal unknown function values inside the elements, are then summed together to approximate the solution of the BVP.

There are various methods for implementing FEM to solve a BVP, such as variational method, weighted residual method, etc. [67,72]. Detailed discussion on the different mathematical implementation of FEM are provided in references [65,67,68,70,73]. Although COMSOL's FEM implementation is much more involved [73], in order to provide a brief introduction to FEM, a simple overview is presented here by utilizing the weighted residual method with Galerkin's method. This simplified overview was adapted from references [67,72]. The following example of a general differential equation is considered for a domain Ω with specified boundary conditions:

$$L[\varphi(\vec{r})] = F(\vec{r}) \qquad\qquad (3.1)$$

Here, L is a linear differential operator, $\varphi(\vec{r})$ is an unknown function that needs to determined, and $F(\vec{r})$ is a source function. To implement the weighted residual method, we can rewrite equation (3.1) as $R(\vec{r}) = L[\varphi(\vec{r})] - F(\vec{r})$, multiply a weighting function $\Psi(\vec{r})$ to $R(\vec{r})$, and then integrate over Ω to arrive at the following relation:

$$\int_{\Omega} \Psi(\vec{r})R(\vec{r})d\Omega = 0 \tag{3.2}$$

$R(\vec{r})$ is called the residual and it measures how much a prospective $\varphi(\vec{r})$ satisfies equation (3.1) [70]. In cases where $\varphi(\vec{r})$ can be solved analytically, $R(\vec{r})$ = 0. However, in cases where $\varphi(\vec{r})$ cannot be determined analytically, an approximate solution $\varphi_D(\vec{r})$ can be used. In such a case, $R(\vec{r}) \neq 0$, and we seek a $\varphi_D(\vec{r})$ that will reduce $R(\vec{r})$ to the lowest possible value in Ω [67]. The goal of the weighted residual method is to find $\varphi_D(\vec{r})$ with the aid of chosen $\Psi(\vec{r})$ such that equation (3.2) is satisfied, thus ensuring the lowest possible $R(\vec{r})$ in Ω [67]. For simplicity we will define the above integrals in inner product notation:

$$\left(a(\vec{r}), b(\vec{r})\right) = \int_{\Omega} a(\vec{r})b(\vec{r})d\Omega \tag{3.3}$$

As a result, we can rewrite equation (3.2) as follows:

$$\left(\Psi(\vec{r}), R(\vec{r})\right) = 0 \tag{3.4}$$

We can now construct $\varphi_D(\vec{r})$ by partitioning Ω into m non-overlapping subdomains (elements) labeled $\Omega_{S1}, \Omega_{S2}, \cdots, \Omega_{Sm}$. This yields N nodal grid points, coinciding with the vertices of the element. $\varphi_D(\vec{r})$ can then be specified as the following sum:

$$\varphi_D(\vec{r}) = \sum_{j=1}^{N} \varphi_j N_j(\vec{r}) \tag{3.5}$$

Here, φ_j is the value of $\varphi(\vec{r})$ at node j and $N_j(\vec{r})$ is the basis (shape) function that allows for the interpolation of non-nodal values of $\varphi(\vec{r})$ inside the element based on the values of the φ_j at the nodes. $N_j(\vec{r})$ can be specified as polynomials of various orders or higher order functions [66–69,72]. Additionally, $N_i(\vec{r_j})$ is defined as zero at all other nodes except at the jth node with coordinates $\vec{r_j}$:

$$N_i(\vec{r_j}) = \begin{cases} 0; i \neq j \\ 1; i = j \end{cases} \tag{3.6}$$

Now, by inserting equation (3.5) into (3.4), we arrive at the following relation:

$$\left(\Psi(\vec{r}), L\left[\sum_{j=1}^{N} \varphi_j N_j(\vec{r}) \right] - F(\vec{r}) \right) = 0 \tag{3.7}$$

Although there are different choices of weighting function $\left(\Psi(\vec{r}) \right)$ we will select $\Psi(\vec{r})$ to be the same type of function as the shape function, $N_i(\vec{r})$ [67]. This approach is called Galerkin's method and yields the most precise solution [67]. Applying this modification, we arrive at the following relation:

$$\sum_{j=1}^{N} \left(N_i(\vec{r}), L\big[N_j(\vec{r})\big] \right) \varphi_j - \left(N_i(\vec{r}), F(\vec{r}) \right) = 0 \tag{3.8}$$

By substituting $a_{ij} = \left(N_i(\vec{r}), L\big[N_j(\vec{r})\big] \right) \varphi_j$, where $i, j = 1$ to N, and $b_i = \left(N_i(\vec{r}), F(\vec{r}) \right)$, where $i = 1$ to N, the above system of equations can be rewritten in the following short-hand notation:

$$\sum_{j=1}^{N} a_{ij}\varphi_j - b_i = 0 \tag{3.9}$$

This is the familiar matrix equation: $A \cdot x = B$, which can now be solved to determine φ_j at each node. To simplify the process, the system matrix A (also called stiffness matrix in reference to FEM's original application in structural mechanics [69]) and vector B (also called load vector) is more easily solved by summing together contributions from individual elements as follows:

$$a_{ij} = \sum_{\Omega_{Sk} \in \Omega} a_{ij}^{\Omega_{Sk}} = \sum_{\Omega_{Sk} \in \Omega} \left(N_i(\vec{r}), L\big[N_j(\vec{r})\big] \right)_{\Omega_{Sk}}$$

$$= \sum_{\Omega_{Sk} \in \Omega} \int_{\Omega_{Sk}} N_i(\vec{r}) L\big[N_j(\vec{r})\big] d\Omega \tag{3.10}$$

$$b_i = \sum_{\Omega_{Sk} \in \Omega} b_i^{\Omega_{Sk}} = \sum_{\Omega_{Sk} \in \Omega} \left(N_i(\vec{r}), F(\vec{r}) \right)_{\Omega_{Sk}} = \sum_{\Omega_{Sk} \in \Omega} \int_{\Omega_{Sk}} N_i(\vec{r}) F(\vec{r}) d\Omega \tag{3.11}$$

Here, $i, j = 1, ..., N_v$. N_v is the number of vertices (nodes) for a single element. Additionally, $a_{ij}^{\Omega_{Sk}} = 0$ unless N_i and N_j are from the same element Ω_{Sk}. The dimensions of these smaller matrices are N_v by N_v. This overall procedure of using

smaller element matrices to construct the general matrix by summing them together is referred to as assembly. This procedure reduces computational complexity for solving the system of equations to determine φ_j [72].

In the case of time harmonic E- and H-fields in Ω, the FEM is applied to the Helmholtz equations and the E- and H-field components are explicitly determined at each element node, and in conjunction with the shape functions are used to interpolate the E- and H-field components inside the elements [66,67,74].

Additionally, the accuracy of $\varphi_D(\vec{r})$ can be improved by increasing the number of discrete elements (reducing element size) in Ω or using higher order polynomials or functions to interpolate values of $\varphi_D(\vec{r})$ inside the elements while keeping the element sizes fixed [67,69]. Both of these procedures require an increase in computational resources and time [69].

3.2. Nanowire (nw) array optical model

After briefly reviewing FEM, the optical model set up for simulations performed in COMSOL 3.5a RF-module will be discussed in this section. Circular and hexagonal cross-section nanowires (nws) in a continuous square lattice array were simulated. This was achieved by constructing a unit cell geometry with square base and a nw of either hexagonal or circular cross-section of diameter (D) at the center. The unit cell base length is equal to the array period (P). Figure 3.1 shows a schematic image of a square nw array with hexagonal cross-section.
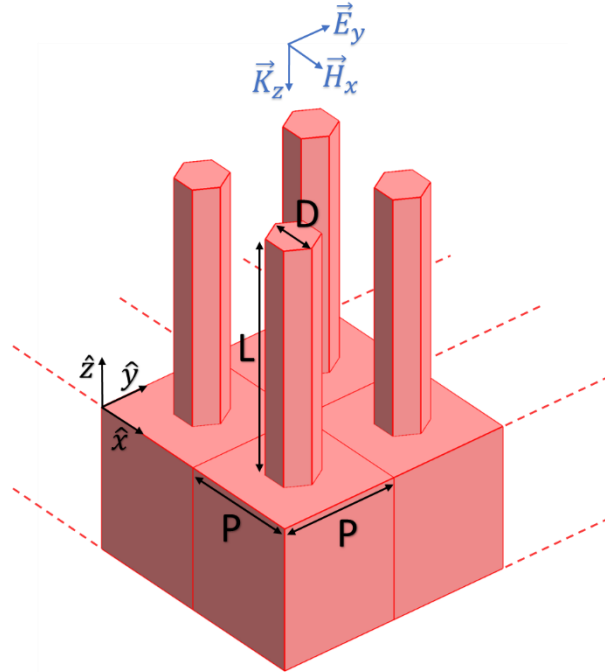
Figure 3.1. Schematic of a nw array of period (P), nw diameter (D), and nw length (L). Incident plane wave polarization and propagation direction are indicated.

The air above and the substrate below the nw array is assumed to extend to infinity. In order to simulate such an infinite medium above and below the nw array that are situated beyond the simulation domain of interest, a perfectly matched layer (PML) subdomain was used. A PML subdomain attenuates all incident waves without reflection from its interface [74,75]. This prevents the introduction of unnecessary simulation artifacts (e.g. unwanted reflections) into the simulated results from the outermost geometrical boundaries of the simulation model [75]. The location of the PML subdomains simulating infinite air and substrate are indicated in figure 3.2.

Finite GaAs, InP, InAs, and InSb nw arrays were simulated for select geometries using the same material type substrate or Si substrate (see figure 3.2 (a)). The specific substrate used is specified later while discussing the results. The substrate subdomain was constructed over a PML subdomain of the same material type. As mentioned above, this simulates a substrate that extends to infinity. For a subset of the simulation, the nw base was in direct contact with the PML subdomain and the total nw length of the simulation geometry was elongated (2000 nm for GaAs, InP, and InAs nw simulations and 10000 nm for InSb nw simulations) in order to avoid back reflection from the substrate and F-P modes along the nw axis (see figure 3.2 (b)). We refer to these nws as semi-infinite nws. These semi-infinite nws were simulated to identify the radial modes involved in nw resonance absorptance peaks and the change in nw resonance absorptance at various nw lengths (L) for varying D and P. It should be noted that the back reflection from the PML substrate and the F-P mode contribution to the nw absorptance are not completely eliminated using the above approach. Future studies can better simulate semi-infinite nws by ensuring that the subdomains vertically adjacent to the PML subdomain are index matched. Hence, complex refractive index ($\bar{n}(\lambda)$) in the PML subdomain should equal the $\bar{n}(\lambda)$ of the nw for regions of the PML $\leq$ D and $\bar{n}(\lambda)$ of air (or other medium between nws) for regions of the PML > D.
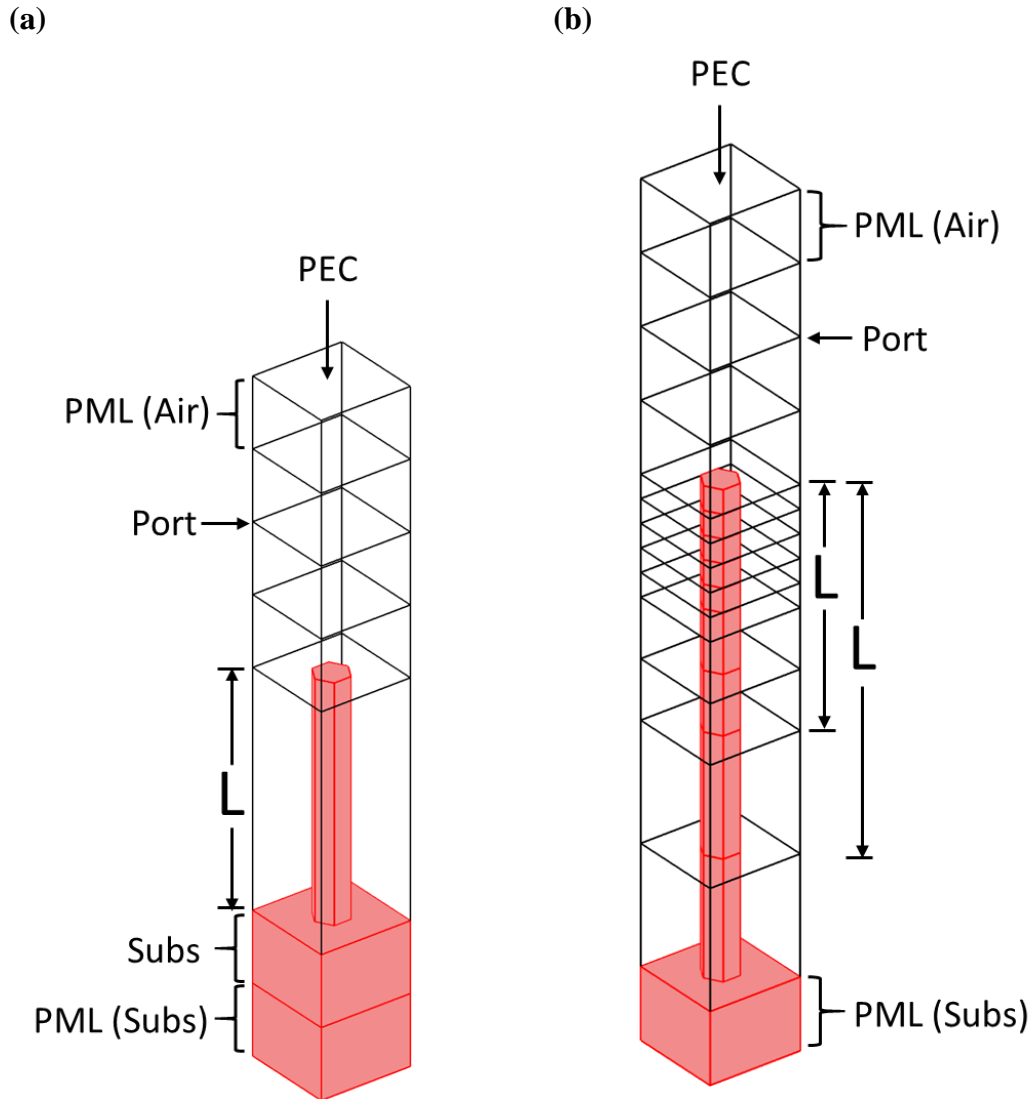
Figure 3.2. COMSOL schematic of a unit cell for (a) finite nw array and (b) semi-infinite nw array.

Periodic boundary conditions at the sidewalls of the unit cell were used to simulate a continuous 2D array of vertical nws. A perfect electric conductor (PEC) boundary condition was used at the topmost and bottommost outer boundary of the simulation geometry. This was done to ensure any unabsorbed tangential E-field to the PEC boundary in the PML subdomain was set to zero [74]. All internal

boundaries except port boundary were set as "continuity" which ensures tangential

$\vec{E}(\vec{r})$ and $\vec{H}(\vec{r})$ fields to the internal boundary are continuous across the boundary

[74].

The port boundary condition was declared over an "assembly pair" constructed above the nw and was set to generate Y-polarized electromagnetic waves at normal incidence to the nw top surface (see figure 3.2) [74]. For assembly ports, the incident field is generated from one side of the port while the scattered light from the nw passes through the port boundary to the other side without interacting with the port. The Air-PML subdomain is specified above the assembly pair. For the nw photodetector simulation, X-polarized and circularly polarized (left hand circular polarized, LHCP: $x + j \cdot y$ and right hand circular polarized, RHCP: $x - j \cdot y$) incident waves were also used for investigating nw absorptance.

The medium surrounding the nws was either set as air or bisbenzocyclobutene (BCB). BCB is a polymer commonly used to fill the voids between nws in practical devices [76]. The complex refractive index $\left(\bar{n}(\lambda) = n(\lambda) + j \cdot k(\lambda)\right)$ of air was assumed to be 1. Here $n(\lambda)$ is the real and $k(\lambda)$ is the imaginary part (extinction coefficient) of $\bar{n}(\lambda)$. Bulk $n(\lambda)$ and $k(\lambda)$ values for GaAs, InP, and InAs are plotted in figure 3.3 and InSb, BCB, Si, and Ni are plotted in figure 3.4. Optical data for intrinsic GaAs, InP, InAs, InSb and Si were obtained from Palik et al. [77], and Ni data was obtained from Rakic et al. [78,79]. The $\bar{n}(\lambda)$ for BCB was obtained experimentally and the $n(\lambda)$ is ~1.53 for $\lambda \geq 1$ μm [52]. All

material data was acquired at approximately 300 K. Quantum confinement effects

were neglected since all the simulated D and L were greater than 100 nm.

(a)

(b)
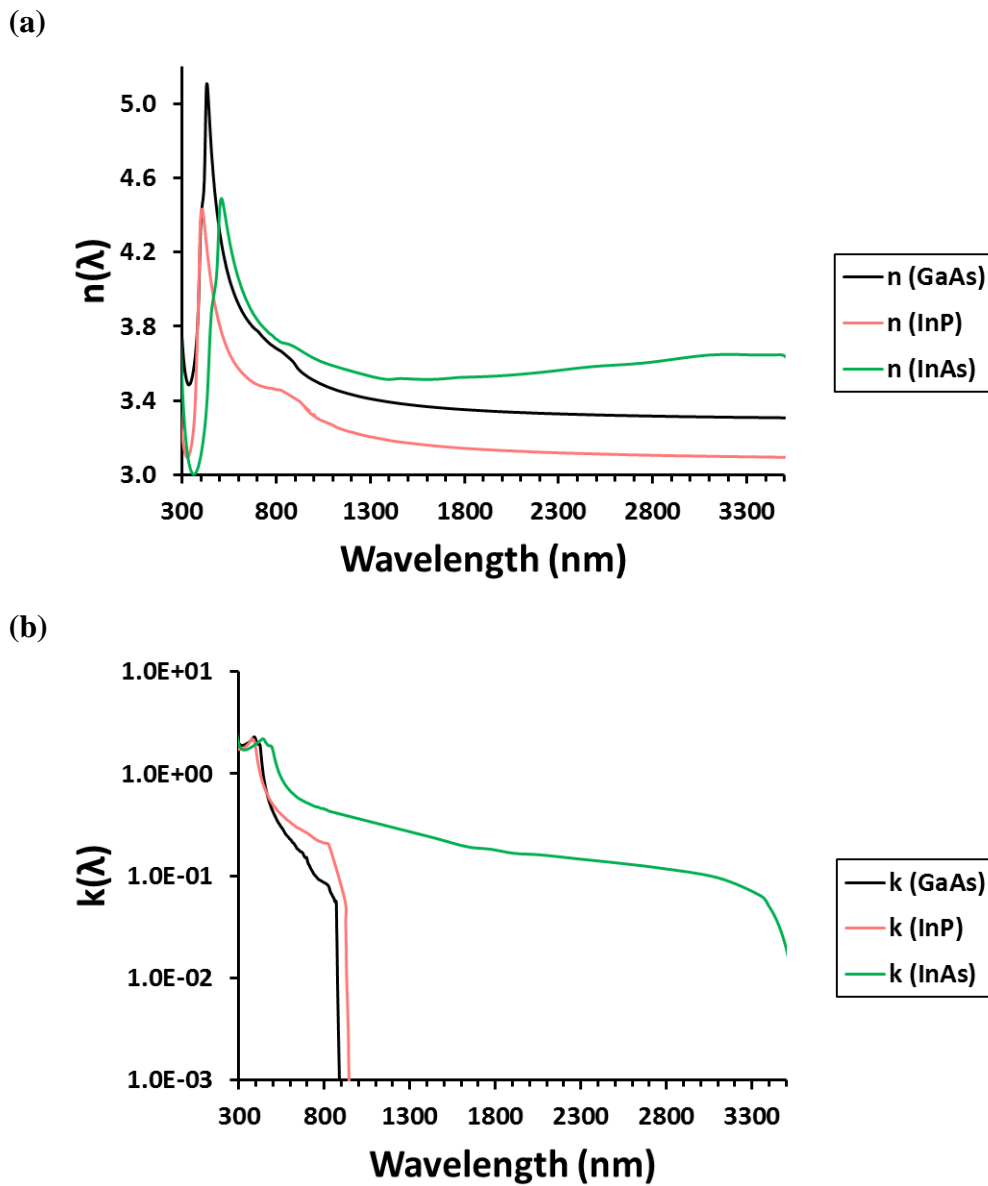
Figure 3.3. (a) $n(\lambda)$ and (b) $k(\lambda)$ part of $\bar{n}(\lambda)$ for GaAs, InP, and InAs.

(a)

(b)
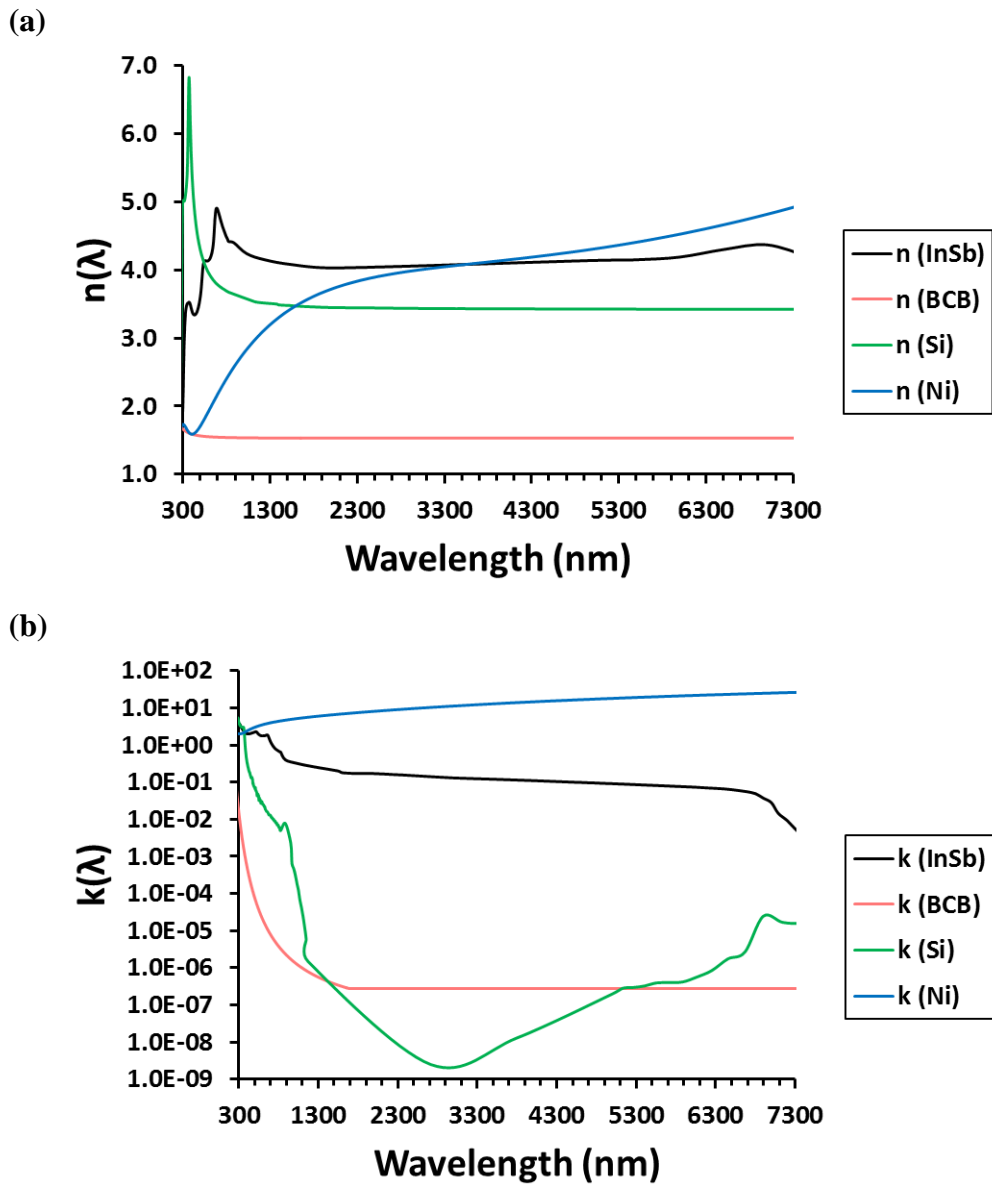
Figure 3.4. (a) $n(\lambda)$ and (b) $k(\lambda)$ part of $\bar{n}(\lambda)$ for InSb, BCB, Si, and Ni.

After setting up the boundary and subdomain conditions, the Helmholtz equations of time harmonic $\vec{E}(\vec{r})$ and $\vec{H}(\vec{r})$ fields, according to equations (3.12) and (3.13), were then solved using FEM for the aforementioned subdomain and boundary conditions in COMSOL:

$$\vec{\nabla} \times \left(\mu_r^{-1} \left(\vec{\nabla} \times \vec{E}(\vec{r}) \right) \right) = k_o^2 \bar{n}^2 \vec{E}(\vec{r}) \tag{3.12}$$

$$\vec{\nabla} \times \left((\bar{n})^{-2} \left(\vec{\nabla} \times \vec{H}(\vec{r}) \right) \right) = k_o^2 \mu_r \vec{H}(\vec{r}) \tag{3.13}$$

Here, k_o is the free space wavenumber and μ_r is the relative permeability. Since all simulated material components are assumed to be non-magnetic, μ_r is set to 1. The reflectance, $R(\lambda)$, from above the nws (between the assembly port and the top Air-PML) and transmittance, $T(\lambda)$, for specified lengths along the nw axis (for semi-infinite nws) or at the base of the nws (for finite nws) were then obtained. The nw absorptance, $A(\lambda)$, was then calculated for various wavelength ranges at 25 nm increments as follows:

$$A(\lambda) = 1 - R(\lambda) - T(\lambda) \tag{3.14}$$

Thin films were simulated using the same boundary and port conditions as the nw simulation geometry, but instead of the nw at the center of the unit cell, a cubic subdomain of either GaAs, InP, InAs, and InSb material was defined with the same dimensions as the unit cell. The same material PML subdomain was defined at the base of the thin film subdomain to simulate an infinite substrate. The thin film absorptance is then measured for specified depths (L) from the thin film surface.

For the InSb nw photodetector device model, a 2 nm ultrathin Ni metal film was also used as the contact layer to the top of the nws and the substrate was set as Si. The schematic of the device is shown in figure 3.5. The black horizontal lines indicate the location of the port and the location where $R(\lambda)$ and $T(\lambda)$ was measured.
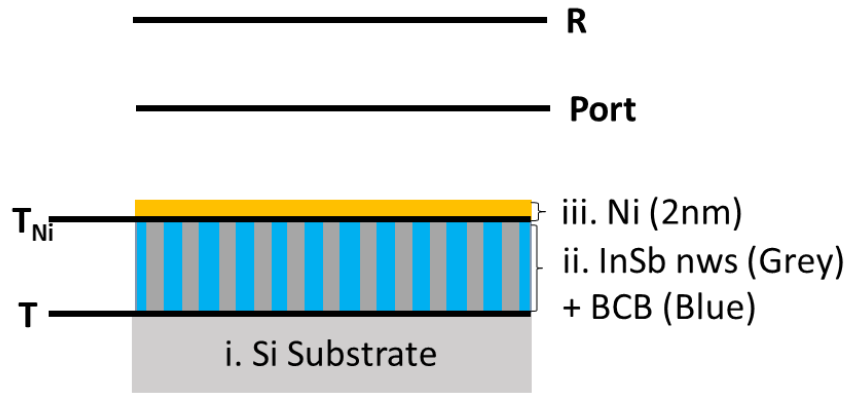
Figure 3.5. Schematic of the nw array photodetector device with Ni top contact, InSb nws in BCB, and Si substrate. The black horizontal lines indicate the regions at which transmittance ($T(\lambda)$) and reflectance ($R(\lambda)$) were measured and the location of the port.

The absorptance of the nw array ($A(\lambda)_{Active\ region}$, device active region) in the photodetector was calculated as follows:

$$A(\lambda)_{Active\ region} = A(\lambda)_{Total} - A(\lambda)_{Ni} \tag{3.15}$$

Here, $A(\lambda)_{Ni} = 1 - R(\lambda) - T(\lambda)_{Ni}$ is the absorptance of the Ni thin film and $A(\lambda)_{Total} = 1 - R(\lambda) - T(\lambda)$ is the total absorptance of the photodetector device, which includes Ni thin film and InSb nw array in BCB on Si. Due to the low $k(\lambda)$

of BCB (see figure 3.4) the absorptance in the BCB medium is considered negligible.

3.3. Comparison of simulation and experimental results

The validity of the optical model was tested by comparing GaAs nw array experimental reflectance data from reference [41] with simulated GaAs nanowire array reflectance data. The experimental reflectance data was measured by focusing light on a ~20 μm x 20 μm area on the center of the GaAs nw pads using a Filmetrics (F40) thin film profiler with a 10x microscope objective and numerical aperture (NA) of 0.25 [41]. Figure 3.6 shows the experimental reflectance data (solid line) from vertically etched GaAs nws of L = 1000 nm, P = 400 nm, and D from 65 nm to 125 nm.
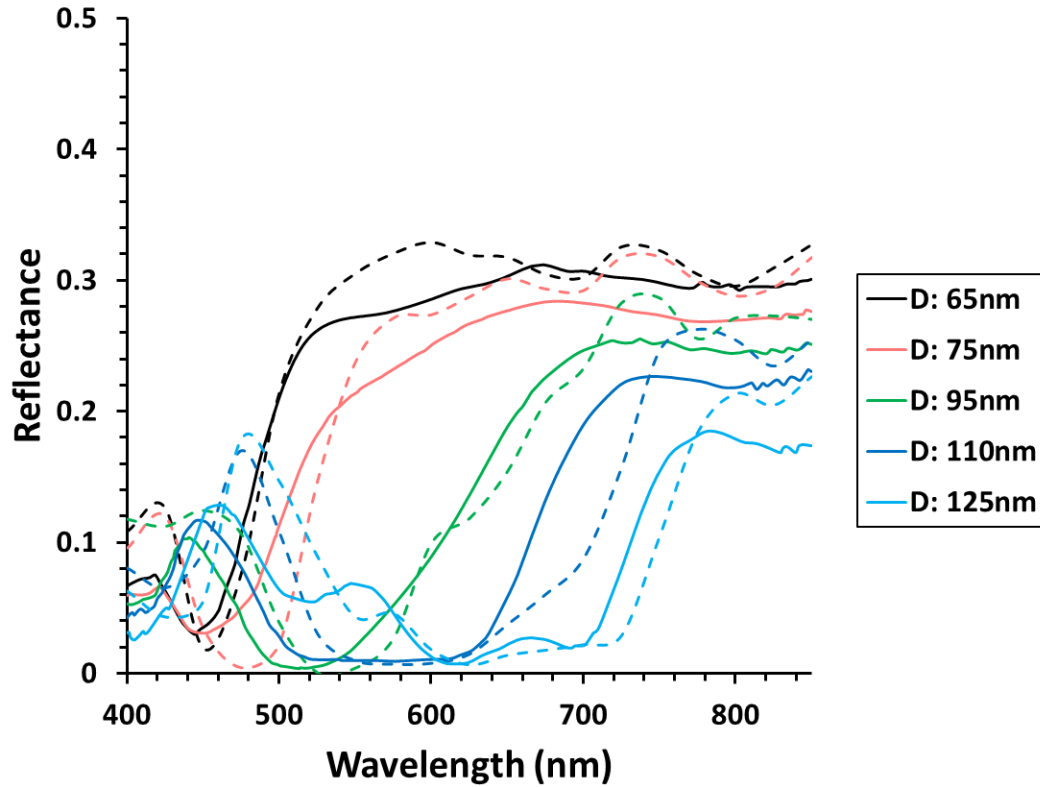
Figure 3.6. Experimental (solid) and simulated (dashed) reflectance curves for GaAs nws on GaAs substrate for P = 400 nm, D = 65 nm to 125 nm, and L = 1000 nm. The experimental data was acquired from reference [41].

The simulated reflectance data (dashed lines) from the COMSOL FEM optical model is overlaid onto the experimental reflectance data. The simulation data agrees well with the experimental data. Slight disparity between the experimental and simulated reflectance data and the lack of pronounced oscillations due to Fabry-Perot (F-P) mode resonances are observed in experimental reflectance data, especially at longer wavelengths. This results from the small NA of the microscope objective. Thus a fraction of the diffuse reflected light from the nw array is not collected [80]. In contrast, the simulation results account for the total

reflectance from the nw array, which consists of both specular and diffuse reflectance [80]. This accounts for the slight underestimation of the reflectance in the experimental reflectance data. Additionally, the experimental reflectance is an average reflectance from a range of incident angles ($0° \leq \theta < \sim14.5°$). This then averages the pronounced reflectance oscillations due to the F-P mode resonances, unlike the simulated reflectance which results from the incident light perfectly collimated at $0°$ normal incidence onto the nw array [80]. As observed from figure 3.6, the reflectance edge red-shifts with increasing D. As will be discussed in chapter 4, this is due to HE_{11} resonance red-shift with increasing D.

4 Wavelength-selective absorptance in GaAs, InP, and InAs nanowire (nw) arrays

Simulated photoabsorption in GaAs, InP, and InAs nanowire (nw) arrays are discussed in this chapter. Three known optical phenomena influence nw photoabsorption of incident light. These are radial mode resonances, near field evanescent wave coupling, and Fabry-Perot (F-P) mode resonances. The respective contributions of these optical phenomena will be investigated in this chapter for the aforementioned III-V nanowires (nws). The understanding of these optical phenomena are later used to optically model a wavelength selective nw photodetector in the upcoming chapters. Optical simulations were performed for hexagonal cross-section nws to mimic bottom-up fabricated III-V nws, which have hexagonal facets [81]. However, the results equally apply to circular cross-section nws, which are common for top-down fabricated nws [47,82], as will be shown at the end of this chapter. A square nw lattice was chosen for the simulation study and the medium surrounding the nw was air. Majority of the results presented in sections 4.1 to 4.5 of this chapter were previously published in Nanotechnology, titled: "Wavelength-selective absorptance in GaAs, InP and InAs nanowire arrays" [18].

4.1 Absorptance in III-V nw arrays

Contour plots of the absorptance in GaAs, InP and InAs nw arrays of various periods for a length of L = 1000 nm are shown in figures 4.1-4.3. The substrates are of the same material type as the nw for all data investigated in section 4.1. Each plot shows the absorptance over a range of wavelengths and diameters for a fixed period, P. For a given P and diameter, D, the nws generally exhibited a drastic increase in absorptance at two distinct wavelength regions. The strong absorptance near the long and short wavelengths can be attributed to the HE_{11} and HE_{12} radial mode resonances, respectively, as evidenced in section 4.2. As seen in figures 4.1-4.3, these resonance wavelengths red-shift with increasing D. Similar simulation and experimental studies have also reported the HE_{1n} family of radial mode resonances for circular cross-section nws [31,35,41,43].
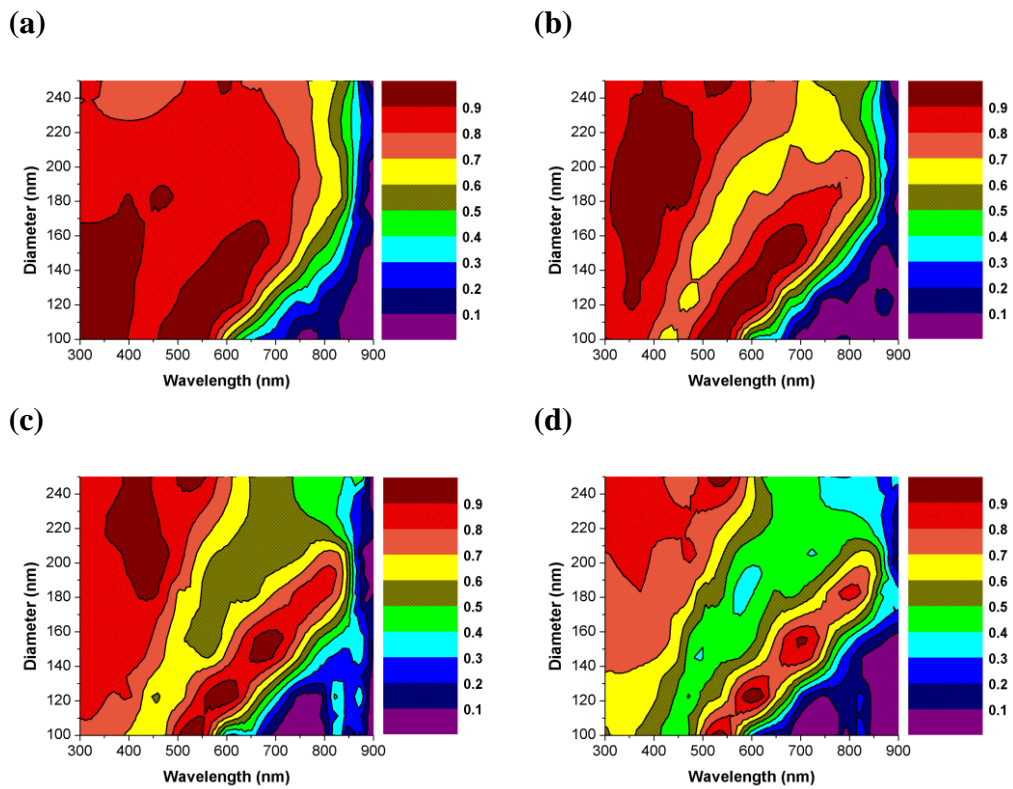
Figure 4.1. Absorptance of GaAs nw array for P of (a) 250 nm, (b) 330 nm, (c) 400 nm, and (d) 500 nm. L = 1000 nm.
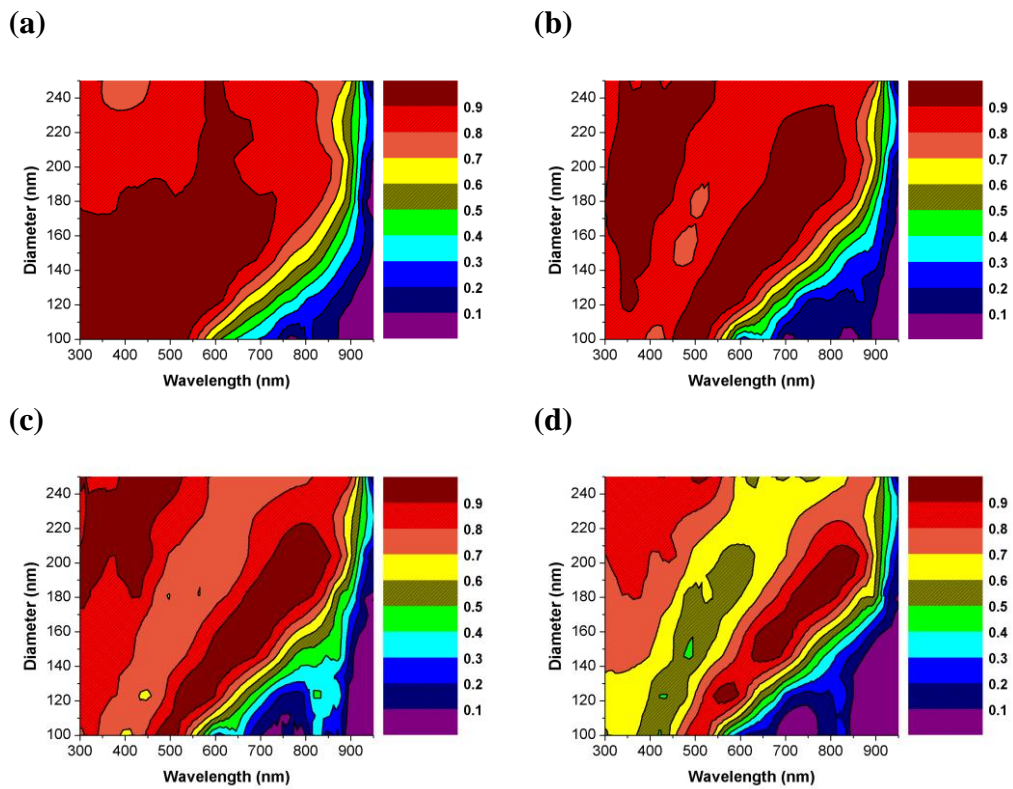
Figure 4.2. Absorptance of InP nw array for P of (a) 250 nm, (b) 330 nm, (c) 400 nm, and (d) 500 nm. L = 1000 nm.
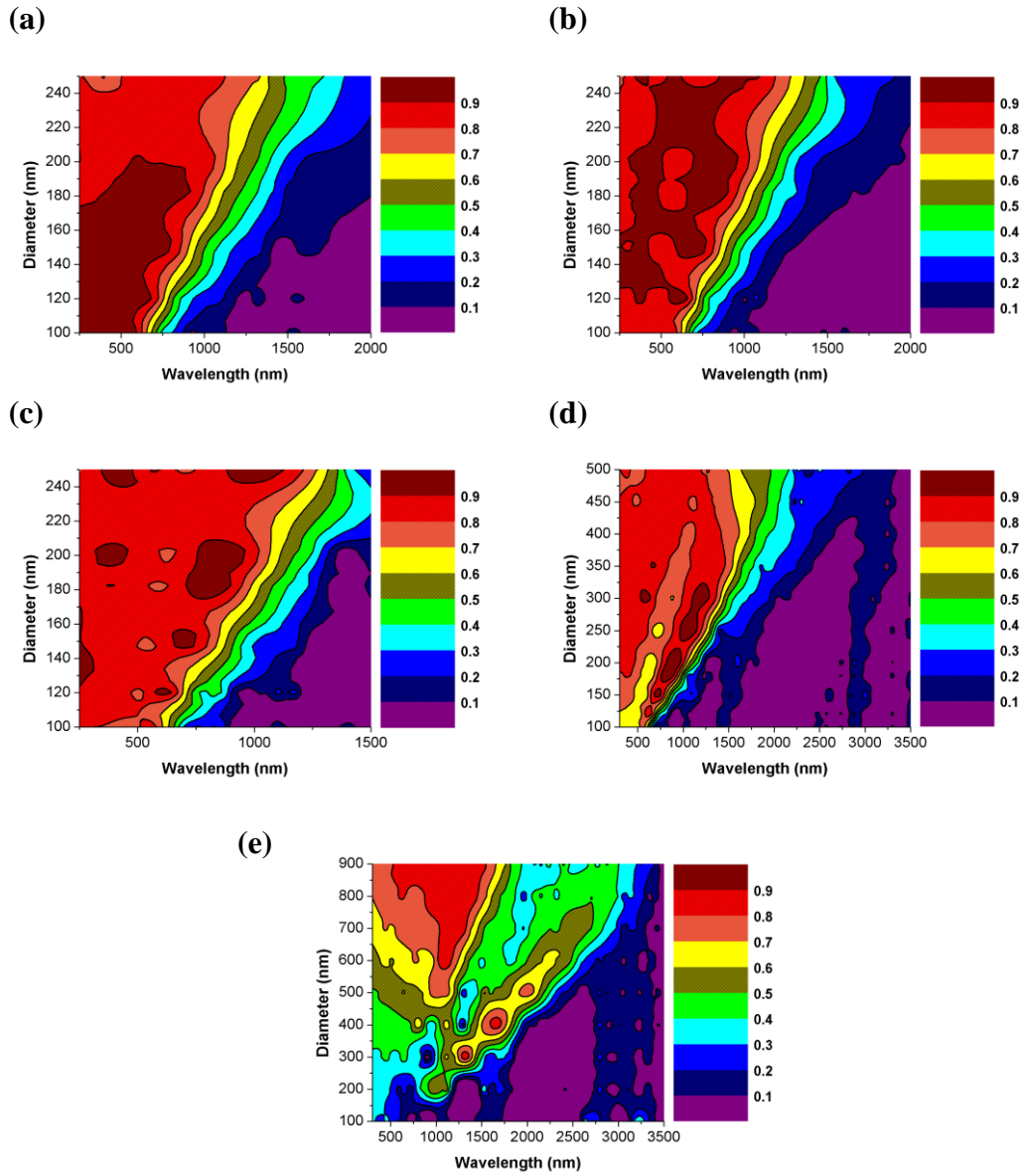
Figure 4.3. Absorptance of InAs nw array for P of (a) 250 nm, (b) 330 nm, (c) 400 nm, (d) 500 nm, and (e) 1000 nm. L = 1000 nm.

Figure 4.4 plots the absorptance for each material (GaAs, InP, and InAs) at the HE_{11} resonance wavelength for different D (indicated by data points) and different P (indicated by lines) for L = 1000 nm. As the HE_{11} resonance wavelength red-shifts with increasing D its contribution to nw absorptance concomitantly decreases. Eventually the HE_{11} resonance peak absorptance diminishes when the HE_{11} resonance peak moves into the bandgap region of the respective materials. This transition of the HE_{11} resonance into the nw material bandgap determines the maximum D for the existence of HE_{11} absorptance peak for that material. The decrease in the absorptance near the bandgap can be attributed to decreasing extinction coefficient ($k(\lambda)$; as shown in figure 3.3) with increasing wavelength, increasing reflectance from the nw top surface area as diameter to period ratio (D/P) increases, and increasing near field coupling with increasing D/P (to be discussed further in section 4.4). It is further observed that as the nw D/P decreases below ~1/3, the HE_{11} peak absorptance also decreases. This decrease in absorptance is due to a low fill factor of the nws. As a result, a larger fraction of incident light flux passes through the nw array to the substrate without coupling into the nw. Additionally, for D/P << 1 the HE_{11} resonance does not vary with P, e.g. for D = 100 nm in figure 4.4. This is due to negligible near-field coupling between modes of neighbouring nws.
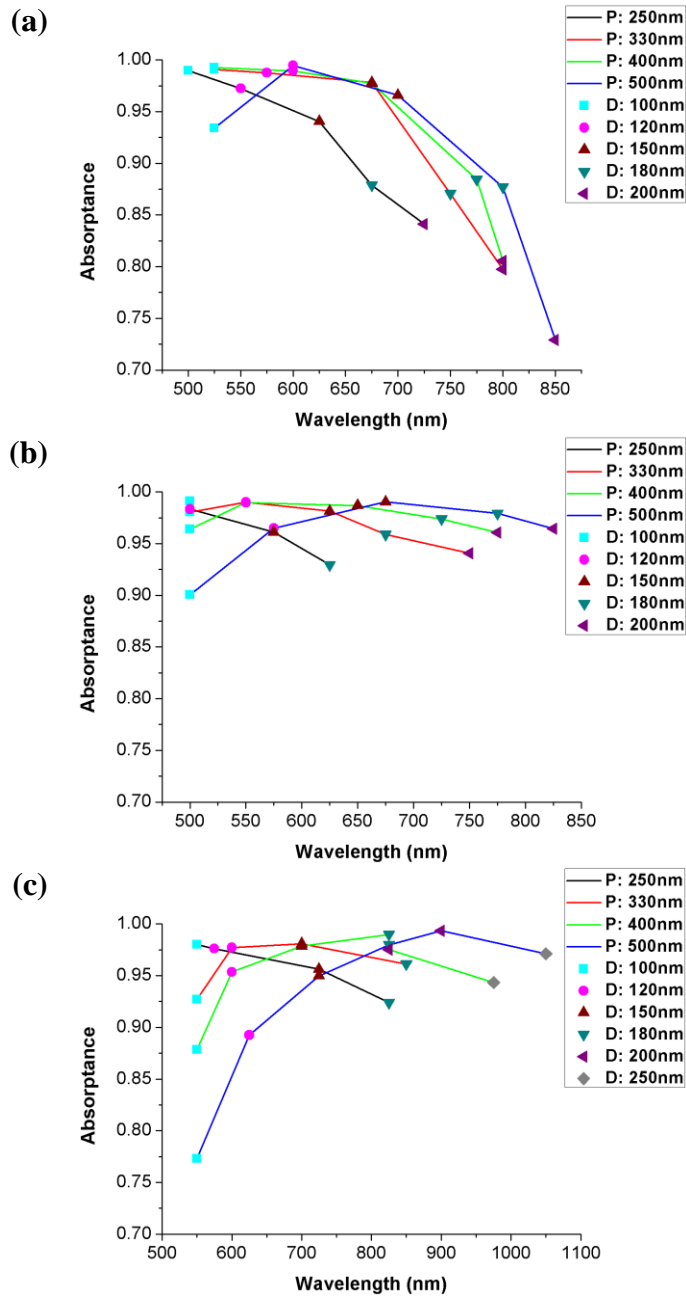
Figure 4.4. (a) GaAs, (b) InP, and (c) InAs HE_{11} radial mode resonance peak absorptance versus the resonance peak wavelength for different P (indicated by lines) and D (indicated by data points) at L = 1000 nm.

The radial (x-y) and axial (x-z) cross-sectional profiles of the energy density at the HE_{11} resonance wavelength ($\lambda = 700$ nm for GaAs, $\lambda = 675$ nm for InP, and $\lambda = 725$ nm for InAs) and HE_{12} resonance wavelength ($\lambda = 375$ nm) are shown in figure 4.5 and figure 4.6 for GaAs, InP, and InAs nws with D = 150 nm, P = 500 nm, and L = 1000 nm. The radial cross-section was taken at a position along the nw axis where the energy density was maximum. In all cases, the HE_{11} energy density profile was maximum near the nw tip and decreased rapidly along the nw axis due to absorption. This indicates that light is strongly coupled into the nw and attenuated. On the other hand, the HE_{12} energy density oscillated along the nw axis with minor attenuation compared to that observed for HE_{11} resonance. The oscillation is due to weaker coupling of light to the HE_{12} mode at D = 150 nm. As a result, incident light interferes with the reflected light from the substrate leading to longitudinal standing waves or F-P modes [80]. The energy density at the HE_{11} resonance (figure 4.5) was maximum at the nw center, while at the HE_{12} resonance (figure 4.6) it was maximum near the nw radial boundary and minimum at the center indicating insufficient transverse field confinement. The radial energy density profile for both HE_{11} and HE_{12} radial mode resonances were oriented along the polarization axis of the incident light wave, as confirmed in figure 4.7.
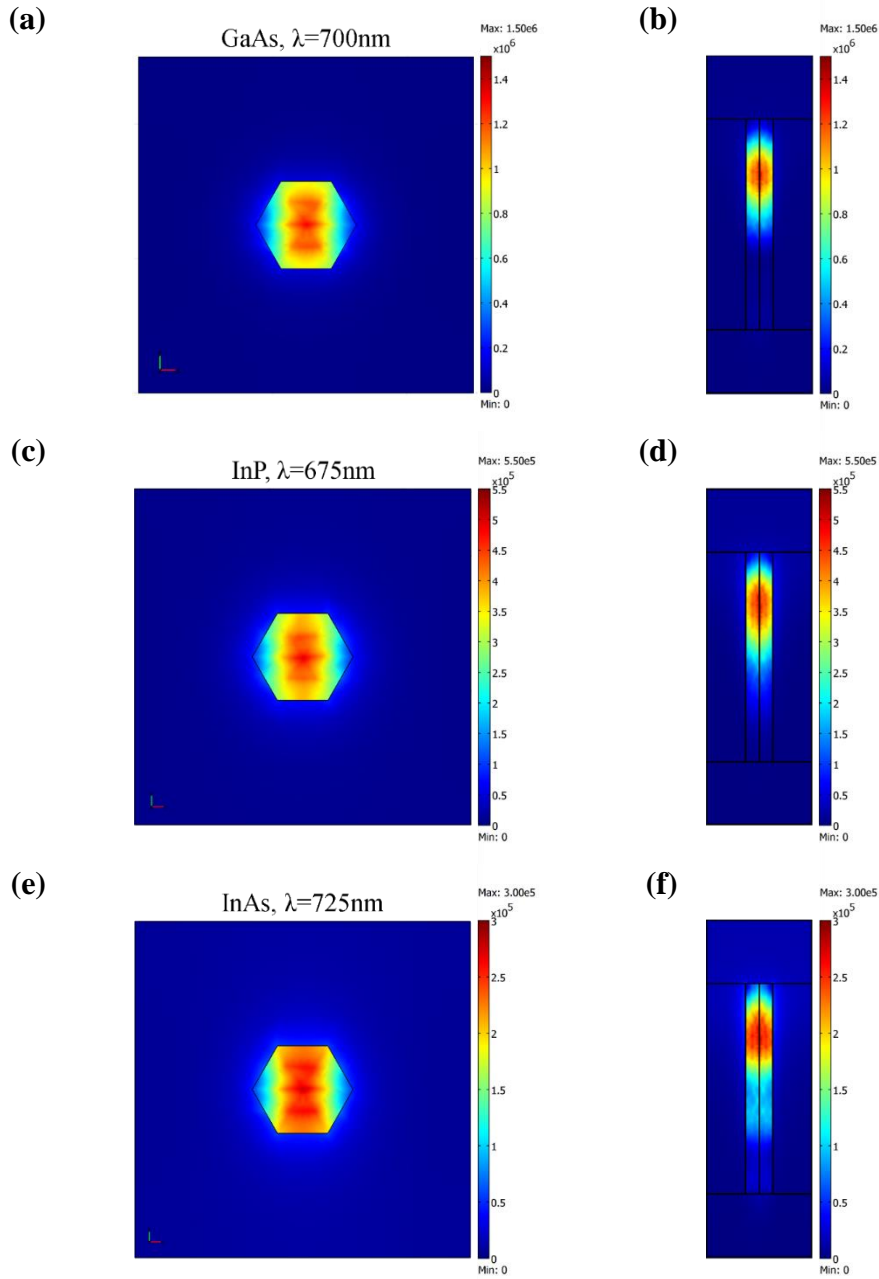
Figure 4.5. (a, b) GaAs, (c, d) InP, and (e, f) InAs energy density profiles along (a, c, e) radial (x-y) and (b, d, f) axial (x-z) cross-sections at the HE_{11} resonance wavelength ($\lambda = 700$ nm for GaAs, $\lambda = 675$ nm for InP, and $\lambda = 725$ nm for InAs) for D = 150 nm, P = 500 nm, and L = 1000 nm. The energy density is in units of J/m^3.
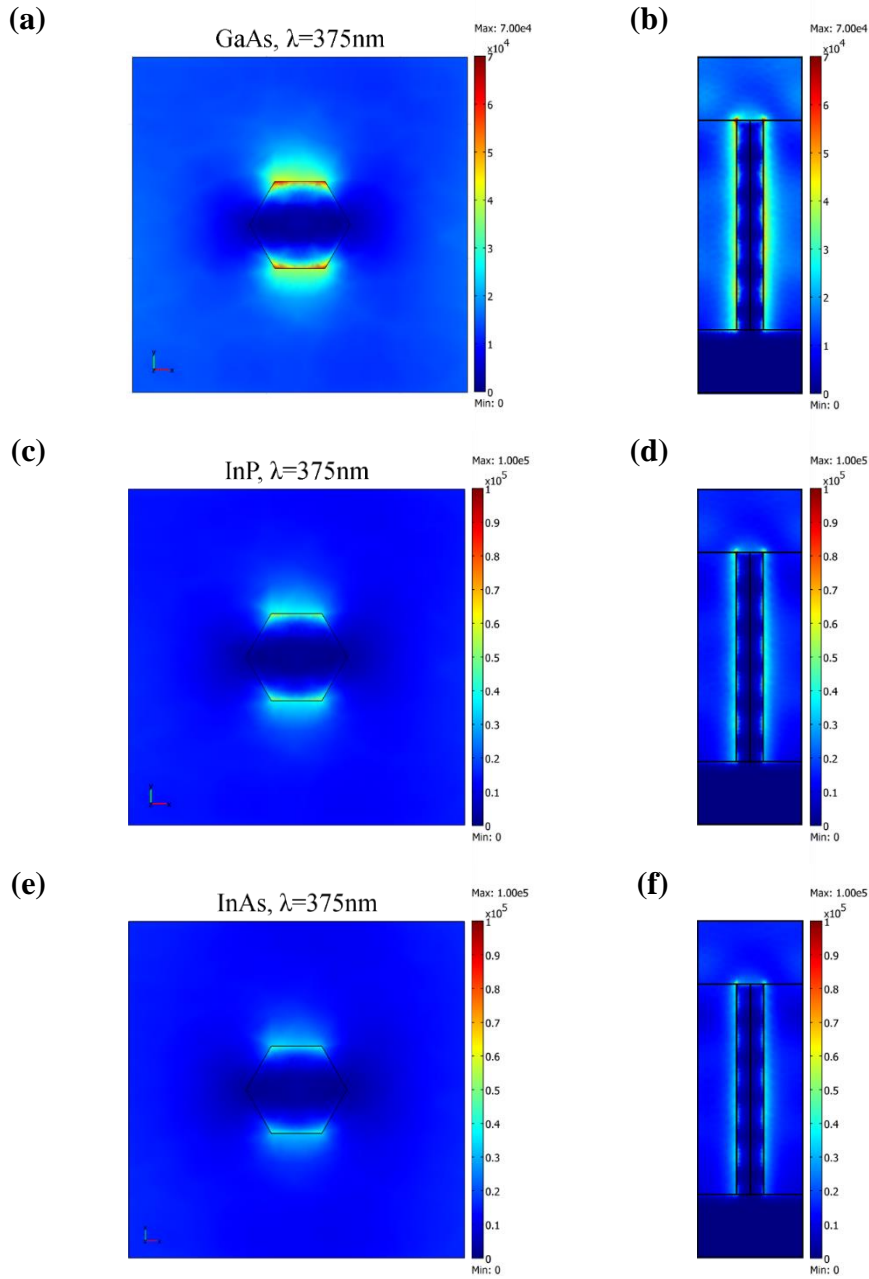
Figure 4.6. (a, b) GaAs, (c, d) InP, and (e, f) InAs energy density profiles along (a, c, e) radial (x-y) and (b, d, f) axial (x-z) cross-sections at the HE_{12} resonance wavelength (λ = 375 nm for GaAs, InP, and InAs) for D = 150 nm, P = 500 nm, and L = 1000 nm. The energy density is in units of J/m^3.

(a)   **(b)**
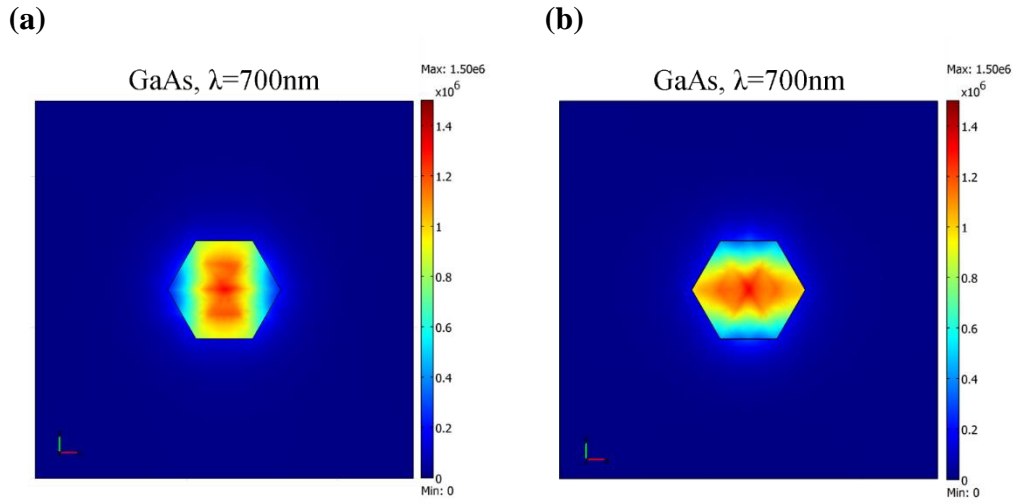
Figure 4.7. The radial (x-y) energy density profile of the HE_{11} mode in GaAs nw for (a) Y-polarized and (b) X-polarized normal incident light for D = 150 nm, P = 500 nm, and L = 1000 nm. The energy density is in units of J/m^3.

For larger D, the incident light, in addition to coupling strongly with the HE_{11} radial mode, also strongly couples to the HE_{12} radial mode. In both scenarios, if the HE_{1n} radial mode resonance peaks are within the bandgap of the nw material, coupled light is also strongly attenuated along the nw axis. As an example, figure 4.8 shows strong coupling and attenuation of incident light to the HE_{12} radial mode for D = 300 nm for GaAs nw. In such a scenario the energy density profile along the nw axis for HE_{12} radial mode resonance is similar to HE_{11} radial mode resonance energy density profile in figure 4.5 (b). Figure 4.8 also indicates that the energy density profile is a maximum at the center of the nw radial cross-section, which is representative of strong transverse field confinement.
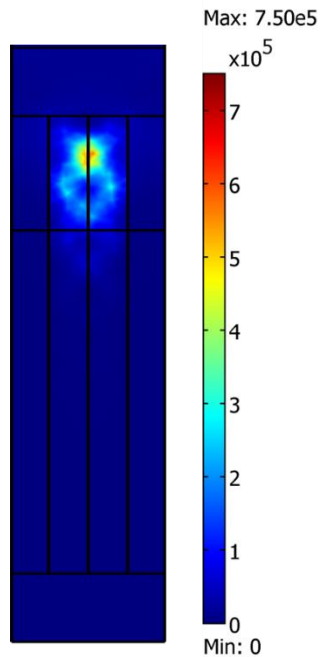
Figure 4.8. GaAs energy density profile along axial (x-z) cross-section at the HE_{12} resonance wavelength ($\lambda = 600$ nm) for D = 300 nm, P = 500 nm, and L = 2000 nm on perfectly matched layer (PML) substrate (semi-infinite nw). The energy density is in units of J/m^3.

4.2 Radial mode contribution to nw absorptance

The ability of III-V nws to support radial modes stems from the large refractive index difference between III-V nws and the surrounding air medium in conjunction with the incident light wavelength falling within the nanophotonic regime, i.e. $\lambda \sim D$ [83]. In finite nws the radial modes overlap with the F-P modes. These two effects can be decoupled using semi-infinite nws where F-P modes are absent due to the addition of a perfectly matched layer (PML) substrate at the base of the nw. This decoupling allows for a clearer identification of the radial modes involved in the nw absorptance. Semi-infinite nws were simulated for P = 500 nm and D = 100 nm to 300 nm for GaAs, InP, and InAs nws. The nw absorptance at L = 500 nm from the nw tip of the respective materials are shown in figure 4.9. The absorptance in a thin film of the same material and thickness (500 nm) is also shown for comparison.
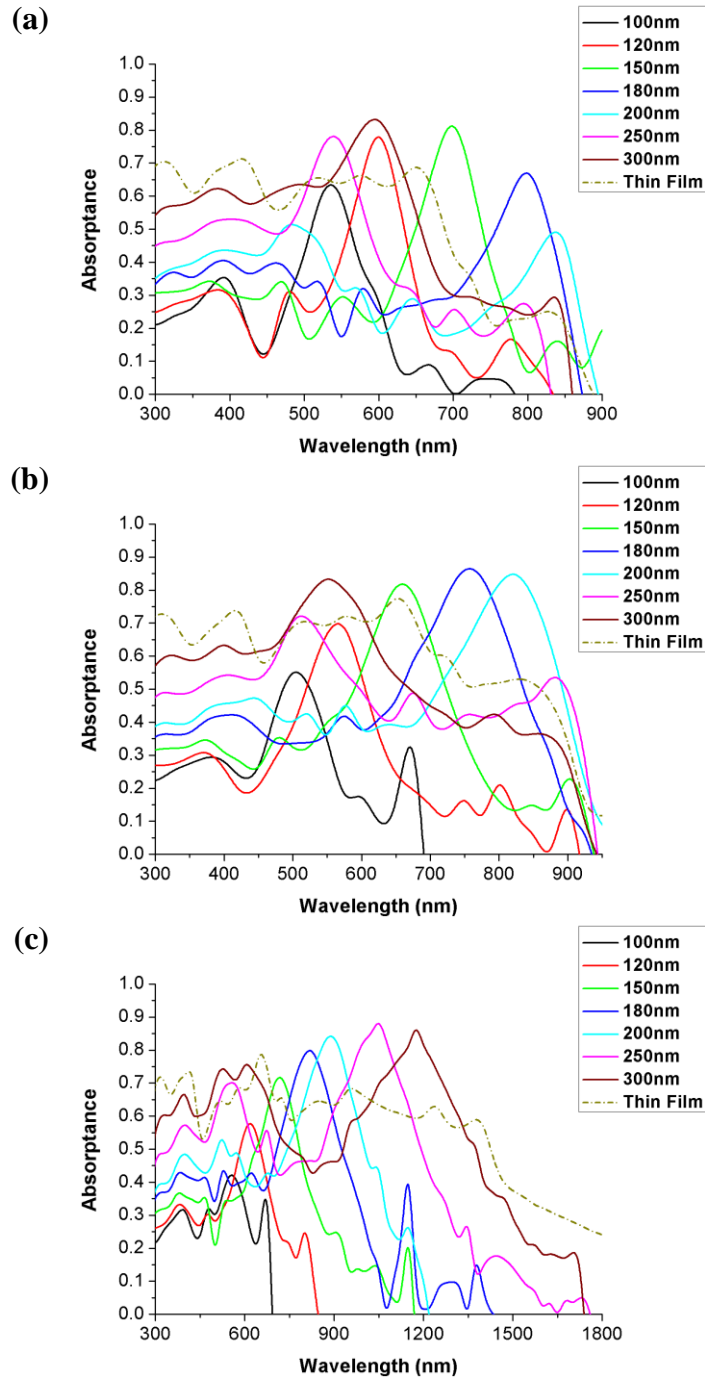
Figure 4.9. Absorptance at L = 500 nm from nw tip in semi-infinite nws for D = 100 nm to 300 nm for (a) GaAs, (b) InP, and (c) InAs nws. P = 500 nm. The thin film absorptance of equal thickness is also shown for comparison.

The nw absorptance remarkably exceeded that of the thin film near certain absorptance peaks in the spectrum. Radial cross-sectional profiles of the six field components of electric (E) and H-field (namely E_x, E_y, E_z, H_x, H_y, and H_z), shown in figures 4.10 to 4.15, identify these absorptance peaks as HE_{11} or HE_{12} radial modes, respectively. Linearly polarized light, incident parallel to the nw axis, have been shown to only couple with the HE_{1n} family of radial modes due to symmetry arguments (see section 2.7.3) [20,25,36,43,80]. It is further observed in figure 4.9 that for smaller diameters, incident light strongly couples to the HE_{11} mode only. But as the diameter increases in excess of 200 nm the incident light also strongly couples to the HE_{12} mode (figure 4.9). Additionally, light still strongly couples to the HE_{11} mode even after it has moved into the bandgap region. However, in this case the coupled light is guided through the nw with negligible attenuation, and at the nw-substrate boundary it is partly transmitted into the substrate and the remainder is reflected back into the nw.
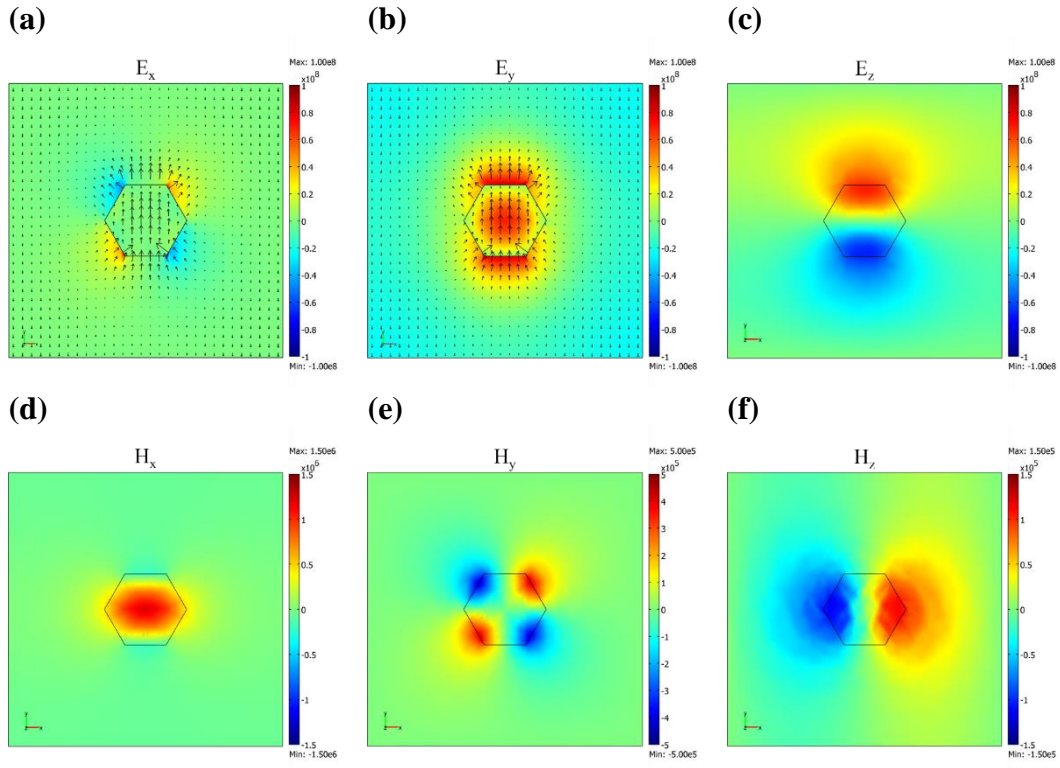
Figure 4.10. Field components (a) E_x, (b) E_y, (c) E_z, (d) H_x, (e) H_y, and (f) H_z at λ = 700 nm in GaAs nws of D = 150 nm and P = 500 nm. They correspond with the HE$_{11}$ mode. The E- and H-field component magnitudes are in units of V/m and A/m. Electric field vectors are shown in (a) and (b).

(a)

(b)

(c)

(d)

(e)

(f)
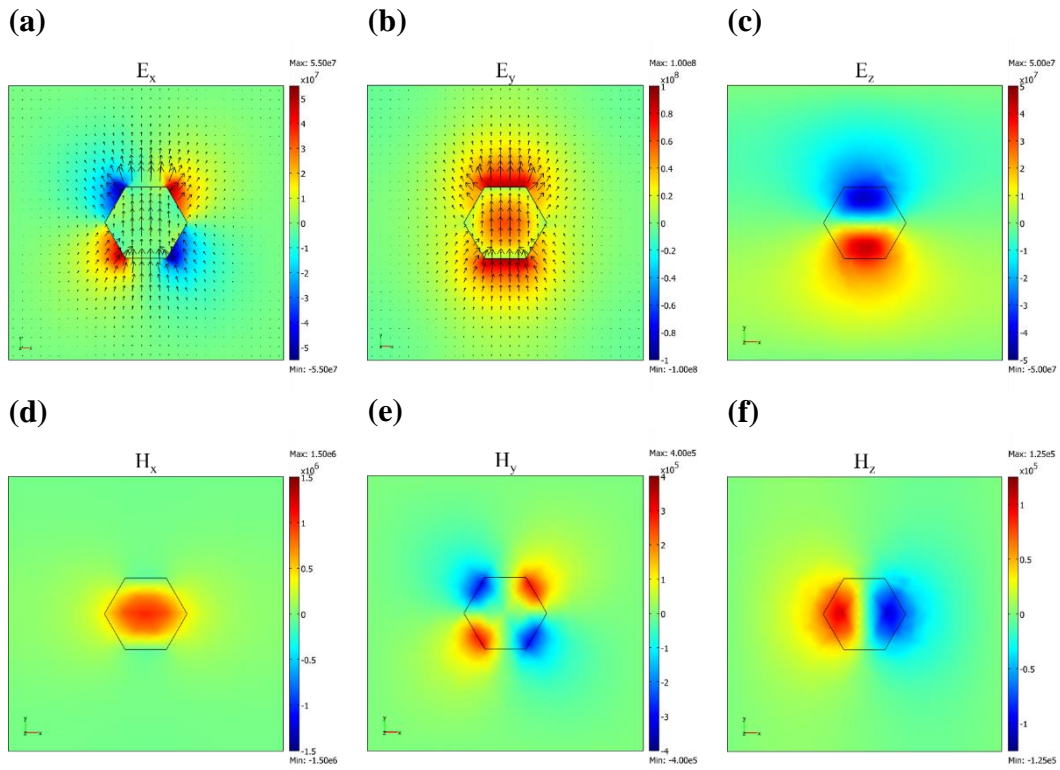
Figure 4.11. Field components (a) E_x, (b) E_y, (c) E_z, (d) H_x, (e) H_y, and (f) H_z at λ = 650 nm in InP nws of D = 150 nm and P = 500 nm. They correspond with the HE$_{11}$ mode. The E- and H-field component magnitudes are in units of V/m and A/m. Electric field vectors are shown in (a) and (b).

(a)

(b)

(c)

(d)

(e)

(f)
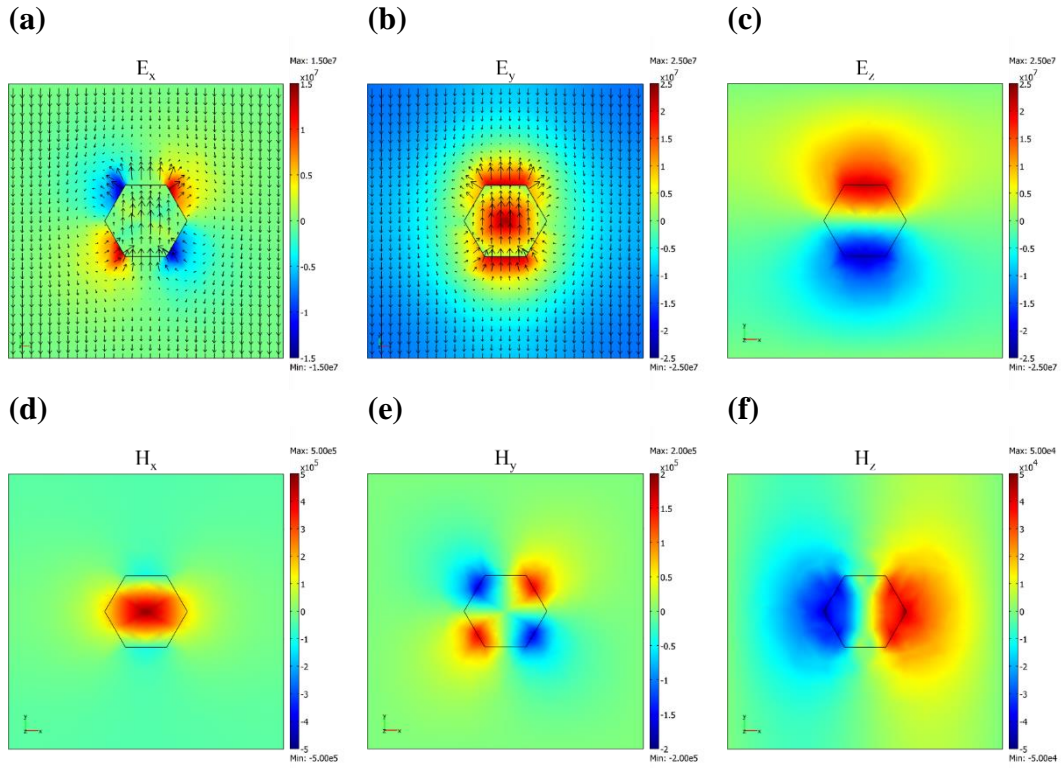
Figure 4.12. Field components (a) E_x, (b) E_y, (c) E_z, (d) H_x, (e) H_y, and (f) H_z at λ = 725 nm in InAs nws of D = 150 nm and P = 500 nm. They correspond with the HE_{11} mode. The E- and H-field component magnitudes are in units of V/m and A/m. Electric field vectors are shown in (a) and (b).
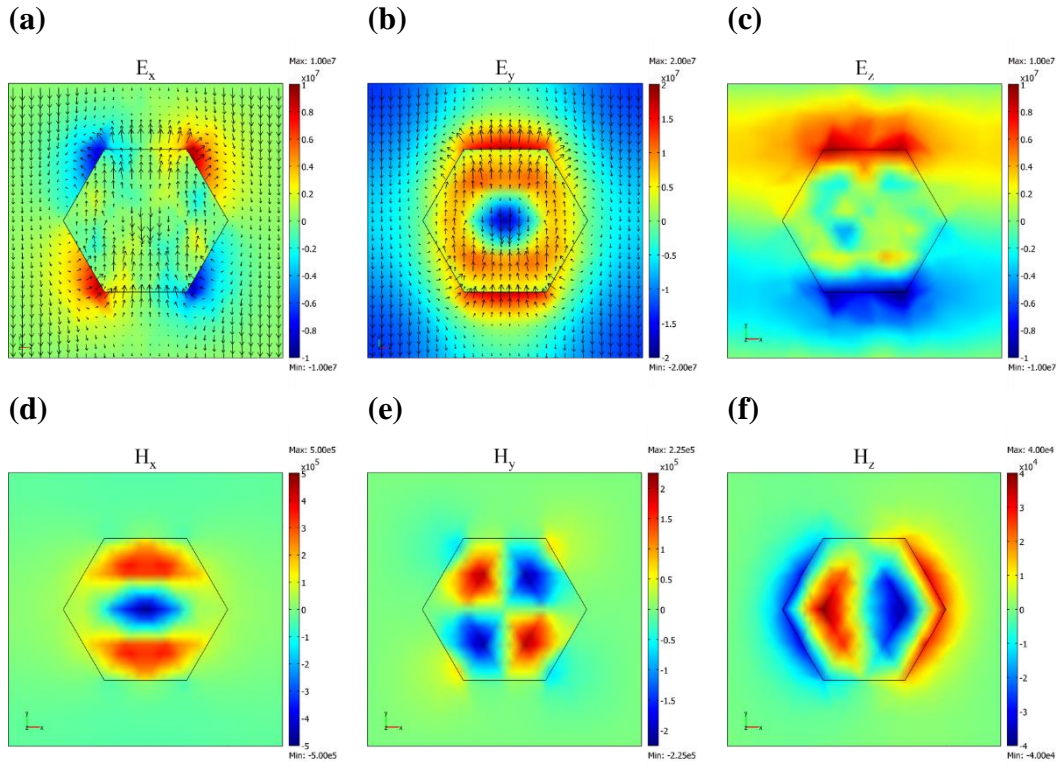
Figure 4.13. Field components (a) E_x, (b) E_y, (c) E_z, (d) H_x, (e) H_y, and (f) H_z at λ = 600 nm in GaAs nws of D = 300 nm and P = 500 nm. They correspond with the HE$_{12}$ mode. The E- and H-field component magnitudes are in units of V/m and A/m. Electric field vectors are shown in (a) and (b).
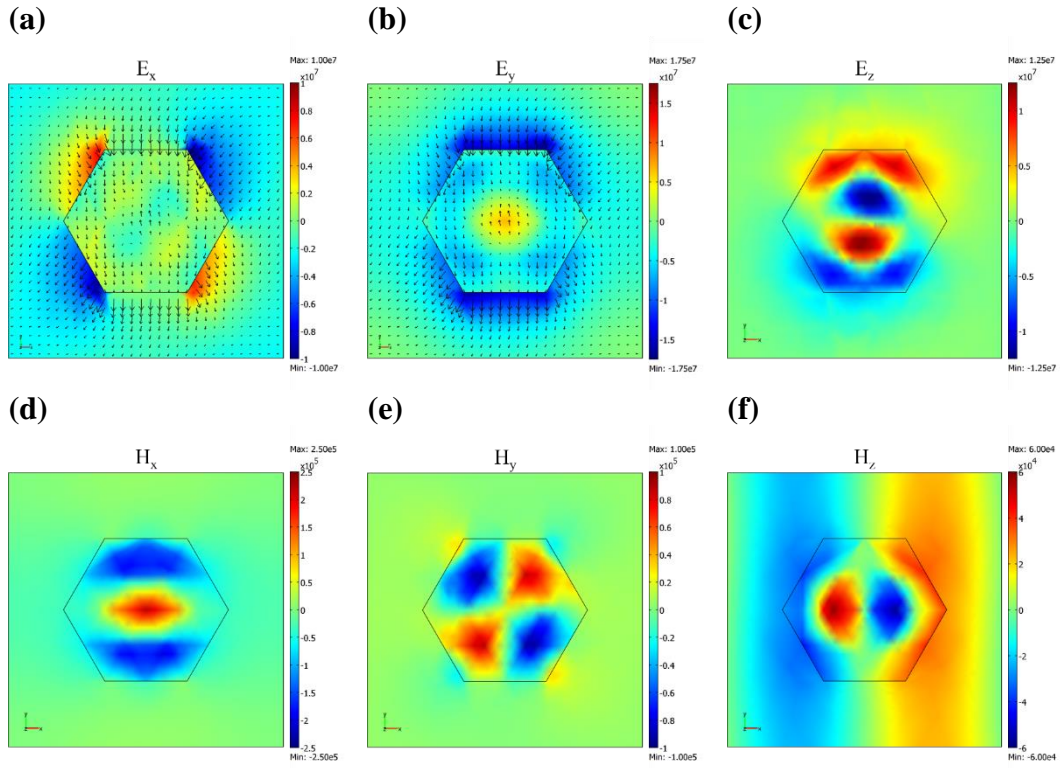
Figure 4.14. Field components (a) E_x, (b) E_y, (c) E_z, (d) H_x, (e) H_y, and (f) H_z at λ = 550 nm in InP nws of D = 300 nm and P = 500 nm. They correspond with the HE$_{12}$ mode. The E- and H-field component magnitudes are in units of V/m and A/m. Electric field vectors are shown in (a) and (b).
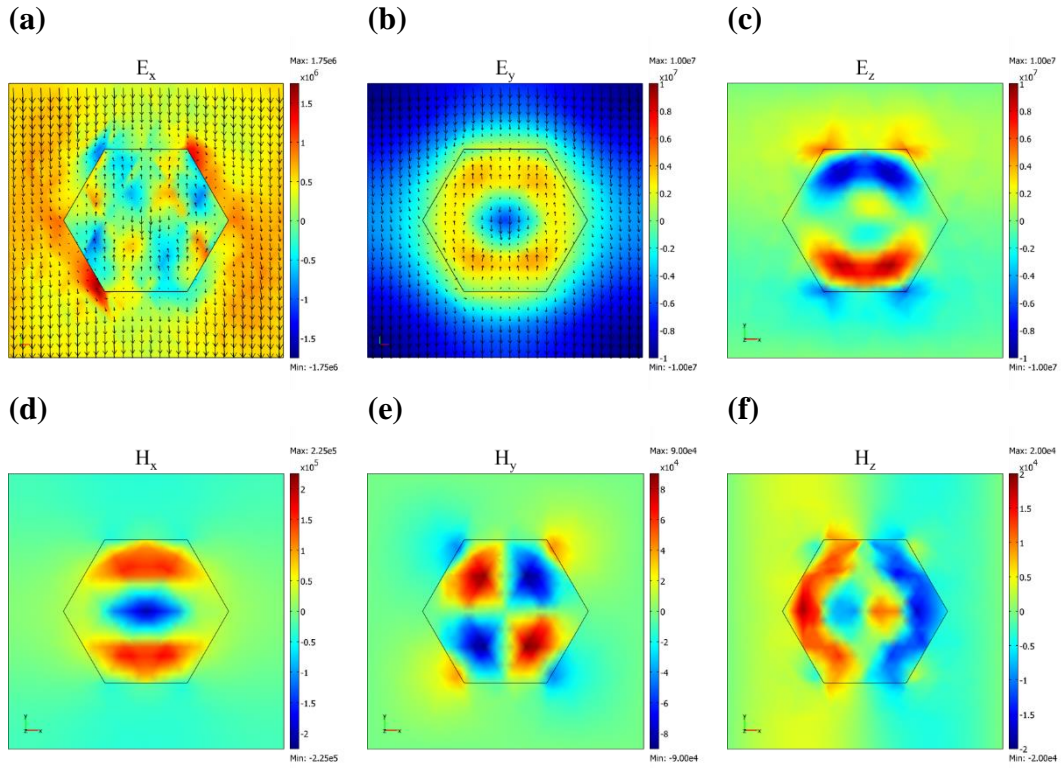
Figure 4.15. Field components (a) E_x, (b) E_y, (c) E_z, (d) H_x, (e) H_y, and (f) H_z at λ = 600 nm in InAs nws of D = 300 nm and P = 500 nm. They correspond with the HE$_{12}$ mode. The E- and H-field component magnitudes are in units of V/m and A/m. Electric field vectors are shown in (a) and (b).
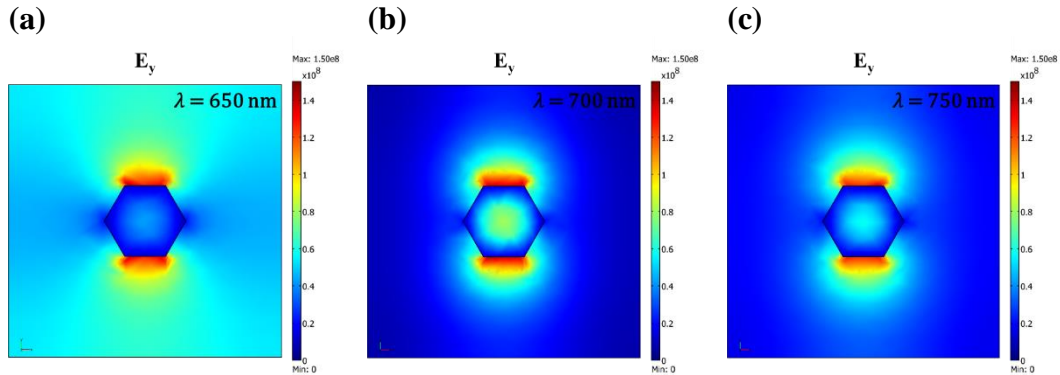
Figure 4.16. E_y field at (a) $\lambda = 650$ nm, (b) $\lambda = 700$ nm, and (c) $\lambda = 750$ nm in semi-infinite GaAs nws for D = 150 nm and P = 500 nm. The E_y field magnitude is in units of V/m.

Figure 4.16 shows the E_y field components on HE$_{11}$ resonance ($\lambda = 700$ nm) and 50 nm above or below resonance for GaAs nws for D = 150 nm and P = 500 nm. It is observed that on resonance the E_y field is localized within the nw along with a substantial evanescent field component along the incident light polarization direction (Y). It is the significant presence of the radial mode E_y field that leads to strong coupling with the incident light. This corroborates with observations from Si nw simulations [31,84]. For wavelengths 50 nm above or below the resonance wavelength, the light confinement in the nw is significantly diminished as is observed from the reduced E_y field magnitude in the nw, although a significant evanescent field is still observed. As a result, the coupling of incident light to the radial mode is weakened.
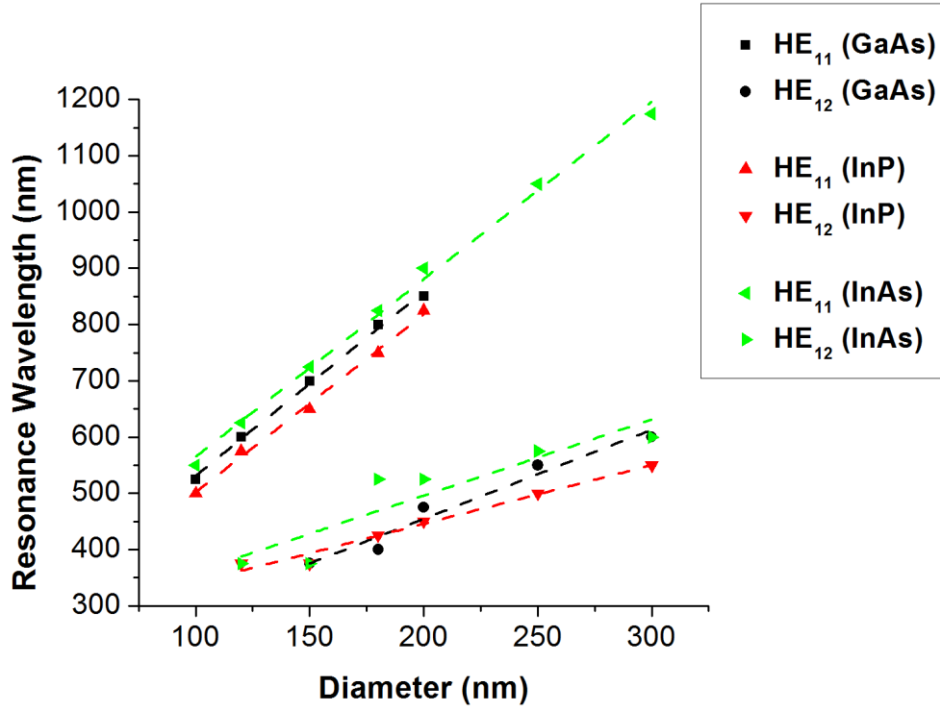
Figure 4.17. HE_{11} and HE_{12} resonance wavelength versus D for GaAs, InP, and InAs semi-infinite nws with P = 500 nm. The dashed lines are linear fits of the data.

The HE_{11} and HE_{12} resonance wavelengths, for all three materials, are plotted with respect to D in figure 4.17 for semi-infinite nws with P = 500 nm. The resonance linearly red-shifts with increasing D for D/P << 1. This can be explained using nw radial boundary conditions by assuming that the HE_{1n} radial mode evanescent field is negligible and it has a sine profile in the nw. Then the resonance red-shift with D can be roughly approximated using the following relationship:

$$\lambda_{HE1n} = \frac{Re(\bar{n}_{eff})D}{n} \qquad (4.1)$$

where n is the radial mode index (counts the number of half wavelengths or field nulls along the radius) and $Re(\bar{n}_{eff})$ is the real part of the complex effective refractive index $(\bar{n}_{eff})$ of the mode. A detailed derivation of equation (4.1) is provided in section 2.7.4. As observed from equation (4.1), each HE_{1n} (n = 1, 2, etc.) radial mode resonance wavelength linear trend with D will have different slopes (nm red-shift per nm increase in D), which is confirmed in figure 4.17. A slightly modified expression for determining the approximate HE_{11} resonance wavelength versus D is provided by Anttu et al. [80,85]. The resonance red-shift as D/P approaches 1 will be explored in the next chapter in the context of InSb whose absorptance spectra spans well into the mid wavelength infrared (MWIR) region.

The red-shift of the resonance wavelength with D is tabulated in table 4.1 for the HE_{11} and HE_{12} modes with similar results obtained for all three materials. This is expected since the complex refractive indices $(\bar{n}(\lambda))$ of all three materials follow similar trends, as shown in figure 3.3. The red-shift of the HE_{11} and HE_{12} modes was similar to that observed for the finite nws in figures 4.1 to 4.3. Table 4.1 also provides the maximum D at which HE_{11} and HE_{12} resonance wavelengths reach the respective material bandgap.

Table 4.1. D dependences of HE_{11} and HE_{12} modes for semi-infinite nws with P = 500 nm

Material	HE_{11} red-shift	Maximum HE_{11} D (nm)	HE_{12} red-shift	Maximum HE_{12} D (nm)
GaAs	3.27	204	1.58	463
InP	3.16	233	1.04	657
InAs	3.15	1031	1.35	2422

4.3 Length (L) dependence of nw absorptance

The absorptance of the semi-infinite nws was obtained for L = 300 nm to 2000 nm from the nw tip for D = 150 nm and P = 500 nm in GaAs, InP, and InAs nws, as shown in figure 4.18. Thin film absorptances for the same thickness as L are also shown for comparison with the nws. The HE_{11} resonance occurred at a wavelength of 700 nm, 650 nm, and 725 nm for GaAs, InP, and InAs nws, respectively. The HE_{11} absorptance spectra for all three materials increases similarly with L. As L increased, the HE_{11} peak absorptance increased and broadened due to bulk absorption. The negligible peak shift with L indicates further that the resonance peak is only due to radial modes [33]. The HE_{11} peak absorptance exceeded 0.9 for L = 750 nm for both GaAs and InP nws, while InAs nws required L = 1000 nm.

(a)

(b)

(c)
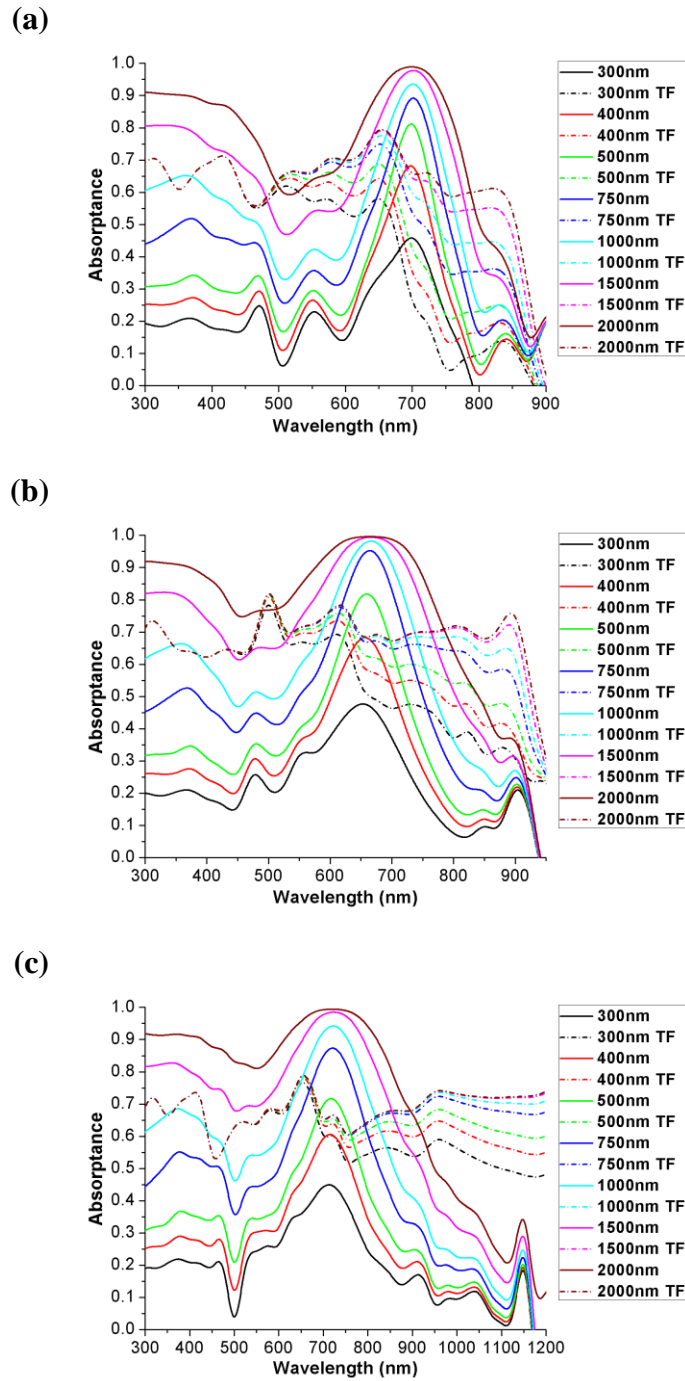
Figure 4.18. The absorptance of (a) GaAs, (b) InP, and (c) InAs nws for different L along the semi-infinite nw axis. L was measured from the nw tip. Thin film (TF) absorptances for the same thickness are also plotted for comparison with the nws.

A broader HE_{12} resonance peak was observed at a wavelength of 375 nm for all three materials, which increased in absorptance with increasing L. The HE_{12} peak absorptance was weaker compared to the HE_{11} resonance peak, as was observed earlier from the energy density profiles in figure 4.6 for finite nws. As mentioned previously, this low absorptance is attributed to the weaker coupling of the incident light to the HE_{12} radial mode. However, when the HE_{11} resonance peak moved into the bandgap with increasing D, then the HE_{12} peak absorptance became relatively stronger (see figure 4.9).

4.4 Effect of near-field coupling on nw absorptance

To assess the effect of evanescent wave near-field coupling in GaAs, InP, and InAs nws, the absorptance in semi-infinite nws were compared for P = 250 nm to 500 nm for D = 150 nm. The absorptance was simulated for L = 500 nm from the nw tip. The thin film absorptance for the same thickness was also simulated for comparison with the nws. As shown in figure 4.19 for GaAs, InP, and InAs nws, a blue-shift in the HE_{11} resonance peak was observed with decreasing P (increasing nw array density).

(a)

(b)

(c)
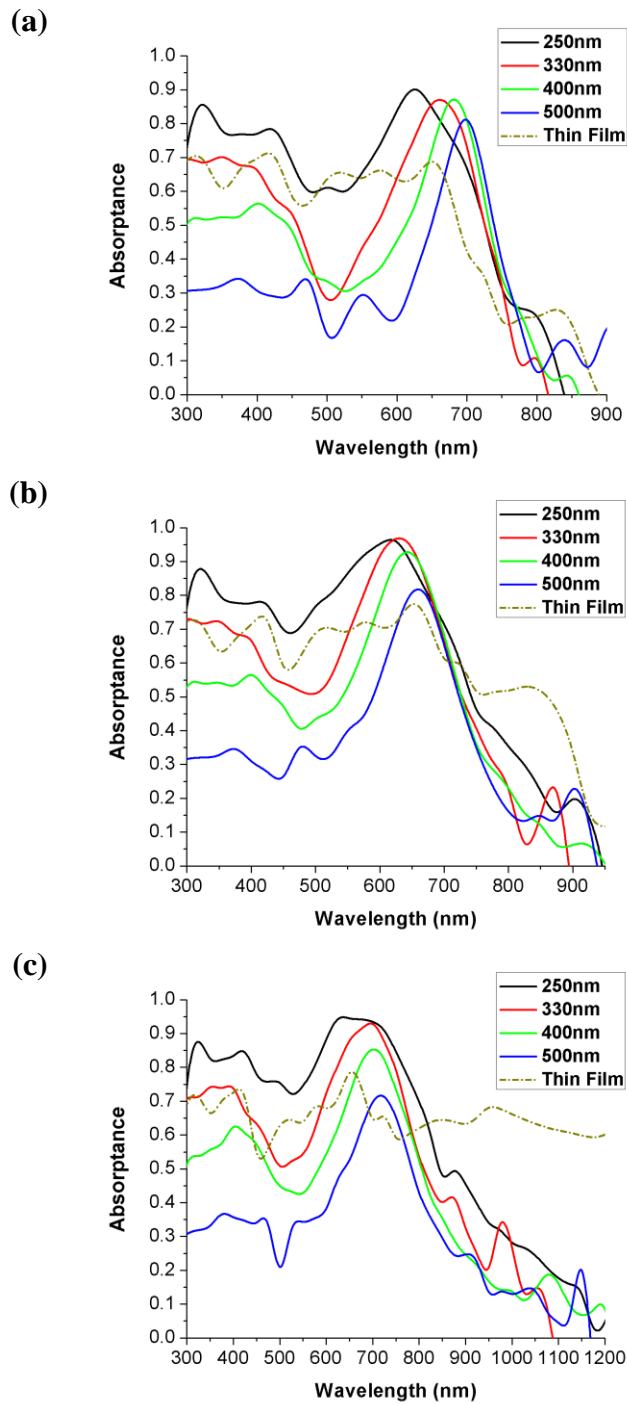
Figure 4.19. Absorptance at L = 500 nm and D = 150 nm for semi-infinite (a) GaAs, (b) InP, and (c) InAs nws for P = 250 nm, 330 nm, 400 nm, and 500 nm. Absorptance from a thin film of equivalent thickness is also indicated.

This shift in peak resonance is related to the increase in near-field evanescent wave coupling with neighbouring nws as P decreases. Concurrently, the resonance peak absorptance also increased with decreasing P. This increase in absorptance is associated with the increase in nw D/P, as discussed previously for figure 4.4. However, as the array becomes even denser, the absorptance peak reaches a maximum and then decreases at the thin film limit, D/P ~ 1 (e.g. InP in figure 4.19 (b); alternatively see figure 4.4). The blue-shift of the resonance peak with decreasing P stems from the destructive interference of the evanescent fields leading to a localized decrease in the refractive index of the medium surrounding the nw [20]. This leads to an increased confinement of the radial modes to the nw core [20]. As a result, with increasing nw array density the radial modes of individual nws transition to the photonic modes of a 2D photonic crystal due to increasing near field coupling between nws [20,53]. A more elaborate discussion has been provided in section 2.8.

4.5 Contribution of Fabry-Perot (F-P) modes to nw absorptance

The contribution of the F-P modes to nw absorptance on resonance was discerned by comparing the absorptance in finite (with same material substrate) and semi-infinite nws while keeping all other parameters constant. For this purpose, D = 150 nm and P = 500 nm was used for both finite and semi-infinite nws. The absorptance at L = 500 and 1000 nm in semi-infinite nws were compared with that of finite nws having the same L.

As shown in figure 4.20 for GaAs, InP, and InAs nws, the HE_{11} resonance peaks for finite and semi-infinite nws closely overlap. This is due to strong attenuation of light, coupled strongly to the HE_{11} radial mode on resonance, near the top of the nws as observed from the energy density profiles in figure 4.5. Hence, multiple longitudinal reflections along the nw axis due to the F-P modes have little effect on the HE_{11} resonance absorption.
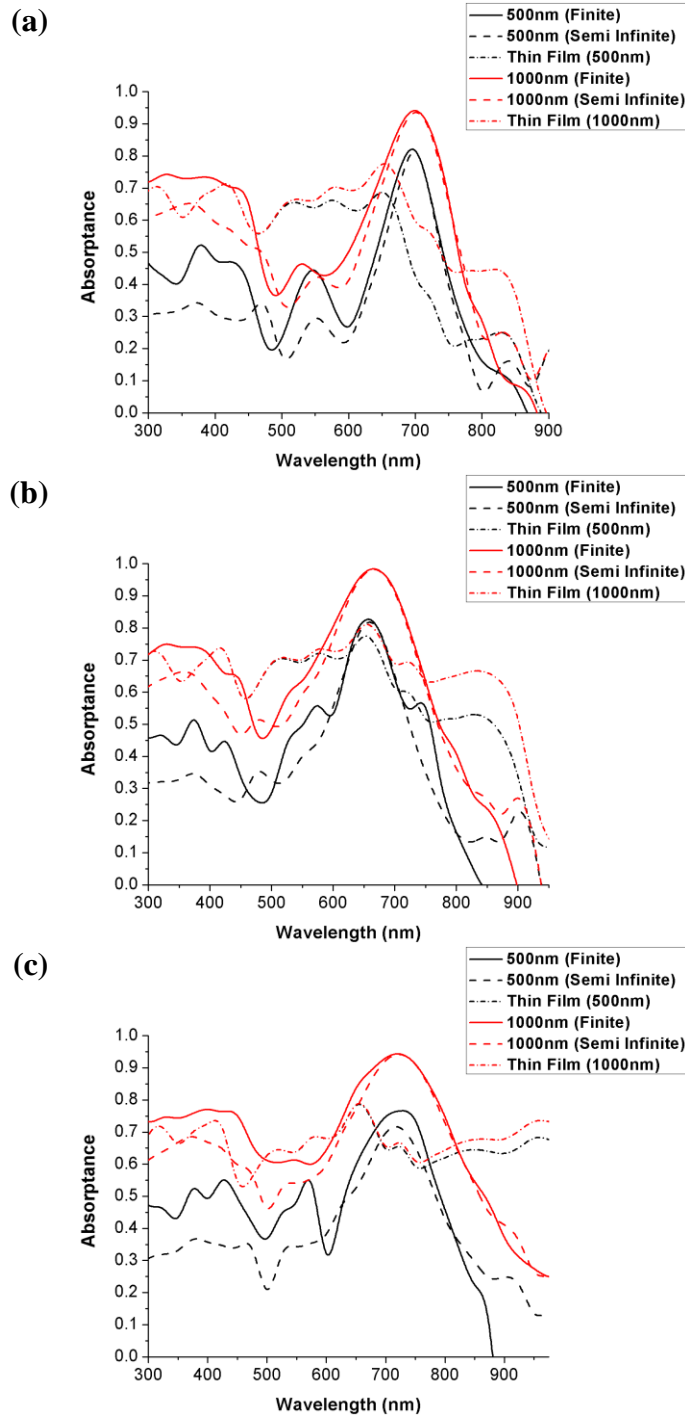
Figure 4.20. Absorptance in finite and semi-infinite (a) GaAs, (b) InP, and (c) InAs nws for D = 150 nm and P = 500 nm at L = 500 nm and 1000 nm. Absorptances from thin film of equivalent thickness are also indicated.

There was a significant difference between the finite and semi-infinite HE_{12} resonance peaks for the selected array parameters for all three materials. This difference resulted from the weak coupling of light to and attenuation of the HE_{12} radial mode in the nw, as was evident from the axial energy density profile in figure 4.6. The multiple reflections due to the F-P modes in finite nws considerably enhance the HE_{12} resonance absorption. However, with increasing L, the absorption enhancement due to the F-P modes is diminished due to greater attenuation of the HE_{12} mode along the nw axis. As well, for larger diameters the F-P mode effect on HE_{12} resonance diminishes due to strong attenuation along the nw axis, as is observed in figure 4.8. Additionally, as the HE_{1n} modes move into the bandgap of the nws, the effect of the F-P modes become significant due to negligible attenuation of the radial modes along the nw axis.

4.6 Comparison between hexagonal and circular cross-section nw array absorptance

In order to make the above mentioned results relevant for circular cross-section nws, which are the common nw cross-section type for top down etching method, simulation of hexagonal and circular cross-section nws were performed for the same geometrical parameters. Figure 4.21 shows the nw absorptance curves for D = 95 nm, P = 400 nm, and L = 1000 nm on GaAs substrate. The HE_{11} resonance

peak for a circular cross-section nw is red-shifted by ~25 nm compared to the

hexagonal cross-section nw for the above simulated array parameters.
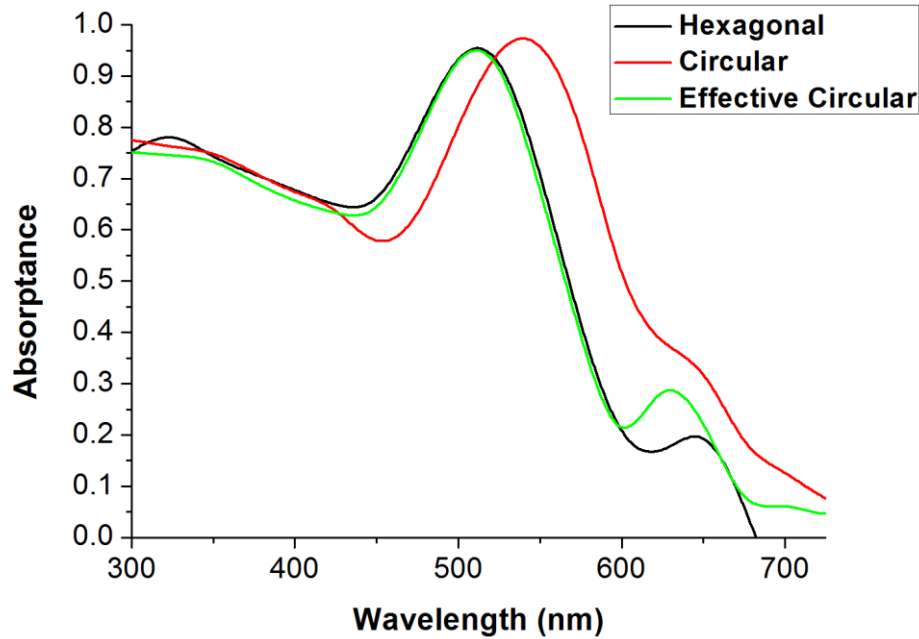
Figure 4.21. GaAs nw array absorptance for D = 95 nm (Hexagonal cross-section; black), D = 95 nm (Circular cross-section; red), and D = 86.4 nm (Circular cross-section with the same area as hexagonal cross-section with D = 95 nm, green). Incident light, parallel to the nw axis, was Y-polarized. Similar results are also observed for X-polarized incident light.

This resonance red-shift is not due to the shape of the nw cross-sections but

due to the change in the cross-sectional area between the two nws. The $\bar{n}_{eff}$ of the

HE$_{1n}$ radial modes depend only on the cross-sectional area of hexagonal and

circular cross-section nws [44,45,86]. As a result, the absorptance peaks can be

aligned by using the following D conversion factor from hexagonal to circular

cross-section nws for the same cross-sectional area:

$$D_{circ} = \sqrt{\frac{3\sqrt{3}}{2\pi}} D_{hex} \approx 0.91(D_{hex}) \tag{4.2}$$

where D_{circ} is the diameter of the "effective" circular cross-section with the same area as the hexagonal cross-section with diameter D_{hex}. From equation (4.2), $D_{circ} =$ 86.4 nm for $D_{hex} = 95$ nm. As observed from figure 4.21, the absorptance spectra for both "effective" circular and hexagonal cross-section nws strongly overlap. However, the field profiles of the HE_{1n}^x and HE_{1n}^y radial modes (superscript x and y represent polarization direction) slightly differ in hexagonal cross-section nws compared to circular cross-section nws, where they are degenerate [45]. This dissimilarity is due to the reduction in symmetry from circular (which is rotationally invariant) to hexagonal cross-section (which has six fold rotational symmetry) [45].

As a result, all the observations from this chapter equally apply for both circular and hexagonal cross-section nws. In the next chapter InSb nw array absorptance will be examined for wavelengths spanning near infrared (NIR), short wavelength infrared (SWIR), and MWIR regimes with special focus on optimizing the nw geometrical parameters for achieving sharp resonance peaks up to the InSb bandgap. This will take us one step closer to realizing efficient nw multispectral detectors in the MWIR region.

5 Optimizing InSb nanowire (nw) array geometrical parameters for high resonance absorptance

In chapter 4 we demonstrated that GaAs, InP, and InAs nanowires (nws) support optical resonance modes, making them very effective waveguides that can concentrate and absorb light [18]. Similar phenomena were also reported from optical modeling and experimental measurements on semiconductor nws [27,30,39,40,42,54,87–91]. Additionally, the individual contributions of radial mode resonance, near-field evanescent wave coupling, and longitudinal or Fabry-Perot (F-P) mode resonance on nanowire (nw) array absorptance were investigated. In the present chapter, we continue our investigation of the influence of geometrical parameters linked to these optical phenomena on InSb nw HE_{1n} resonances in the infrared (IR) region. The results presented in this chapter were previously published in Nanotechnology, titled: "Optical design of a mid-wavelength infrared InSb nanowire photodetector" [19].

Since the aforementioned optical phenomena arise from the geometrical structure of the nw, their effects on InSb nw array absorptance are similar to those observed for GaAs, InP, and InAs nw arrays. However, since the investigated simulation wavelengths in InSb nws extend well into the mid-wavelength infrared (MWIR) region, the trends in the variation of diameter (D), period (P), and length

(L) are more prominent. Additionally, the InSb complex refractive index ($\bar{n}(\lambda)$) dispersion is different compared to other III-V materials (see figure 3.3 and 3.4), especially that of the extinction coefficient, $k(\lambda)$. Thus, a simple interpolation function cannot be used to predict InSb nw array optical responses (e.g. absorptance) from those of other III-V nw arrays, e.g. GaAs, InP, etc. by rescaling their geometrical parameters [80]. Rather, a systematic optical simulation study of InSb nw array is necessary in order to investigate its optical responses [80]. InSb nw array simulations are performed for a square lattice with circular cross-section nws, as shown in figure 5.1.
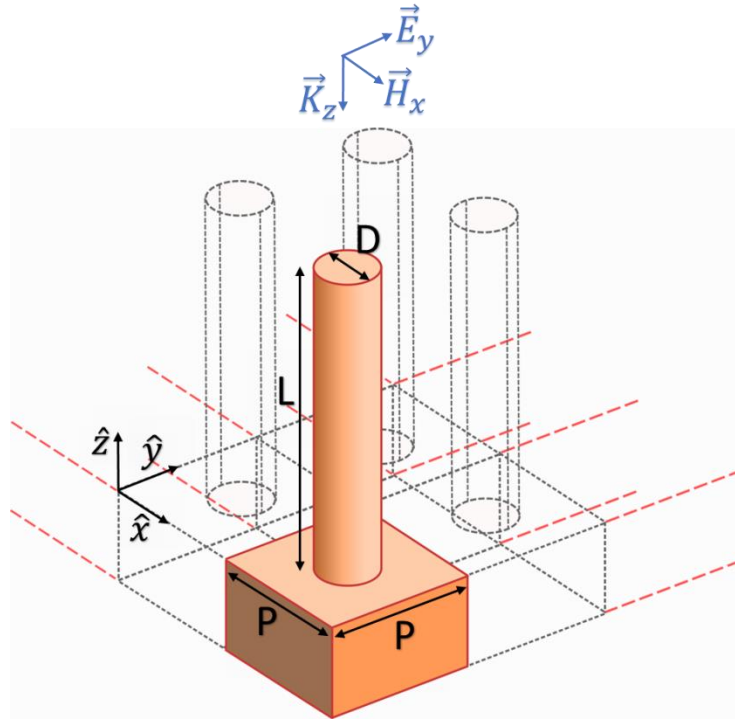
Figure 5.1. Schematic of a continuous 2D nw array with specified nw diameter (D), period (P), and length (L).

The absorptance results for circular cross-section nws equally apply to hexagonal cross-section nws via a simple D conversion formula (see equation (4.2) in section 4.6). Nw geometrical parameter space optimization for broadband absorption has been reported by various groups for solar cell application with square and hexagonal lattice configurations [36,49,51,53,92–94]. For such optimization schemes, the arrays are dense in order to broaden the resonance peak absorptance through strong near-field coupling between nws. In this chapter nw array geometrical parameters are optimized to produce sharp HE_{11} resonance peaks with narrow full-width-at-half-maximum (FWHM). These peaks are suitable for multispectral IR detection as they allow for several narrow spectral photodetection bands in the IR spectrum.

5.1 Effect of geometrical parameters on InSb nw resonance

The simulated InSb nw array absorptance spectra are shown in figure 5.2, where P = 1500 nm, L = 1500 nm and D = 200 nm to 1200 nm. The simulated nws are semi-infinite. The medium between and above the nws is set as air for all simulations investigated in section 5.1.

(a)

(b)
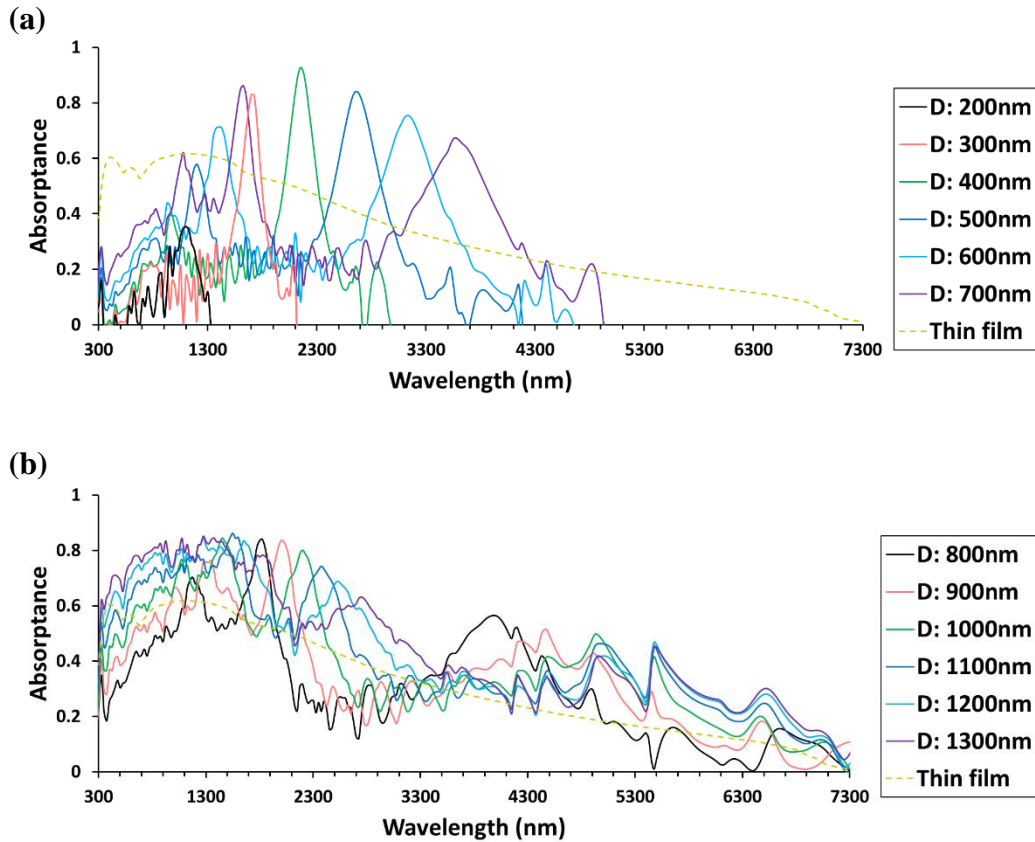
Figure 5.2. Absorptance spectra of semi-infinite InSb nw arrays with P = 1500 nm, L = 1500 nm and D from (a) 200 nm to 700 nm, and (b) 800 nm to 1300 nm. Absorptance from a thin film of 1500 nm thickness is shown for comparison.

The absorptance of an InSb thin film with the same thickness as L (1500 nm) is also included for comparison in figure 5.2. The nws exhibit strong optical absorptance, which exceeds the thin film absorptance, at certain resonance wavelengths. These pronounced absorptance peaks are due to the HE_{1n} family of radial mode resonances [18]. This is confirmed by the profiles of the electric (E-) and H-field components in figures 5.3 to 5.5, which are characteristic of the HE_{1n} modes.

(a)

(b)

(c)

(d)

(e)

(f)
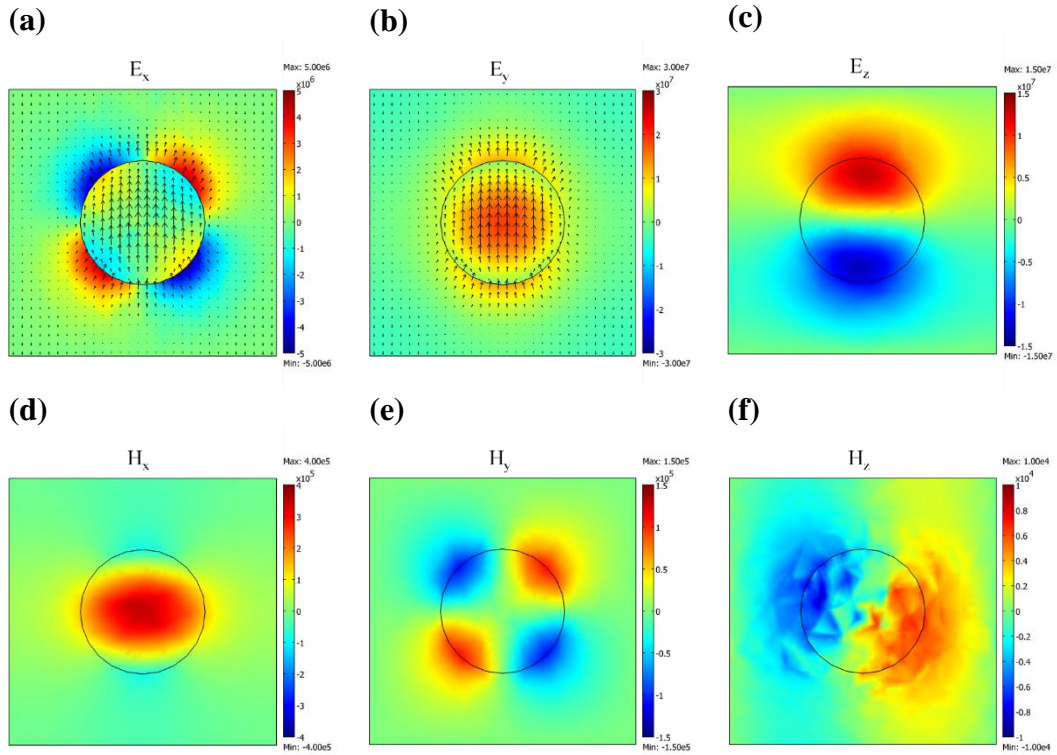
Figure 5.3. (a) E_x, (b) E_y, (c) E_z, (d) H_x, (e) H_y, and (f) H_z field components in InSb nw array at $\lambda = 3550$ nm for P = 1500 nm and D = 700 nm. The field patterns correspond to the HE_{11} mode. The E- and H-field component magnitudes are in units of V/m and A/m.
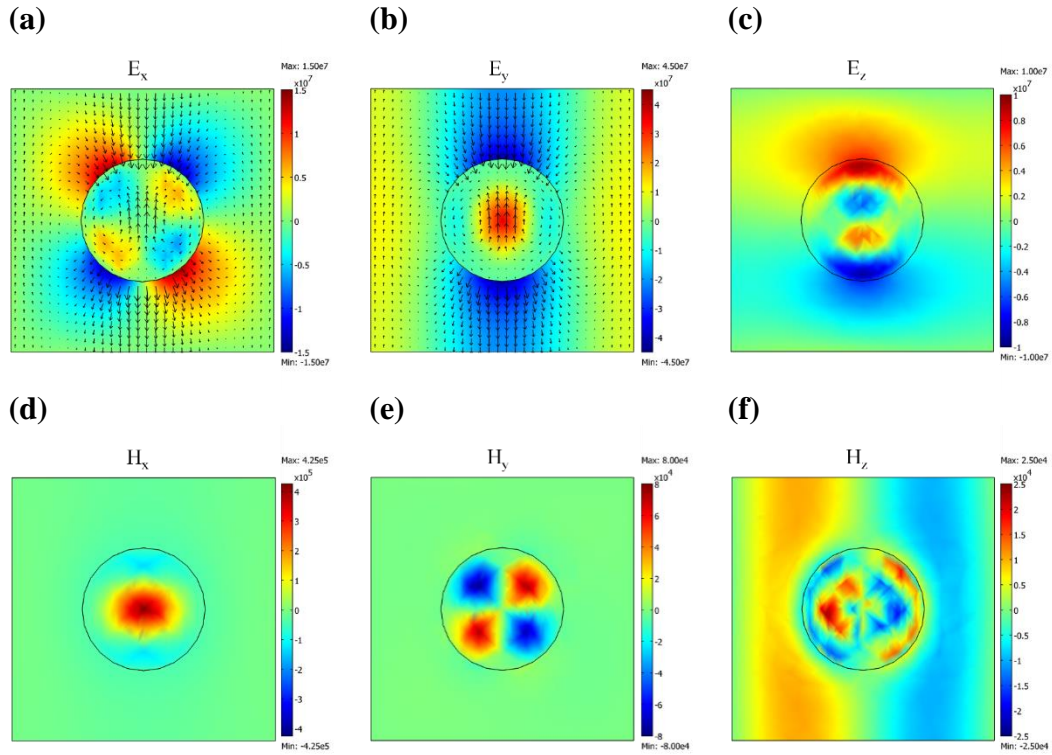
Figure 5.4. (a) E_x, (b) E_y, (c) E_z, (d) H_x, (e) H_y, and (f) H_z field components in InSb nw array at $\lambda = 1625$ nm for P = 1500 nm and D = 700 nm. The field patterns correspond to the HE_{12} mode. The E- and H-field component magnitudes are in units of V/m and A/m.

(a) **(b)** **(c)**

(d) **(e)** **(f)**
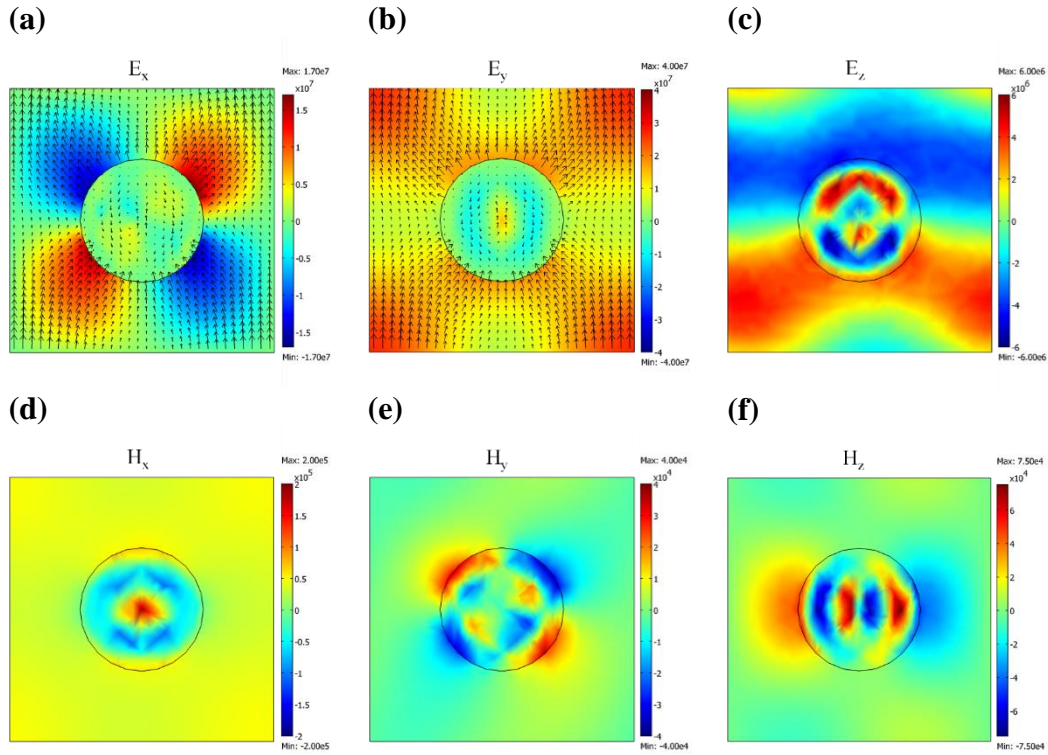
Figure 5.5. (a) E_x, (b) E_y, (c) E_z, (d) H_x, (e) H_y, and (f) H_z field components in InSb nw array at $\lambda = 1075$ nm for P = 1500 nm and D = 700 nm. The field patterns correspond to the HE_{13} mode. The E- and H-field component magnitudes are in units of V/m and A/m.

The resonance peak wavelength versus D for each of the HE_{1n} radial modes for L = 2000 nm and P = 500 nm to 2000 nm are presented in figure 5.6. The HE_{1n} resonance peaks strongly depend on D and red-shift with increasing D at fixed P. This general property is also reported for nws of other III-V materials and can be explained by the radial boundary conditions of the nw (see equation 2.128 in section 2.7.4). The HE_{1n} resonance peaks also weakly depend on P and blue-shift with decreasing P at fixed D. This is due to an increase in near-field coupling between neighbouring nws. The increased coupling between neighbouring nws leads to

destructive interference of the evanescent fields at the nw surface [54]. This

effectively causes a localized decrease in the refractive index surrounding the nw

interface which increases mode confinement [54]. The overall effect results in the

HE_{1n} resonance wavelength blue-shift [54]. This phenomenon is elaborated in more

detail in section 2.8. The capability of tuning the resonance wavelengths with D and

P enables the fabrication of wavelength-tunable photodetectors for multispectral

imaging [55–57].
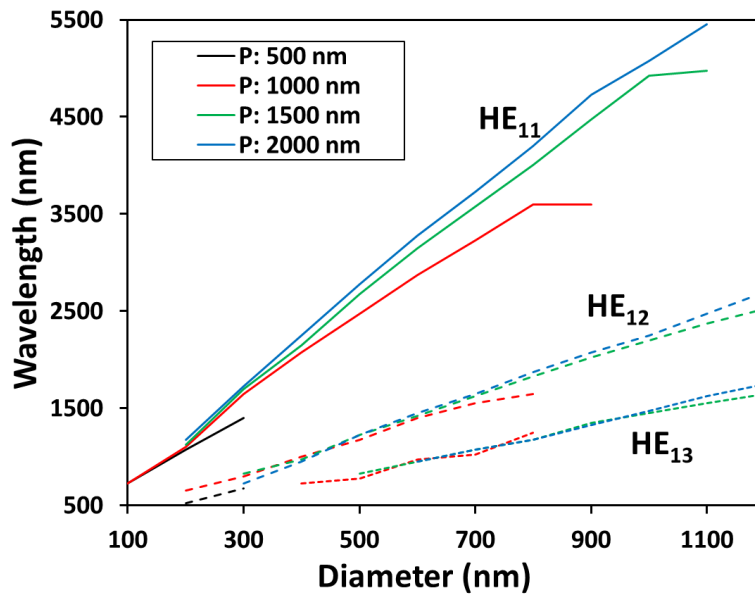
Figure 5.6. Resonance peak wavelengths versus D for HE_{11} (solid lines), HE_{12} (dashed lines), and HE_{13} (dotted lines) radial modes in semi-infinite InSb nw arrays, measured for L = 2000 nm and P = 500 nm to 2000 nm.

Contour plots of absorptance for L = 2000 nm and P = 500 nm to 2000 nm

are shown in figure 5.7, where the influence of P on the HE_{1n} resonances can be

observed. All of the HE_{1n} resonances follow the same general trend. The resonance

peak absorptance is small for D/P << 1 (sparse nw arrays), as most of the incident light passes between the nws without being absorbed. As D/P increases, less light is transmitted through nw array and the resonance peak absorptance increases until it reaches a maximum and thereafter decreases. As explained earlier, increasing D/P (denser nw arrays) leads to an increase in near-field coupling between neighbouring nws. This leads to greater mode confinement inside the nw which will increase the absorption of light coupled into the nw. However, the large refractive index difference, due to the localized drop in refractive index at the nw surface, will also increase reflection from the nw array [84]. With increasing D/P, the nw top surface area will also increase which will further increase reflectance from the nw top surface. Additionally, the extinction coefficient ($k(\lambda)$) also decreases as the resonance wavelength red-shifts to longer wavelengths with increasing D. The HE_{1n} resonance peak FWHM also broadens with increasing D for fixed P (increasing D/P), as evident in figure 5.2. This is due to increasing near-field coupling between adjacent nws [43].
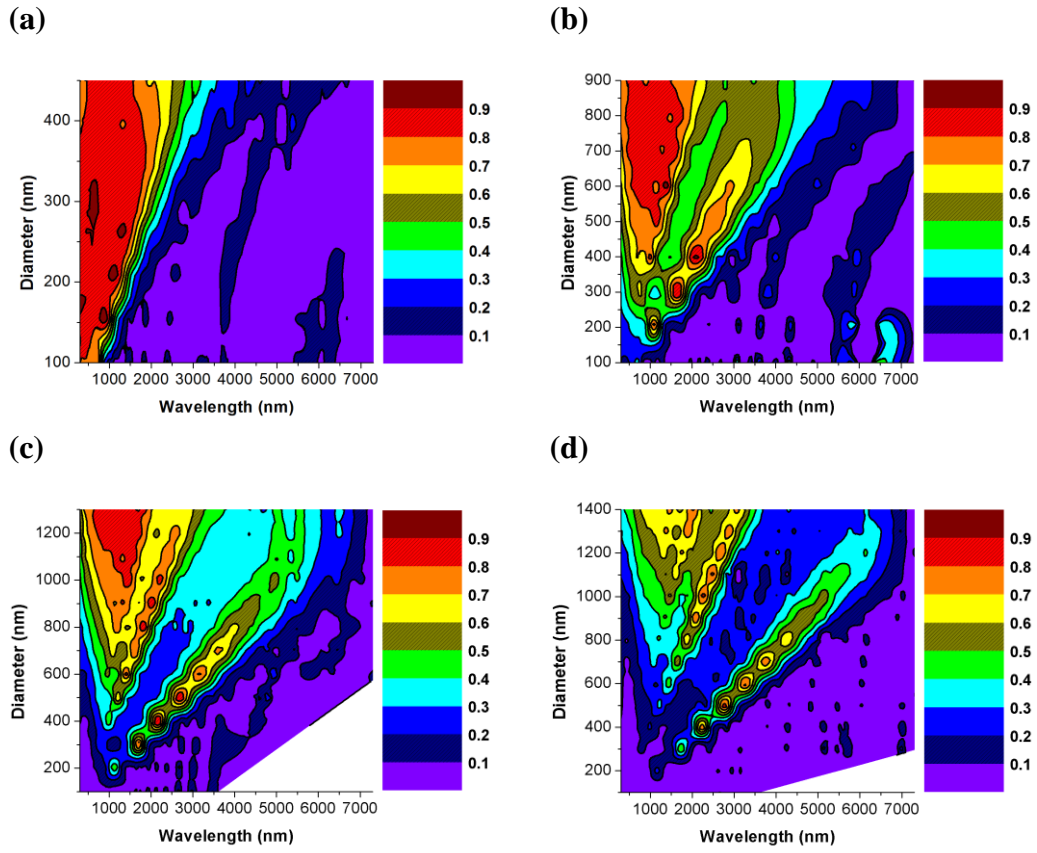
Figure 5.7. Contour plots of absorptance in semi-infinite InSb nw arrays for L = 2000 nm and P of (a) 500 nm, (b) 1000 nm, (c) 1500 nm, and (d) 2000 nm.

Contour plots of absorptance are presented in figure 5.8 for P = 1500 nm and L = 1000 nm to 10000 nm. The HE_{1n} peak absorptance rapidly increases and becomes more pronounced with increasing L until the absorptance peak saturates and broadens as L increases beyond 5000 nm. This was similarly observed for GaAs, InP, and InAs nws in section 4.3.

(a)   **(b)**

(c)   **(d)**
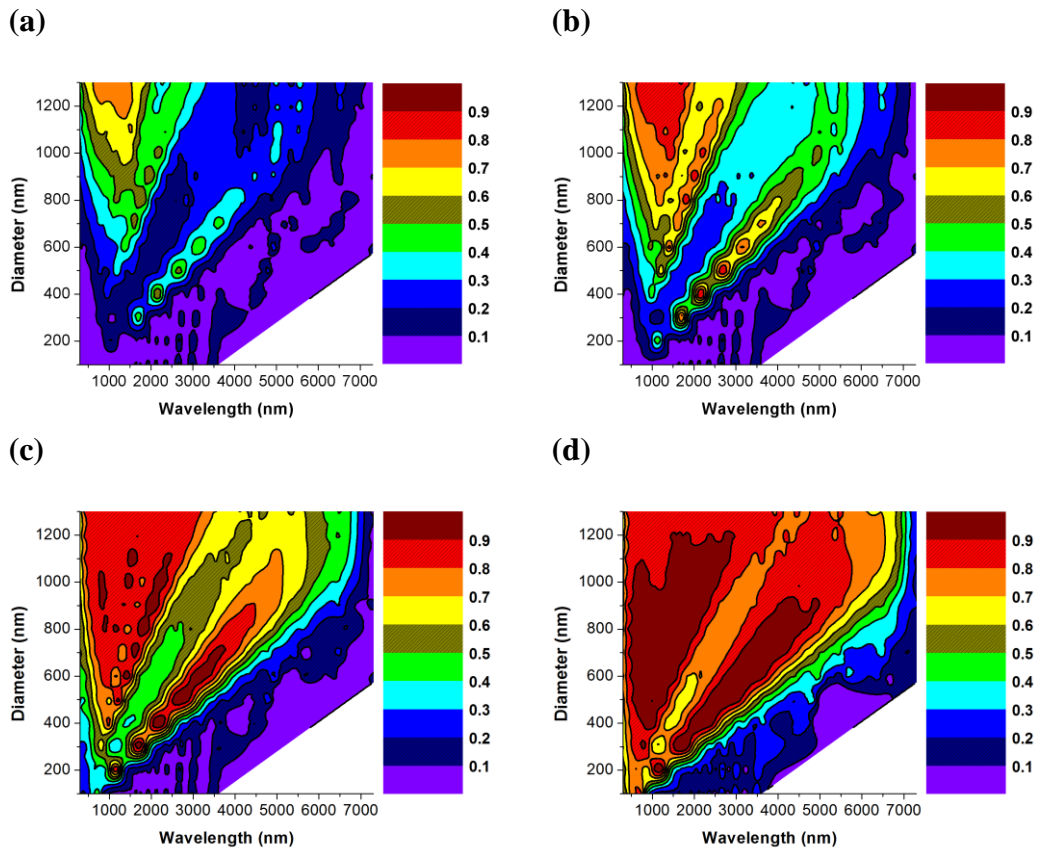
Figure 5.8. Contour plots of absorptance in semi-infinite InSb nw arrays at P = 1500 nm and L of (a) 1000 nm, (b) 2000 nm, (c) 5000 nm, and (d) 10000 nm.

5.2. Optimization of HE_{11} resonance absorptance

The array parameters (D, P, and L) for semi-infinite InSb nws in air were optimized to achieve high optical absorptance. Specifically, for a given D and P, the minimum L was determined to achieve an HE_{11} peak absorptance of ~0.8. These L values are plotted with respect to P for D = 200 nm to 1200 nm in figure 5.9.
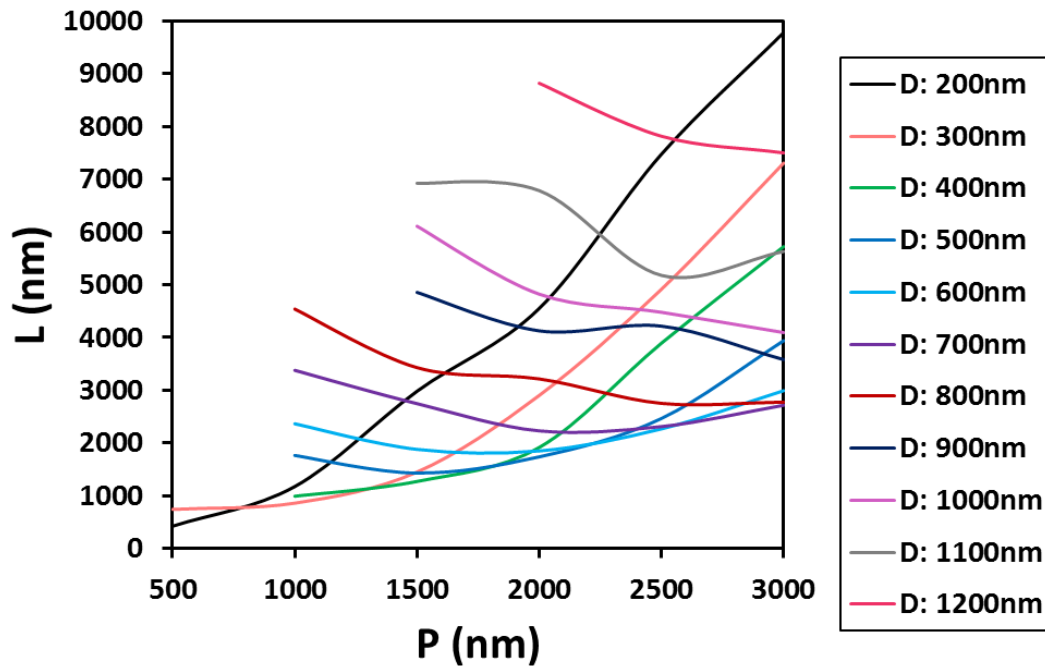
Figure 5.9. L versus P for semi-infinite InSb nw arrays with D = 200 nm to 1200 nm, giving an HE_{11} resonance peak absorptance of ~0.8.

The corresponding absorptance spectra for select D, P and L values closest to the lowest aspect ratio (L/D) are shown in figure 5.10. For D ≤ 900 nm (figure 5.10 (a)) the HE_{11} resonance peaks are clearly visible as compared to the resonance peaks from higher order HE_{1n} radial modes. The FWHM of these HE_{11} resonance

peaks were less than 1000 nm. For $D \geq 1000$ nm (figure 5.10 (b)), the resonance peaks are visible for HE_{11} between 5300-7300 nm, for HE_{12} between 2300-3300 nm, and for HE_{13} between 1300-2300 nm. As the HE_{11} peak red-shifts towards the bandgap (with increasing D), taller nws (larger L) are required to achieve high absorptance. The absorptance spectrum of a 10 µm thick InSb thin film is also included in figure 5.10 for comparison. It is evident that the nw absorptance at the HE_{11} resonance, for lengths less than 10 µm, are greater than that of the thin film absorptance.

(a)

(b)
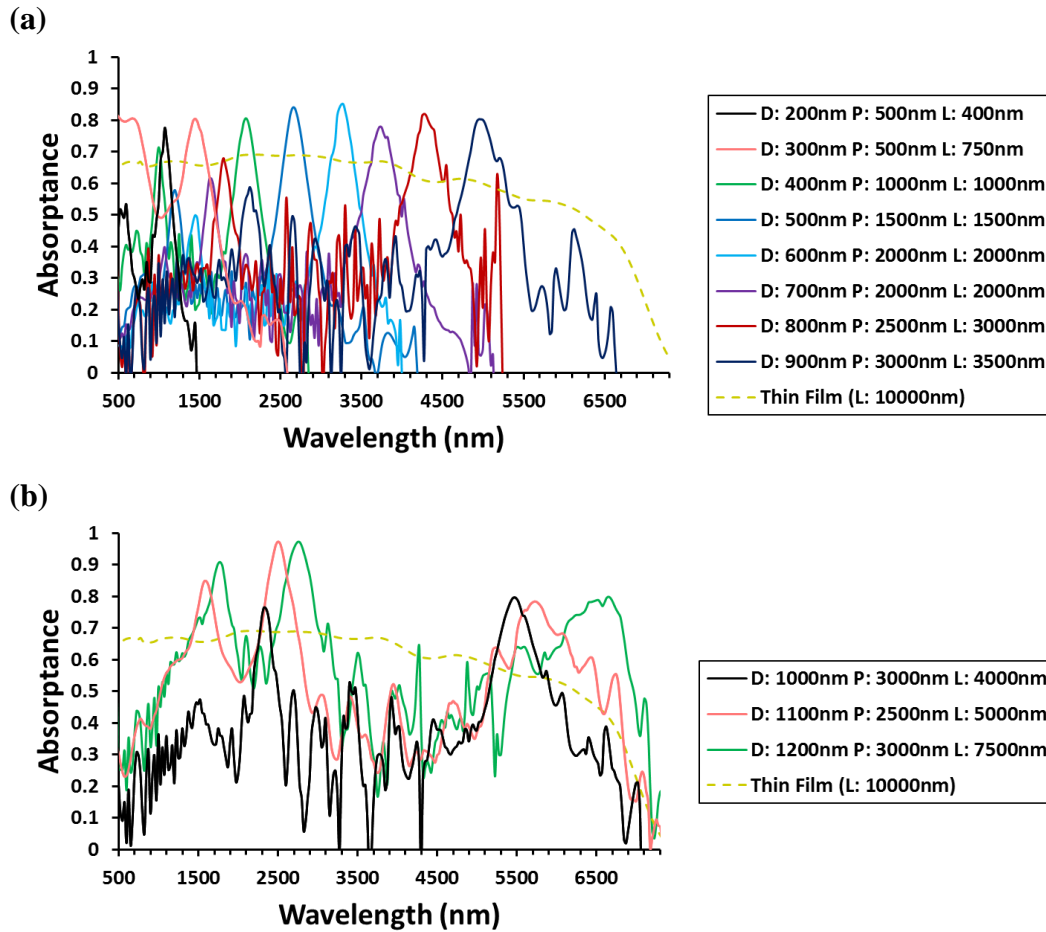
Figure 5.10. Absorptance spectra of InSb semi-infinite nw arrays with indicated D, P, and L values. Absorptance spectra from a thin film with thickness of 10000 nm is also shown for comparison.

The simulation results discussed thus far were obtained for particular lengths along semi-infinite nws. The perfectly matched layer (PML) substrate removed the possibility of back reflections from the substrate surface and, hence, F-P modes along the length of the nw. To include the effect of F-P modes on absorptance, the PML substrate was removed and the InSb nws were simulated on InSb or Si substrates. To demonstrate this, we select the HE_{11} absorptance spectrum

for D = 700 nm, P = 2000 nm, and L = 2000 nm (purple data series in figure 5.10

(a)). The HE_{11} resonance peak for this D, P, and L is ~3.7 µm. This resonance

wavelength is of particular interest as it falls within the 3-5 µm window of low

atmospheric IR absorption, allowing for a variety of MWIR related applications

[5,9].
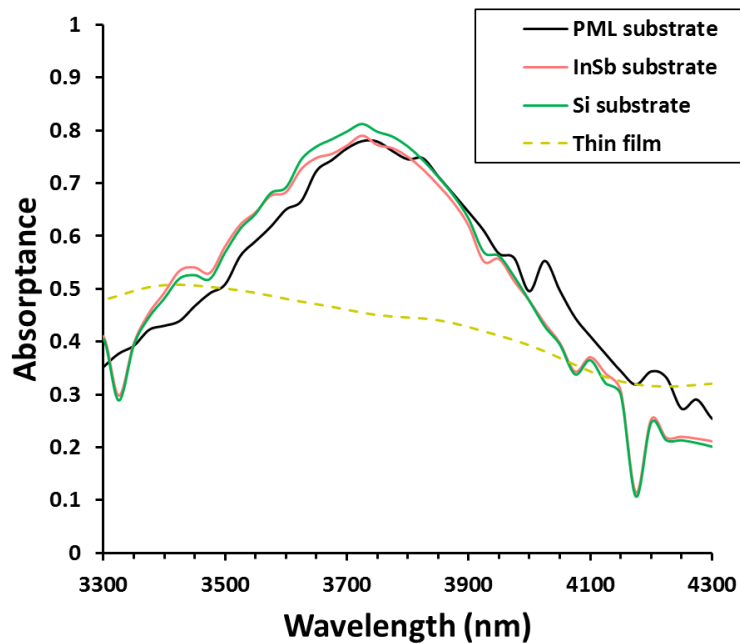
Figure 5.11. Absorptance spectra of InSb nw array with D = 700 nm, P = 2000 nm, and L = 2000 nm. As indicated in the legend, the substrate was either perfectly matched layer (PML), InSb or Si. The absorptance from an InSb thin film of 2000 nm thickness is included for comparison.

The HE_{11} resonance peaks for an InSb nw array with PML (black), InSb

(red), and Si (green) substrates are compared in figure 5.11. The absorptance near

the resonance peak was similar regardless of the substrate (PML, Si or InSb) due to

the strong optical absorptance in the nws and, hence, low transmittance to the

substrate. This leads to only negligible back reflections from the substrate (Si or InSb) and hence, minor oscillations in the absorptance spectra due to the F-P modes.

6 Optical design of a mid-wavelength infrared (MWIR) InSb nanowire (nw) photodetector

We have established from chapter 4 and 5 that nanowires (nws) support optical resonance modes. Their absorptance peaks can be tuned with diameter (D), period (P), and length (L). This naturally makes nanowire (nw) based multispectral photodetectors attractive because the nw geometry can be tuned to strongly absorb at a specified wavelength without the need for tuning the material bandgap or mounting additional spectral filters on top of the photodetector [9,56]. In this chapter we will present an optical design for a mid-wavelength infrared (MWIR) photodetector comprised of an InSb nanowire (nw) array on a Si substrate with ultrathin Ni top contact. Bisbenzocyclobutene (BCB) was used as the medium between nws as it is a common insulating filler medium in nw devices that provides support to the Ni top contact [52,76,95]. For the photodetector optical model, the nw array D, P, and L were optimized in BCB, similar to the geometrical optimization scheme developed in section 5.2. The chapter ends with a discussion on how light enters the nw photodetector on resonance. The results presented in section 6.1 of this chapter were previously published in Nanotechnology, titled: "Optical design of a mid-wavelength infrared InSb nanowire photodetector" [19].

6.1. Absorptance in an InSb nw MWIR photodetector

As mentioned in the chapter introduction, BCB is often used as a filling medium between nws to provide mechanical support for an electrical contact to the top of the nws. To assess how the HE_{11} resonance peak is affected by BCB, figure 6.1 shows the HE_{11} absorptance spectrum for InSb nws on Si substrate with BCB filler between the nws for parameters optimized for air (D = 700 nm, P = 2000 nm, and L = 2000 nm). These specific geometrical parameters were chosen since the HE_{11} resonance peak lies within the 3-5 µm low infrared (IR) atmospheric absorption window [96].
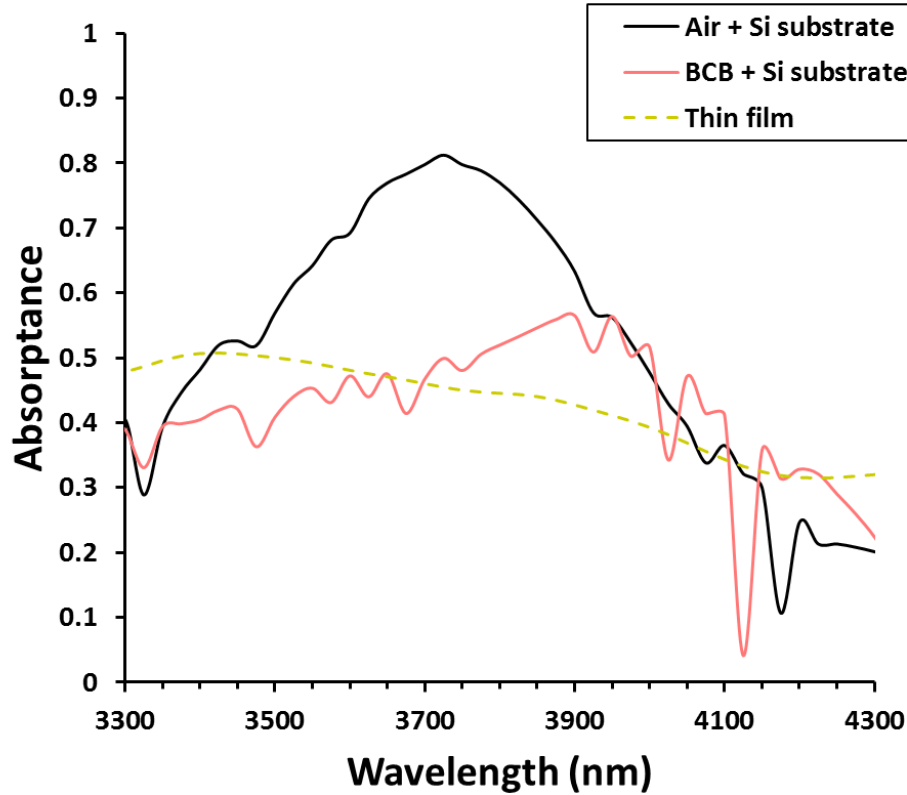
Figure 6.1. Absorptance spectra of InSb nw array with D = 700 nm, P = 2000 nm, and L = 2000 nm. As indicated in the legend, the medium between nws was either air or BCB, and the substrate was Si. The absorptance from an InSb thin film of 2000 nm thickness is included for comparison.

Compared to the case with air, the optical absorptance peak decreased substantially with BCB, and oscillations are introduced in the spectrum (figure 6.1). The decrease in optical absorptance is due to the reduced radial mode confinement due to higher refractive index ($n(\lambda)$) of BCB compared to air and, to a lesser extent, increased reflectance loss at the top of the nw array from the BCB/air interface. The former effect decreases the attenuation along the L leading to an increase in transmittance through the nw array to the substrate. The BCB therefore creates a

Fabry-Perot (F-P) cavity due to reflections between the BCB/air interface at the top and BCB/Si interface at the bottom of the nw array. This F-P cavity is responsible for the oscillations in the nw array absorptance spectrum with BCB.

The minimum L required for a HE_{11} peak absorptance of ~0.8 was investigated for nws with BCB filler. The L versus P data for D = 700 nm, analogous to figure 5.9, is presented in figure 6.2 for perfectly matched layer (PML) substrate and BCB filler (red).
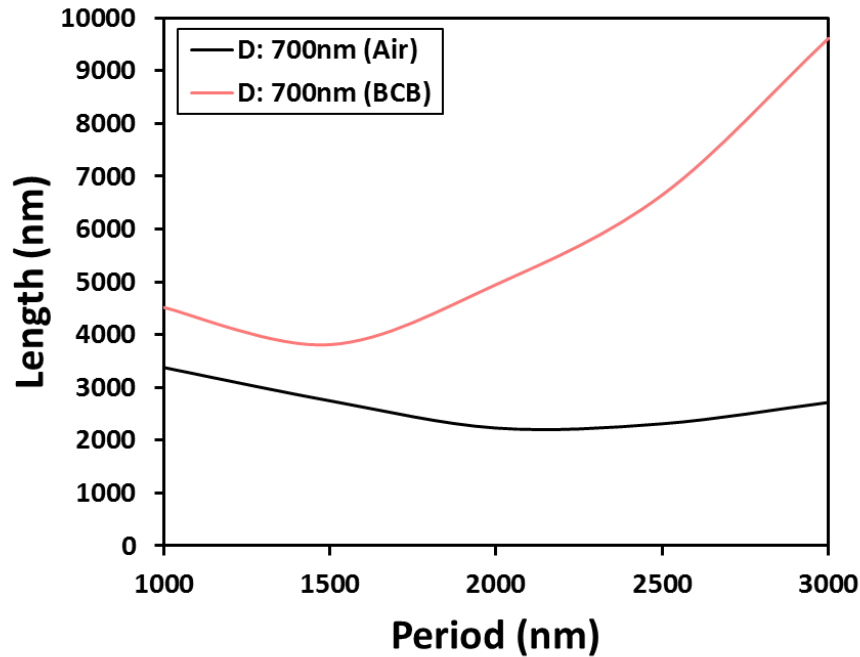
Figure 6.2. (a) L vs P curves for D = 700 nm for nw array in air (black) and BCB (red). The curves were constructed for HE_{11} resonance peak absorptance of ~0.8.

Due to the lower mode confinement for nws in BCB, larger L is required to recover a high optical absorptance. An HE_{11} peak absorptance of ~0.8 with

minimum aspect ratio (L/D) can be achieved with D = 700 nm, P = 1500 nm, and L = 4000 nm. The HE_{11} resonance spectrum for nw array in BCB for this D, P, and L on Si substrate is shown in figure 6.3 (black). A Si substrate was used due to its low absorptance in the MWIR and it provides future prospects for integration of III-V nw photodetectors with Si-based electronics [5,58]. But the lattice mismatch between InSb (lattice constant of 6.479 Å [97]) and Si (lattice constant of 5.431 Å [98]) is ~19.3%. This large lattice mismatch will put a limit on the critical diameter (D_c) beyond which grown InSb nws will have dislocation or they will not grow [99]. The suggested InSb D, in chapter 5 and this chapter, for sharp resonance absorptance in IR were on the scale of 100s of nm which are expected to be much greater than D_c for InSb. Hence lattice mismatch strain is expected for grown InSb nws on Si. However, lattice strain can be averted by defining a nw-substrate contact area that is much smaller than the eventual D. This can be achieved via selective-area epitaxy, which is the most common method for fabricating uniform nw arrays. In this method, patterned holes are defined on an oxide thin film on a Si substrate where the nws nucleate and grow [100]. Thus the contact area D between nw and Si can be defined such that it is much lower than D_c [99]. The desired D can then be grown in excess of D_c via overgrowth on the oxide thin film.
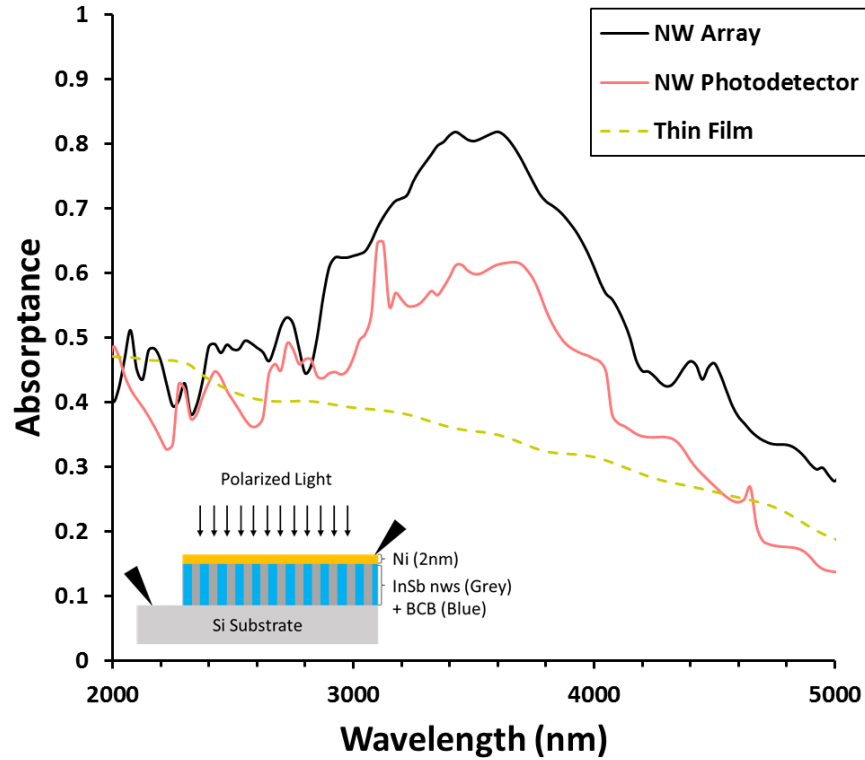
Figure 6.3. HE_{11} resonance absorptance spectra of InSb nw array with BCB, Si substrate, and a 2 nm thick Ni contact layer (red). The HE_{11} resonance absorptance without the 2 nm Ni contact is shown in black. The nw array parameters were D = 700 nm, P = 1500 nm, and L = 4000 nm. The optical absorptance from a 4000 nm InSb thin film with 2 nm Ni top contact is included for reference. The inset shows a schematic of the photodetector device with triangles representing electrical contacts.

A photodetector was simulated on a Si substrate with a 2 nm ultra-thin Ni contact layer at the nw top surface. The nw geometrical parameters were kept fixed at D = 700 nm, P = 1500 nm, and L = 4000 nm. Such an ultra-thin metal film can serve as a semi-transparent window for MWIR photodetectors due to its high optical transmittance (~0.8) in the MWIR and low resistivity (~200 $\mu\Omega$*cm) [101]. Figure 6.3 shows the HE_{11} absorptance spectrum of the photodetector (red). The

inset in figure 6.3 shows the photodetector schematic. The absorptance spectrum of an equivalent thickness InSb thin film (L = 4000 nm) with 2 nm ultra-thin Ni top contact is also presented for comparison. The HE_{11} resonance absorptance profile is still observable for the photodetector device even though the absorptance decreased relative to nws without Ni top contact. Even with the Ni contact, the absorptance of the nw photodetector near the HE_{11} resonance wavelength is still superior to that of the thin film. Additionally, if we assume that all the absorbed photons lead to electron-hole pairs that are collected, then the photodetector absorptance spectrum also indicates the external quantum efficiency (EQE) of the device.

Bulk Ni complex refractive index ($\bar{n}(\lambda)$) values were used in the photodetector simulation as an approximation to the ultra-thin Ni film $\bar{n}(\lambda)$. This is due to variability of $\bar{n}(\lambda)$ with thin film deposition method [102]. In addition, Dumont et al. [103] further showed that the $\bar{n}(\lambda)$ values for ultrathin Ni films of thickness < 10 nm drops compared to bulk values. This would result in a lower reflectance in Ni thin film compared to bulk Ni. Thus the simulation results presented here are a conservative estimate. Figure 6.4 shows the simulated transmittance (black), reflectance (red), and absorptance (green) curves for the 2 nm Ni thin film on top of the nw-BCB layer for the above simulated photodector device.
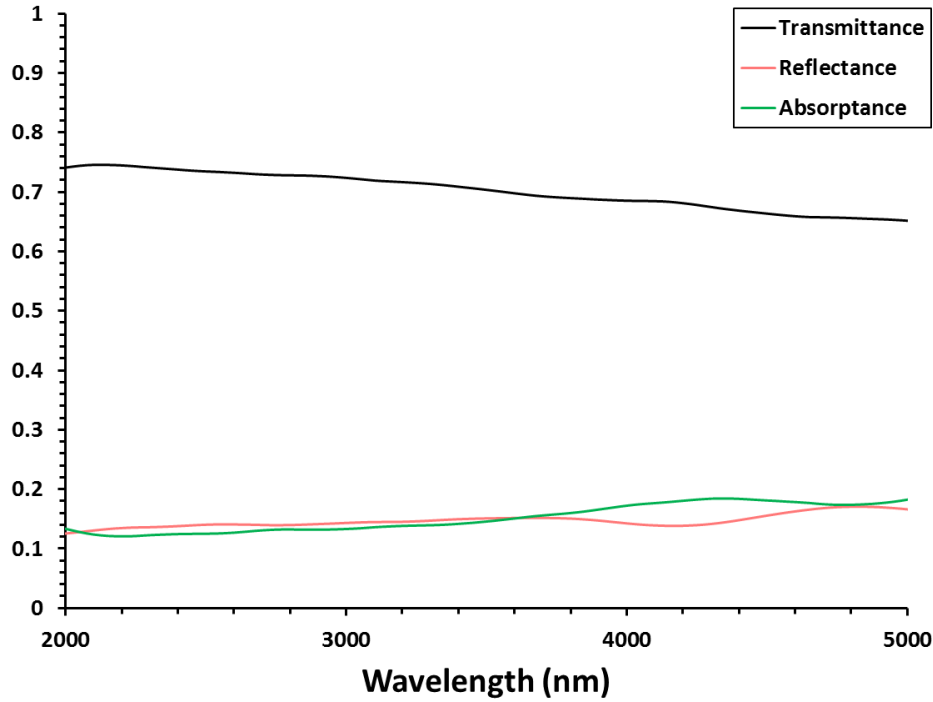
Figure 6.4. Simulated transmittance (black), reflectance (red), and absorptance (green) of 2 nm Ni thin film on nw-BCB layer based on bulk $\bar{n}(\lambda)$ values. The nw array geometrical parameters were D = 700 nm, P = 1500 nm, and L = 4000 nm.

Absorptance of the nw photodetector was also investigated for linear (X) and circular (left hand circular polarized, LHCP: $x + j \cdot y$ and right hand circular polarized, RHCP: $x - j \cdot y$) polarized incident light in addition to Y-polarized incident light. As shown in figure 6.5, the absorptance profiles overlapped indicating that the photodetector is polarization invariant. This invariance is expected due to the symmetry of the square nw array and circular nw cross-section. Additionally, the lack of exact equality between the absorptance profiles of different polarizations are due to computational anomaly.
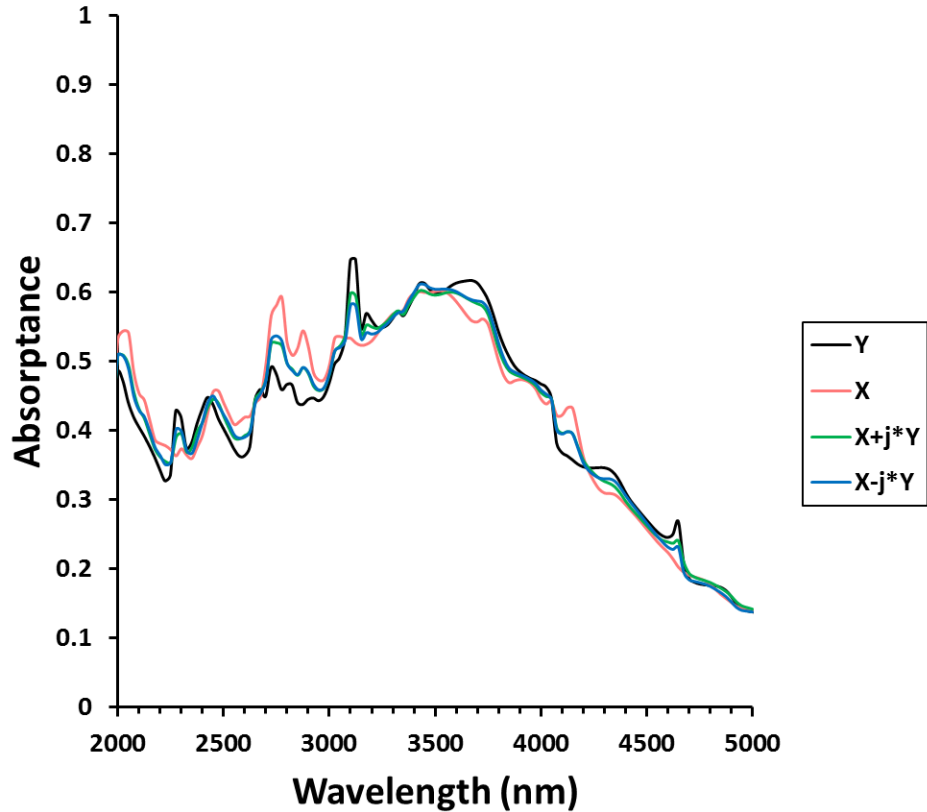
Figure 6.5. HE_{11} resonance absorptance spectra of InSb nw photodetector active region for linear (Y (black) and X (red)) and circular (X + j*Y (green) and X – j*Y (blue)) polarized incident light. The nw array geometrical parameters are D = 700 nm, P = 1500 nm, and L = 4000 nm.

The linear and circular polarized incident light also couples to the HE_{11} radial mode. The coupling of linearly polarized incident light with HE_{1n} radial modes is a known phenomenon which results from their E-fields being antisymmetric under mirror reflection (see section 2.7.3) [20,25,36,43,80]. Similarly, circularly polarized incident light couples with the HE_{1n} radial modes because they are composed of E_x and E_y fields, separated by $\pm\pi/2$ phase difference, which are likewise antisymmetric under mirror reflection.

Having said, the nw photodetector can be made polarization-sensitive by breaking the nw cross-section or array symmetry. For example, the former can be achieved by deforming the circular cross-section into an ellipse. This would split the HE_{1n} radial mode resonances along X- and Y-polarization direction with the absorptance spectra along the major axis more red-shifted compared to that along the minor axis. This may have potential polarization-sensitive applications in the IR [50]. The optimization of elliptical cross-section nws for polarization-sensitive detectors could be a useful future study.

6.2. Flow of light in nw photodetector

Power flow (time average Poynting vector) of incident light flowing into the nws in the photodetector configuration was investigated at the HE_{11} resonance wavelength (3550 nm) for D = 700 nm, P = 1500 nm, and L = 10000 nm on PML substrate. Large L was chosen to determine the power flow over a longer distance along the nw axis. The goal was to investigate how light enters the nw device at the resonance wavelength.

(a)   **(b)**
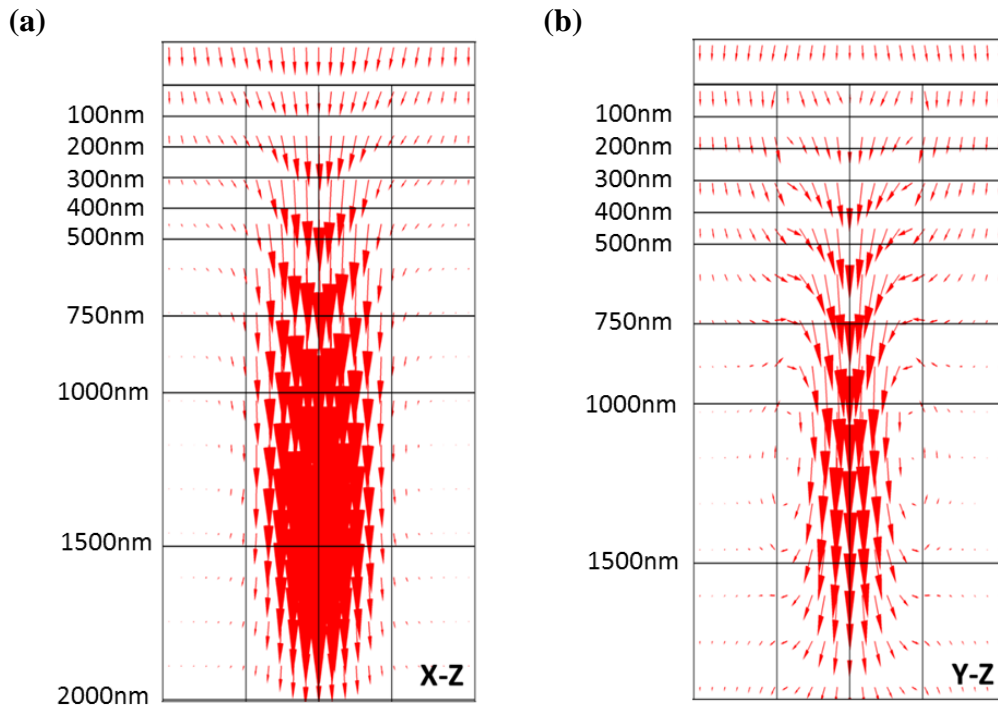
Figure 6.6. Time average Poynting vector field on HE_{11} resonance wavelength (3550 nm) of the InSb nw device along the (a) x-z and (b) y-z plane. The scale represents L from the nw tip.

Figure 6.6 shows the time average Poynting vector field at the HE_{11} resonance wavelength along x-z and y-z planes for Y-polarized incident light. In both cases light flows into the nw through the nw-Ni top surface interface and nw sidewalls. The noted exception being that the power flow profile at certain locations along the nw sidewalls in the y-z plane curls back into the nw (e.g. L = ~1000-1500 nm figure 6.6 (b)) similar to vortices. These vortices occur due to the electric (E) and H-field profiles of the HE_{11} radial mode.

As shown in figure 6.7 (a), at 100 nm below the Ni-nw interface, the flux entering the top nw surface is negligible at the nw cross-section edge and increases

towards the nw cross-section centre, indicating that the incident light is funnelled into the nw core.

(a)

(b)   **(c)**
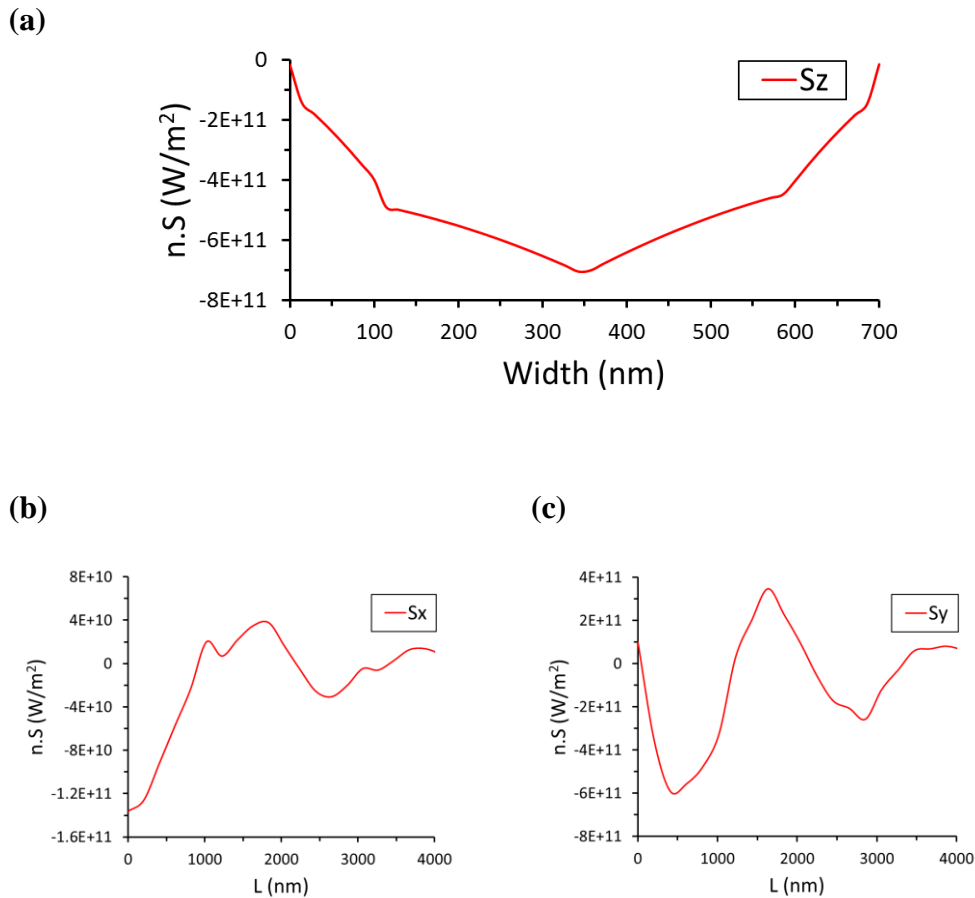
Figure 6.7. Magnitude of light flux entering the nw surface (n·S): (a) at the nw top, along the y-z plane (100 nm beneath the Ni contact) and sidewalls along the (b) x-z plane and (c) y-z plane. Negative values indicate flux entering the nw.

The power flow entering the nw sidewalls in the direction of polarization, y-z, is similar to that in the x-z plane. The flux flows in and out of the nw sidewalls (figure 6.7 (b) and (c)) concentrating at specific locations in the core along the nw axis (figure 6.6 (a) and (b)). The maximum flux entering the nw along the x-z plane

is at the nw-Ni interface (figure 6.7 (b)). While along the y-z plane (figure 6.7 (c)), incident light entering the nw sidewalls reaches a maximum at around L of ~ 500 nm. It can be noticed that the amount of flux entering the nw side walls is greater along the y-z plane, which is oriented in the polarization direction, compared to the x-z plane. As the light attenuates axially along L, the amplitude of light flux entering and exiting the nw decreases.

7 Conclusion

Semiconductor nanowires (nws) behave as nanoscopic waveguides due to the large refractive index difference between the nanowire (nw) material and its surroundings. 2D photonic crystal-like behavior is further observed when these nanoscopic waveguides are arranged into an array. The resultant geometrical arrangement gives rise to unique optical phenomena that govern the overall nw array absorptance. These optical phenomena have been identified as radial mode resonance, near-field evanescent wave coupling, and Fabry-Perot (F-P) mode resonance. Their individual contributions to the nw array absorptance only depend on the nw geometrical parameters: diameter (D), array period (P), and length (L). These properties were investigated for GaAs, InP, InAs, and InSb nws with the eventual aim of developing nw-based multispectral infrared (IR) detectors. Summarized simulation results are presented in this final thesis chapter followed by prospective future simulation work.

7.1 Summary of key observations

Sharp resonance absorptance peaks were observed for each D and P in vertical nws. These peaks are due to the incident light strongly coupling to the HE_{1n} family of radial modes and attenuating along the nw axis. These HE_{1n} resonance peaks also strongly red-shifted with increasing D for a fixed P and weakly red-

shifted with increasing P for fixed D. The latter phenomenon is due to near-field coupling and was confirmed in detail from InSb nw simulations. As the L increased, the HE_{1n} resonance absorptance increased, with the absorptance eventually saturating after which the peak spectrally broadened.

Near-field coupling between neighbouring nws increased with increasing diameter-to-period ratio (D/P). Increasing D/P (decreasing P for fixed D) causes a blue-shift of the HE_{1n} resonance absorptance peaks and an increase in their full-width-at-half-maximum (FWHM). Conversely, decreasing D/P (increasing P for fixed D) decreases the near-field coupling between neighbouring nws, which in turn red-shifts the HE_{1n} resonance absorptance peak. The rate of this red-shift decreases with decreasing D/P ratio until it becomes negligible. At this juncture the nws can be thought of as single nanoscopic waveguides. For a fixed L, the resonance absorptance peak also decreases for large D/P (> 0.5) and small D/P (< 0.2). In the former case, the nw resonance absorptance peak reaches thin film values as D/P approaches 1.

The influence of F-P resonance on nw array absorptance is negligible at the HE_{1n} resonance wavelengths for strongly coupled light at large L. Light at large L is attenuated along the nw axis. For weakly coupled light or shorter L, at HE_{1n} resonance wavelength, the F-P resonance can increase nw absorptance.

From the simulation study on GaAs, InP, InAs, and InSb nws, it was observed that the nw absorptance on HE_{11} resonance can exceed equivalent thickness thin film absorptance. This has the potential for more efficient

photodetection than existing thin film technology. Furthermore, the HE_{1n} resonance absorption peak and bandwidth can be continuously tuned across the visible (VIS) and IR wavelengths by adjusting the nw array geometrical parameters: D, P, and L. All of these properties can be achieved by using a single material system, which in principle opens the avenue for nw based multi-spectral photodetectors with improved wavelength selection compared to existing photodetectors.

With the goal of producing multispectral nw IR photodetectors, InSb based nws were further investigated. The InSb bandgap edge (~7300 nm at 300 K) extends well into the mid-wavelength infrared (MWIR: 3-8 μm) spectrum. The nw array D, P, and L were optimized to achieve HE_{11} resonance absorptance of ~0.8 with minimum aspect ratio (L/D) for nws in air and with Bisbenzocyclobutene (BCB) filler between nws. For nws in air, the HE_{11} resonance peak FWHM was less than 1000 nm for D ≤ 900 nm.

Thereafter, a practical photodetector device was simulated for optimized P and L for D = 700 nm in BCB. The device design was comprised of InSb nws on Si substrate with BCB filler, and a top Ni ultrathin contact layer. Despite a decrease in the nw array absorptance peak from ~0.8 without Ni contact to ~0.6 with Ni contact, the HE_{11} resonance showed superior optical absorptance compared to an InSb thin film of comparable thickness with identical Ni contact. The results are promising as they theoretically prove the viability of nw-based multispectral photodetectors. The nw photodetector absorptance was also shown to be invariant

under normal incident polarized and unpolarized light. This was due to the circular symmetry of the nw cross-section and square symmetry of the nw array.

7.2 Prospective future simulation work

Some future work based on the current simulation study can be undertaken concurrent with the experimental efforts to realize nw based IR multispectral detectors. They are briefly outlined in this section.

An immediate future work is to integrate the optical model developed in this thesis with an electrical model. This will enable investigators to better determine the suitable placement of junctions, doping levels, and output photocurrent for the optimized InSb nw array geometrical parameters in device configuration. The optimum junction can also be compared with the light flux entering the nw sidewalls to provide a general relationship between them. The simulated data can also be correlated with experimental device optoelectronic characterization results.

Further simulations can be performed on $InAs_{0.4}Sb_{0.6}$ based nws as $InAs_{0.4}Sb_{0.6}$ has a bandgap of 14.7 μm at 300 K and 9.0 μm at 77 K. 77 K is approximately the working temperature for high performance photon detectors. The bandgap at 77 K allows for the possibility of realizing nw-based long wavelength infrared (LWIR) nw multispectral detector.

Simulations can also be done on single or multiple axially stacked quantum dots (QDs) in a nw array. Given that the HE_{11} resonance wavelength red-shifts with

increasing D, its red-shift can be tracked with the transmittance peak or reflectance dip in the bandgap region of the nw. The resonance peak can then be aligned with the quantum dot inter- or intra-band transition energy gap to boost quantum dot absorptance. This can open up novel quantum dot (QD) integrated nw photodetector applications in LWIR.

Lastly, array geometrical parameter optimization study can be pursued for elliptical cross-section nws in the IR spectrum. This can be achieved using smaller bandgap materials, such as InAs, InSb, etc. The results can be used in polarization-sensitive applications, for example in quantum computing and communication.

8 Bibliography

[1]   R. Paschotta, RP Photonics Encyclopedia, RP Photonics. (2012). https://www.rp-photonics.com/infrared_light.html (accessed June 30, 2016).

[2]   A. Rogalski, Infrared detectors: An overview, Infrared Phys. Technol. 43 (2002) 187–210. doi:10.1016/S1350-4495(02)00140-8.

[3]   S.O. Kasap, Optoelectronics and Photonics: Principles and Practices, 1st ed., Prentice-Hall, Inc., Upper Saddle River, 2001.

[4]   A. Rogalski, HgCdTe infrared detector material: history, status and outlook, Reports Prog. Phys. 68 (2005) 2267–2336. doi:10.1088/0034-4885/68/10/R01.

[5]   A. Rogalski, J. Antoszewski, L. Faraone, Third-generation infrared photodetector arrays, J. Appl. Phys. 105 (2009). doi:10.1063/1.3099572.

[6]   A. Rogalski, P. Martyniuk, M. Kopytko, Challenges of small-pixel infrared detectors: a review, Reports Prog. Phys. 79 (2016) 046501. doi:10.1088/0034-4885/79/4/046501.

[7]   P. Martyniuk, J. Antoszewski, M. Martyniuk, L. Faraone, A. Rogalski, New concepts in infrared photodetector designs, Appl. Phys. Rev. 1 (2014) 041102. doi:10.1063/1.4896193.

[8]   T. Sprafke, J.W. Beletic, High-Performance Infrared Focal Plane Arrays for Space Applications, Opt. Photonics News. 19 (2008).

[9]   A. Rogalski, Infrared Detectors for the Future, Acta Phys. Pol. A. 116 (2009).

[10]   S.C. Liew, Optical Remote Sensing, Cent. Remote Imaging, Sens. Process. Natl. Univ. Singapore. (2001). http://www.crisp.nus.edu.sg/~research/tutorial/optical.htm (accessed July 3, 2016).

[11]   Y. Zhang, J. Wu, M. Aagesen, H. Liu, III–V nanowires and nanowire optoelectronic devices, J. Phys. D. Appl. Phys. 48 (2015) 463001. doi:10.1088/0022-3727/48/46/463001.

[12]   K.L. Kavanagh, Misfit dislocations in nanowire heterostructures, Semicond. Sci. Technol. 25 (2010) 24006. doi:10.1088/0268-1242/25/2/024006.

[13]   R.R. Lapierre, A.C.E. Chia, S.J. Gibson, C.M. Haapamaki, J. Boulanger, R. Yee, P. Kuyanov, J. Zhang, N. Tajik, N. Jewell, K.M.A. Rahman, III-V nanowire photovoltaics: Review of design for high efficiency, Phys. Status Solidi - Rapid Res. Lett. 7 (2013) 815–830. doi:10.1002/pssr.201307109.

[14]   V.J. Logeeswaran, J. Oh, A.P. Nayak, A.M. Katzenmeyer, K.H. Gilchrist, S. Grego, N.P. Kobayashi, S.-Y. Wang, A.A. Talin, N.K. Dhar, M.S. Islam, A Perspective on Nanowire Photodetectors: Current Status, Future Challenges, and Opportunities, IEEE J. Sel. Top. Quantum Electron. 17 (2011) 1002–1032. doi:10.1109/JSTQE.2010.2093508.

[15]   P.K. Mohseni, A.D. Rodrigues, J.C. Galzerani, Y.A. Pusep, R.R. LaPierre, Structural and optical analysis of GaAsP/GaP core-shell nanowires, J. Appl. Phys. 106 (2009). doi:10.1063/1.3269724.

[16]   P. Kuyanov, R.R. LaPierre, Photoluminescence and photocurrent from InP nanowires with InAsP quantum dots grown on Si by molecular beam epitaxy, Nanotechnology. 26 (2015) 315202. doi:10.1088/0957-4484/26/31/315202.

[17]   K.H. Li, X. Liu, Q. Wang, S. Zhao, Z. Mi, Ultralow-threshold electrically injected AlGaN nanowire ultraviolet lasers on Si operating at low temperature, Nat. Nanotechnol. 10 (2015) 140–4. doi:10.1038/nnano.2014.308.

[18]   K.M. Azizur-Rahman, R.R. LaPierre, Wavelength-selective absorptance in GaAs, InP and InAs nanowire arrays, Nanotechnology. 26 (2015) 295202. doi:10.1088/0957-4484/26/29/295202.

[19]   K.M. Azizur-Rahman, R.R. LaPierre, Optical design of a mid-wavelength infrared InSb nanowire photodetector, Nanotechnology. 27 (2016) 1–8. doi:10.1088/0957-4484/27/31/315202.

[20]   K.T. Fountaine, W.S. Whitney, H.A. Atwater, Resonant absorption in semiconductor nanowires and nanowire arrays: Relating leaky waveguide modes to Bloch photonic crystal modes, J. Appl. Phys. 116 (2014). doi:10.1063/1.4898758.

[21]   A.W. Snyder, J.D. Love, Optical Waveguide Theory, Chapman and Hall Ltd, New York, 1983.

[22]   J. Bures, Guided Optics - Optical Fibers and All-fiber Components, Wiley-VCH Verlag GmbH & Co., Strauss GmbH, Morlenbach, 2009.

[23]   Z. Fan, R. Kapadia, P.W. Leu, X. Zhang, Y.L. Chueh, K. Takei, K. Yu, A. Jamshidi, A.A. Rathore, D.J. Ruebusch, M. Wu, A. Javey, Ordered arrays of dual-diameter nanopillars for maximized optical absorption, Nano Lett. 10 (2010) 3823–3827. doi:10.1021/nl1010788.

[24] T. Okoshi, Optical Fibers, Academic Press, INC., New York, 1982.

[25] J.D. Joannopoulos, S.G. Johnson, J.N. Winn, R.D. Meade, Photonic Crystals - Molding the Flow of Light, 2nd ed., Princeton University Press, Princeton, 2008. doi:10.1063/1.1586781.

[26] A.B. Movchan, N.V. Movchan, C.G. Poulton, Asymptotic Models of Fields in Dilute and Densely Packed Composites, World Scientific Publishing Co. Pte. Ltd., Singapore, 2002.

[27] L. Cao, P. Fan, A.P. Vasudev, J.S. White, Z. Yu, W. Cai, J.A. Schuller, S. Fan, M.L. Brongersma, Semiconductor nanowire optical antenna solar absorbers, Nano Lett. 10 (2010) 439–445. doi:10.1021/nl9036627.

[28] A. Solanki, P. Gentile, V. Calvo, G. Rosaz, B. Salem, V. Aimez, D. Drouin, N. Pauc, Geometrical control of photocurrent in active Si nanowire devices, Nano Energy. 1 (2012) 714–722. doi:10.1016/j.nanoen.2012.05.010.

[29] S.-K. Kim, R.W. Day, J.F. Cahoon, T.J. Kempa, K.-D. Song, H.-G. Park, C.M. Lieber, Tuning Light Absorption in Core/Shell Silicon Nanowire Photovoltaic Devices through Morphological Design, Nano Lett. 12 (2012) 4971−4976.

[30] L. Cao, J.S. White, J.-S. Park, J.A. Schuller, B.M. Clemens, M.L. Brongersma, Engineering light absorption in semiconductor nanowire devices, Nat. Mater. 8 (2009) 643–647. doi:10.1038/nmat2477.

[31] K. Seo, M. Wober, P. Steinvurzel, E. Schonbrun, Y. Dan, T. Ellenbogen, K.B. Crozier, Multicolored vertical silicon nanowires, Nano Lett. 11 (2011) 1851–1856. doi:10.1021/nl200201b.

[32] H. Park, K. Seo, K.B. Crozier, Adding colors to polydimethylsiloxane by embedding vertical silicon nanowires, Appl. Phys. Lett. 101 (2012). doi:10.1063/1.4766944.

[33] N. Dhindsa, J. Walia, M. Pathirane, I. Khodadad, W.S. Wong, S.S. Saini, Adjustable optical response of amorphous silicon nanowires integrated with thin films, Nanotechnology. 27 (2016) 145703. doi:10.1088/0957-4484/27/14/145703.

[34] A. Solanki, K. Crozier, Vertical germanium nanowires as spectrally-selective absorbers across the visible-to-infrared, Appl. Phys. Lett. 105 (2014) 2012–2017. doi:10.1063/1.4901438.

[35] N. Anttu, H.Q. Xu, Coupling of light into nanowire arrays and subsequent absorption, J. Nanosci. Nanotechnol. 10 (2010) 7183–7187. doi:10.1166/jnn.2010.2907.

[36] N. Anttu, H.Q. Xu, Efficient light management in vertical nanowire arrays for photovoltaics, Opt. Express. 21 (2013) A558. doi:10.1364/OE.21.00A558.

[37] N. Anttu, A. Abrand, D. Asoli, M. Heurlin, I. Åberg, L. Samuelson, M. Borgström, Absorption of light in InP nanowire arrays, Nano Res. 7 (2014) 816–823. doi:10.1007/s12274-014-0442-y.

[38] P. Kailuweit, M. Peters, J. Leene, K. Mergenthaler, F. Dimroth, A.W. Bett, Numerical simulations of absorption properties of InP nanowires for solar cell applications, Prog. Photovolt Res. Appl. 20 (2012) 945–953.

[39] J. Kupec, R.L. Stoop, B. Witzigmann, Light absorption and emission in nanowire array solar cells, Opt. Express. 18 (2010) 27589–27605. doi:10.1364/OE.18.027589.

[40] H. Guo, L. Wen, X. Li, Z. Zhao, Y. Wang, Analysis of optical absorption in GaAs nanowire arrays, Nanoscale Res. Lett. 6 (2011) 617. doi:10.1186/1556-276X-6-617.

[41] N. Dhindsa, A. Chia, J. Boulanger, I. Khodadad, R. LaPierre, S.S. Saini, Highly ordered vertical GaAs nanowire arrays with dry etching and their optical properties, Nanotechnology. 25 (2014) 305303(11pp). doi:10.1088/0957-4484/25/30/305303.

[42] P.M. Wu, N. Anttu, H.Q. Xu, L. Samuelson, M.E. Pistol, Colorful InAs nanowire arrays: From strong to weak absorption with geometrical tuning, Nano Lett. 12 (2012) 1990–1995. doi:10.1021/nl204552v.

[43] B. Wang, P.W. Leu, Tunable and selective resonant absorption in vertical nanowires, Opt. Lett. 37 (2012) 3756–3758. doi:10.1364/OL.37.003756.

[44] K.B. Dossou, L.C. Botten, A.A. Asatryan, B.C.P. Sturmberg, M.A. Byrne, C.G. Poulton, R.C. McPhedran, C.M. de Sterke, Modal formulation for diffraction by absorbing photonic crystal slabs, J. Opt. Soc. Am. A. 29 (2012) 817. doi:10.1364/JOSAA.29.000817.

[45] A.-L. Henneghien, B. Gayral, Y. Désières, J.-M. Gérard, Simulation of waveguiding and emitting properties of semiconductor nanowires with hexagonal or circular sections, J. Opt. Soc. Am. B. 26 (2009) 2396. doi:10.1364/JOSAB.26.002396.

[46] N. Dhindsa, S.S. Saini, Comparison of ordered and disordered silicon nanowire arrays: experimental evidence of photonic crystal modes, Opt. Lett. 41 (2016) 2045.

[47] M. Khorasaninejad, S. Patchett, J. Sun, N. O, S.S. Saini, Diameter dependence of polarization resolved reflectance from vertical silicon nanowire arrays: Evidence of tunable absorption, J. Appl. Phys. 114

(2013). doi:10.1063/1.4813081.

[48] B.C.P. Sturmberg, K.B. Dossou, L.C. Botten, A.A. Asatryan, C.G. Poulton, C.M. de Sterke, R.C. McPhedran, Modal analysis of enhanced absorption in silicon nanowire arrays, Opt. Express. 19 (2011) A1067. doi:10.1364/OE.19.0A1067.

[49] J. Li, H. Yu, Y. Li, Solar energy harnessing in hexagonally arranged Si nanowire arrays and effects of array symmetry on optical characteristics, Nanotechnology. 23 (2012) 194010. doi:10.1088/0957-4484/23/19/194010.

[50] H. Park, K.B. Crozier, Elliptical silicon nanowire photodetectors for polarization-resolved imaging, Opt. Express. 23 (2015) 7209. doi:10.1364/OE.23.007209.

[51] H. Alaeian, A.C. Atre, J.A. Dionne, Optimized light absorption in Si wire array solar cells, J. Opt. 14 (2012) 024006. doi:10.1088/2040-8978/14/2/024006.

[52] Y. Hu, R.R. Lapierre, M. Li, K. Chen, J.J. He, Optical characteristics of GaAs nanowire solar cells, J. Appl. Phys. 112 (2012). doi:10.1063/1.4764927.

[53] B.C.P. Sturmberg, K.B. Dossou, L.C. Botten, A.A. Asatryan, C.G. Poulton, R.C. McPhedran, C.M. De Sterke, Optimizing Photovoltaic Charge Generation of Nanowire Arrays: A Simple Semi-Analytic Approach, ACS Photonics. 1 (2014) 683–689. doi:10.1021/ph500212y.

[54] K.T. Fountaine, C.G. Kendall, H.A. Atwater, Near-unity broadband absorption designs for semiconducting nanowire arrays via localized radial mode excitation, Opt. Express. 22 (2014) A930. doi:10.1364/OE.22.00A930.

[55] H. Park, K.B. Crozier, Multispectral imaging with vertical silicon nanowires, Sci. Rep. 3 (2013) 2460. doi:10.1038/srep02460.

[56] H. Park, Y. Dan, K. Seo, Y.J. Yu, P.K. Duane, M. Wober, K.B. Crozier, Filter-free image sensor pixels comprising silicon nanowires with selective color absorption, Nano Lett. 14 (2014) 1804–1809. doi:10.1021/nl404379w.

[57] J. Svensson, N. Anttu, N. Vainorius, B.M. Borg, L.E. Wernersson, Diameter-dependent photocurrent in InAsSb nanowire infrared photodetectors, Nano Lett. 13 (2013) 1380–1385. doi:10.1021/nl303751d.

[58] M.D. Thompson, A. Alhodaib, A.P. Craig, A. Robson, A. Aziz, A. Krier, J. Svensson, L.-E. Wernersson, A.M. Sanchez, A.R.J. Marshall, Low Leakage-Current InAsSb Nanowire Photodetectors on Silicon, Nano Lett. ASAP (2015) acs.nanolett.5b03449. doi:10.1021/acs.nanolett.5b03449.

[59]   K. Zhang, D. Li, Electromagnetic Theory for Microwaves and Optoelectronics, 2nd ed., Springer-Verlag, Berlin, 2008.

[60]   D.J. Griffiths, Introduction to Electrodynamics, 3rd ed., Prentice-Hall, Inc., Upper Saddle River, 1999.

[61]   H. Jackel, Optoelectronics and Optical Communication, (2009). http://people.ee.ethz.ch/~fyuriy/oe/ (accessed June 7, 2016).

[62]   G. Grzela, Directional Light Emission and Absorption by Semiconductor Nanowires, Technische Universiteit Eindhoven, 2013. doi:http://dx.doi.org/10.6100/IR757437.

[63]   L.C. Botten, R.C. McPhedran, C.M. de Sterke, N.A. Nicorovici, A.A. Asatryan, G.H. Smith, T.N. Langtry, T.P. White, D.P. Fussell, B.T. Kuhlmey, From Multipole Methods to Photonic Crystal Device Modeling, in: K. Yasumoto (Ed.), Electromagn. Theory Appl. Photonic Cryst., CRC Press, 2004: p. 464. https://books.google.ca/books?id=vm3LBQAAQBAJ&pg=PA47&dq=rayl eigh+identity+infinite+lattice&source=gbs_toc_r&cad=4#v=onepage&q=r ayleigh identity infinite lattice&f=false.

[64]   S.L. Chuang, Physics of Optoelectronic Devices, John Wiley & Sons, Inc., 1995.

[65]   I. Babuska, U. Banerjee, J.E. Osborn, Generalized Finite Element Methods — Main Ideas, Results and Perspective, Int. J. Comput. Methods. 01 (2004) 67–103. doi:10.1142/S0219876204000083.

[66]   J. Mason, Finite element solution for electromagnetic scattering from two-dimensional bodies, The University of Michigan, 1982. http://deepblue.lib.umich.edu/bitstream/handle/2027.42/20975/rl0734.0001 .001.pdf?sequence=2&isAllowed=y.

[67]   J. Jin, V.V. Liepa, J.L. Volkis, Finite Element-Boundary Element Methods for Electromagnetic Scattering, The University of Michigan, 1989. http://deepblue.lib.umich.edu/bitstream/handle/2027.42/21035/rl0868.0001 .001.pdf?sequence=2.

[68]   O.C. Zienkiewicz, R.L. Taylor, J.Z. Zhu, The Finite Element Method: Its Basis & Fundamentals, 6th ed., Butterworth-Heinemann, 2005.

[69]   COMSOL, The Finite Element Method, (2016). https://www.comsol.com/multiphysics/finite-element-method (accessed May 26, 2016).

[70]   E. Süli, Lecture Notes on Finite Element Methods for Partial Differential Equations, Oxford, UK, 2012.

[71] W. Frei, Meshing Your Geometry: When to Use the Various Element Types, COMSOL BLOG. (2013). https://www.comsol.com/blogs/meshing-your-geometry-various-element-types/ (accessed May 26, 2016).

[72] R.L. de Orio, Electromigration Modeling and Simulation, Vienna University of Technology, 2010. http://www.iue.tuwien.ac.at/phd/orio/diss_html.html (accessed May 26, 2016).

[73] COMSOL, COMSOL Multiphysics Reference Guide, 3.5a ed., COMSOL AB., 2008.

[74] COMSOL, RF Module User's Guide, 3.5a ed., COMSOL AB., 2008.

[75] S.G. Johnson, Notes on Perfectly Matched Layers (PMLs), (2010) 1–18. math.mit.edu/~stevenj/18.369/pml.pdf (accessed May 31, 2016).

[76] A.C.E. Chia, R.R. LaPierre, Contact planarization of ensemble nanowires, Nanotechnology. 22 (2011) 245304. doi:10.1088/0957-4484/22/24/245304.

[77] E.D. Palik, ed., Handbook of Optical Constants of Solids, Academic Press, INC., Washington, 1985.

[78] A.D. Rakic, A.B. Djurisic, J.M. Elazar, M.L. Majewski, Optical properties of metallic films for vertical-cavity optoelectronic devices, Appl. Opt. 37 (1998) 5271–5283. doi:10.1364/AO.37.005271.

[79] M.N. Polyanskiy, Refractive Index Database, (2016). http://refractiveindex.info/?shelf=main&book=Ni&page=Rakic (accessed May 26, 2016).

[80] N. Anttu, Nanophotonics in absorbing III-V nanowire arrays, Lund University, 2013.

[81] M.C. Plante, R.R. LaPierre, Au-assisted growth of GaAs nanowires by gas source molecular beam epitaxy: Tapering, sidewall faceting and crystal structure, J. Cryst. Growth. 310 (2008) 356–363. doi:10.1016/j.jcrysgro.2007.10.050.

[82] J. Walia, N. Dhindsa, J. Flannery, I. Khodadad, J. Forrest, R. Lapierre, S. Saini, Diameter Dependent Heating in GaAs Nanowires, 1 (2014) 893–895.

[83] N. Anttu, Geometrical optics, electrostatics, and nanophotonic resonances in absorbing nanowire arrays, Opt. Lett. 38 (2013) 730–2. doi:10.1364/OL.38.000730.

[84] M. Khorasaninejad, N. Abedzadeh, J. Walia, S. Patchett, S.S. Saini, Color matrix refractive index sensors using coupled vertical silicon nanowire arrays, Nano Lett. 12 (2012) 4228–4234. doi:10.1021/nl301840y.

[85] N. Anttu, K.L. Namazi, P.M. Wu, P. Yang, H. Xu, H.Q. Xu, U. Håkanson, Drastically increased absorption in vertical semiconductor nanowire arrays: A non-absorbing dielectric shell makes the difference, Nano Res. 5 (2012) 863–874. doi:10.1007/s12274-012-0270-x.

[86] T. Nobis, M. Grundmann, Low-order optical whispering-gallery modes in hexagonal nanocavities, Phys. Rev. A - At. Mol. Opt. Phys. 72 (2005) 1–11. doi:10.1103/PhysRevA.72.063806.

[87] J. Wallentin, N. Anttu, D. Asoli, M. Huffman, I. Aberg, M.H. Magnusson, G. Siefer, P. Fuss-Kailuweit, F. Dimroth, B. Witzigmann, H.Q. Xu, L. Samuelson, K. Deppert, M.T. Borgström, InP nanowire array solar cells achieving 13.8% efficiency by exceeding the ray optics limit, Science. 339 (2013) 1057–60. doi:10.1126/science.1230969.

[88] G. Grzela, R. Paniagua-Dominguez, T. Barten, D. Van Dam, J.A. Sanchez-Gil, J.G. Rivas, Nanowire antenna absorption probed with time-reversed fourier microscopy, Nano Lett. 14 (2014) 3227–3234. doi:10.1021/nl5005948.

[89] S. Hu, C.-Y. Chi, K.T. Fountaine, M. Yao, H.A. Atwater, P.D. Dapkus, N.S. Lewis, C. Zhou, Optical, electrical, and solar energy-conversion properties of gallium arsenide nanowire-array photoanodes, Energy Environ. Sci. 6 (2013) 1879–1890. doi:10.1039/C3EE40243F.

[90] L. Wen, Z. Zhao, X. Li, Y. Shen, H. Guo, Y. Wang, Theoretical analysis and modeling of light trapping in high efficiency GaAs nanowire array solar cells, Appl. Phys. Lett. 99 (2011) 2009–2012. doi:10.1063/1.3647847.

[91] Y. Yu, L. Cao, Coupled leaky mode theory for light absorption in 2D, 1D, and 0D semiconductor nanostructures, Opt. Express. 20 (2012) 13847–56. doi:10.1364/OE.20.013847.

[92] C. Lin, M.L. Povinelli, Optical absorption enhancement in silicon nanowire arrays with a large lattice constant for photovoltaic applications, Opt. Express. 17 (2009) 19371–81. doi:10.1364/OE.17.019371.

[93] S. Mokkapati, K.R. Catchpole, Nanophotonic light trapping in solar cells, J. Appl. Phys. 112 (2012). doi:10.1063/1.4747795.

[94] N. Huang, C. Lin, M.L. Povinelli, Broadband absorption of semiconductor nanowire arrays for photovoltaic applications, J. Opt. 14 (2012) 024004. doi:10.1088/2040-8978/14/2/024004.

[95] H. Goto, K. Nosaki, K. Tomioka, S. Hara, K. Hiruma, J. Motohisa, T. Fukui, Growth of core-shell InP nanowires for photovoltaic application by selective-area metal organic vapor phase epitaxy, Appl. Phys. Express. 2 (2009) 3–6. doi:10.1143/APEX.2.035004.

[96] Electro-Optical-Industries, Atmospheric Absorption, (n.d.).
http://www.electro-optical.com/eoi_page.asp?h=Atmospheric Absorption
(accessed April 29, 2016).

[97] InSb - Indium Antimonide, IOFFE. (n.d.).
http://www.ioffe.ru/SVA/NSM/Semicond/InSb/basic.html (accessed July
13, 2016).

[98] Si - Silicon, IOFFE. (n.d.).
http://www.ioffe.ru/SVA/NSM/Semicond/Si/basic.html (accessed July 13,
2016).

[99] G.E. Cirlin, V.G. Dubrovskii, I.P. Soshnikov, N.V. Sibirev, Y.B.
Samsonenko, A.D. Bouravleuv, J.C. Harmand, F. Glas, Critical diameters
and temperature domains for MBE growth of III-V nanowires on lattice
mismatched substrates, Phys. Status Solidi - Rapid Res. Lett. 3 (2009) 112–
114. doi:10.1002/pssr.200903057.

[100] M.T. Robson, R.R. Lapierre, InAs nanowire growth modes on Si (111) by
gas source molecular beam epitaxy, J. Cryst. Growth. 436 (2016) 1–11.
doi:10.1016/j.jcrysgro.2015.11.035.

[101] D.S. Ghosh, L. Martinez, S. Giurgola, P. Vergani, V. Pruneri, Widely
transparent electrodes based on ultrathin metals, Opt. Lett. 34 (2009) 325–
327. doi:10.1364/OL.34.000325.

[102] H.G. Tompkins, S. Tasic, J. Baker, D. Convey, Spectroscopic ellipsometry
measurements of thin metal films, Surf. Interface Anal. 29 (2000) 179–187.
doi:10.1002/(SICI)1096-9918(200003)29:3<179::AID-SIA701>3.0.CO;2-
O.

[103] E. Dumont, B. Dugnoille, Optical properties of nickel thin films deposited
by electroless plating, (1997) 149–153.

9 Appendix

9.1 Matlab code: TE_{0n} and TM_{0n} eigenvalue calculation

The Matlab code below is associated with figure 2.2:

```matlab
clear all; close all; clc;
%Refractive index
n2=1;
n1=3.5;
m=0;%Mode order

%Setup TR
TR=linspace(0,8,2000);

Bessel_ratio=(besselj(m+1,TR))./(besselj(m,TR));

%Normalized frequency
V=[12];

TE0n_mode(length(V),length(TR))=0;
TM0n_mode(length(V),length(TR))=0;

for i=1:length(V)
%Setup TaoR
TaoR(i,:)=sqrt(V(i)^2-TR.^2);
T_Tao_ratio(i,:)=TR./TaoR(i,:);
ModBessel_ratio(i,:)=(besselk(m+1,TaoR(i,:))./besselk(m,TaoR(i,:)));
TE0n_mode(i,:)=-1*ModBessel_ratio(i,:).*T_Tao_ratio(i,:);
TM0n_mode(i,:)=-1*((n2^2)/(n1^2)).*ModBessel_ratio(i,:).*T_Tao_ratio(i,:);
end

figure;
plot(TR,Bessel_ratio,'k','LineWidth',2);%Left hand side of the equation
hold all;
plot(TR,TM0n_mode,'b','LineWidth',2);%Right hand side of the equation (1)
plot(TR,TE0n_mode,'r','LineWidth',2);%Right hand side of the equation (2)
```

```matlab
legend('J1(RT)/J0(RT)','TM Mode','TE Mode','FontSize',14,'FontWeight','bold');
title('TE and TM modes (m=0)','FontSize',18,'FontWeight','bold');
xlabel('RT','FontSize',16,'FontWeight','bold');
plot(TR,zeros(length(TR),1),'k--','LineWidth',2);
axis([0 8 -5 5]);
set(gca,'FontSize',14);
```

9.2 Matlab code: HE_{1n} and EH_{1n} eigenvalue calculation

The Matlab code below is associated with figure 2.5.

```matlab
clear all; close all; clc;
%Refractive index
n2=1;
n1=3.5;
m=1;%Mode order

%TR setup
TR=linspace(0,8,8000);
Bessel_ratio=(1/2).*((besselj(m-1,TR)-besselj(m+1,TR))./(besselj(m,TR)));

%Normalized frequency
V=[12];

EH_mode(length(V),length(TR))=0;
HE_mode(length(V),length(TR))=0;

for i=1:length(V)
%TaoR setup
TaoR(i,:)=sqrt(V(i)^2-TR.^2);
T_Tao_ratio(i,:)=TR./TaoR(i,:);
ModBessel_ratio(i,:)=(-1/2).*((besselk(m-
1,TaoR(i,:))+besselk(m+1,TaoR(i,:)))./besselk(m,TaoR(i,:)));
P(i,:)=((n1^2+n2^2)/(2*n1^2)).*ModBessel_ratio(i,:).*T_Tao_ratio(i,:);

Q1(i,:)=(((n1^2-n2^2)/(2*n1^2)).*ModBessel_ratio(i,:).*T_Tao_ratio(i,:)).^2;
Q2(i,:)=((m./TR).^2).*(1+((n2/n1).*T_Tao_ratio(i,:)).^2).*(1+T_Tao_ratio(i,:).^2
);
Q(i,:)=Q1(i,:)+Q2(i,:);

%Non-magnetic material
EH_mode(i,:)=-P(i,:)+sqrt(Q(i,:));%equation (1); converts to TE0n when m = 0
HE_mode(i,:)=-P(i,:)-sqrt(Q(i,:));%equation (2); converts to TM0n when m = 0
end

figure;
```

```matlab
%Multiplying the values by -1 b/c they are negative, this will make them
%positive on both sides of the equation
plot(TR,(-1)*Bessel_ratio,'k','LineWidth',2);%Left hand side of the equation
hold all;
plot(TR,(-1)*EH_mode,'b','LineWidth',2);%Right hand side of the equation (1)
plot(TR,(-1)*HE_mode,'r','LineWidth',2);%Right hand side of the equation (2)
legend('dJm(RT)/Jm(RT)','EH Mode','HE
Mode','FontSize',14,'FontWeight','bold');
title('HE and EH modes (m=1)','FontSize',18,'FontWeight','bold');
xlabel('RT','FontSize',16,'FontWeight','bold');
plot(TR,zeros(length(TR),1),'k--','LineWidth',2);
axis([0 8 -5 5]);
set(gca,'FontSize',14);
```